UNIVERSITY OF READING

Department of Meteorology

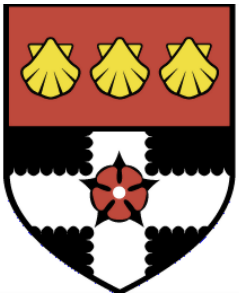

On the Parameterisation of Convection in the 'Grey-Zone'

Chuen Chung Chui

A thesis submitted for the degree of Doctor of Philosophy

January 2021

Declaration

I confirm that this is my own work and the use of all material from other sources has been properly and fully acknowledged.

Chuen Chung Chui

Abstract

Representing convection at kilometre-scale resolution (also known as the 'grey-zone') has been a challenge for numerical modellers. Conventional parameterisation approaches rely on assumptions only valid for very coarse resolution simulation and so cannot be applied at this resolution. However, the 'grey zone' is not sufficiently fine to fully resolve convective updraughts. A new approach towards solving the problem is proposed. The new Stochastic Explicitly Prognostic Mass Flux (SEP-MF) scheme features a stochastic triggering function based on the occurrence and strength of boundary layer thermals, as well as a fully prognostic (growth) plume model in which prognostic equations representing the evolution of sub-grid convection are solved explicitly. The SEP-MF scheme was tested in a case featuring a diurnal cycle of convection, a phenomenon which is known to be difficult to simulate. Results from this study suggest that the SEP-MF scheme is capable of producing scale-independent solutions of the diurnal cycle of convection, as well as improving the overall performance of kilometre-scale models in representing convection.

Acknowledgements

I would like to hereby sincerely show my gratitude towards everyone that was involved in this project. First of all, I would deeply thank my supervisors, Professor Peter A. Clark and Professor Robert S. Plant for their value guidance over the past four years. I would also like to thank Adrian Hill and Ben Shipway at the Met Office, who assisted me in getting the model running as well as provided me guidance on how to compile the model on other machines. Most importantly, I would like to thank my parents who have been wholeheartedly supporting me through the project. Of course, I must thank my girlfriend Yvonne, who had to tolerate my severe delays in the completion of this thesis.

Contents

Chapter 1

Introduction

1.1 Why study atmospheric convection?

Convection is a heat transfer mechanism exclusive to fluids due to internal motions induced by density perturbations. As hot air rises and cold air sinks, energy becomes more evenly distributed within the fluid over time. However, convection in the atmosphere is complicated by phase changes of water vapour in the air, in which latent heat transfer may alter the density difference between air parcels and the surrounding environment. This may lead to the formation of rapidly rising air columns known as convective updraughts. This type of atmospheric convection is referred to as moist convection and is the primary focus of this project.

Atmospheric convection is capable of triggering severe weather events such as heavy precipitation, lightning, large hail, strong gusts and tornadoes, and can cause loss of lives and properties. On 16 August 2004, sustained convective storms brought over 200 mm of rain to Boscastle, Cornwall, England within 24 hours. Heavy rain caused the river level to rise by 2 m in one hour and led to flash floods. The event ultimately brought extensive damages to local villages, with approximately 100 homes and businesses destroyed and 80 vehicles, with several buildings washed into the sea (Fenn et al., 2005; Golding et al., 2005; metoffice.gov.uk, 2015). In the United States, an average of 1000 tornadoes, a type of weather phenomenon associated with severe thunderstorms, are observed every year (Schaefer and Edwards, 1999), with 1,150 reported tornado-related deaths annually (Fricker, 2019). Over the tropical oceans where heat and moisture supplies are abundant, convective

thunderstorms may persist and aggregate into tropical cyclones. These rotating storms may release 100 PetaWatts of power, equivalent to 70 times the worldwide energy consumption (Emanuel, 1999) and are capable of bringing extreme winds and storm surges to coastal areas. Super Typhoon Haiyan in November 2013 was among the strongest tropical cyclones ever observed. It remains the strongest tropical cyclone to make landfall over the Philippines today, claiming 6000 lives and an economic loss of USD 5.8 million with its extreme winds and storm surge (Mori et al., 2014; Lagmay et al., 2015; bbc.com, 2019). Accurate forecast of convection could lead to better decisions being made to mitigate severe weather threats and reduce casualties and economic loss.

In addition to local weather, convection drives intra-seasonal variations and affects the global climate. In the tropics, the rainfall pattern is governed by the Madden-Julian Oscillation (MJO), an intra-seasonal variability in the form of an eastward propagating circulation (Madden and Julian, 1972). The associated circulation alternatively enhances and suppresses convective activities across the tropical oceans, affecting the intermittency of the Asian Summer Monsoon (Tong et al., 2009; Pai et al., 2011, e.g.), tropical cyclogenensis (Liebmann et al., 1994; Sobel and Maloney, 2000; Maloney and Hartmann, 2001) and rainfall over higher latitude regions (e.g. the Pineapple Express, Weller et al., 2012). Surface wind anomalies over the tropical Pacific ocean associated with MJO and other convective events (such as westerly wind bursts (WWB) associated with twin tropical cyclones scenarios, Seiki and Takayabu, 2007) can lead to an onset of the El-Niño Southern Oscillation (ENSO) event. Both the warm phase (El Niño) and cool phase (La Niña) are capable of affecting the weather patterns of the tropics and subtropics, including the rainfall, strength of the Asian Summer Monsoon (Qian et al., 2010) and tropical cyclone tracks (Camargo and Sobel, 2005). The impact of ENSO may extend beyond its source region to the entire globe via teleconnections (Yeh et al., 2018). Thus, predicting convection accurately is essential towards a reliable forecast of short-term climate and long-term climate change.

Numerical models are common tools for modern weather and climate predictions. They numerically solve the Navier-Stokes equations, the governing set of fluid dynamic equations, to simulate the evolution of the atmosphere. Yet, the spatial precision of models, commonly known as their resolution, is often insufficient to resolve (i.e. directly simulate) convection. Given its significant impact on the large-scale flow, models often represent the effect of convection through parameterisation; the vertical structure and strength of convection must be estimated based on features of the resolved-scale flow. The effect of the parameterised convection on the resolved-scale flow is then estimated, based on additional assumptions about the interactions between convection

and the resolved scale features. As I will discuss in detail in this chapter, conventional assumptions only hold true for low-resolution simulations. This limits the applicability of traditional convective parameterisation schemes, especially in high-resolution modelling.

The goal of this project is to develop a convection scheme for high-resolution simulations. We shall begin with understanding the nature and characteristics of convection, followed by the conventional ideas behind convective parameterisation and their limitations. Sections 1.2 and 1.3 describe the nature of atmospheric convection. Section 1.4 explains daytime convective development. Section 1.5 introduces convective parameterisation and identifies the challenges in representing convection in high-resolution simulations. Section 1.6 explains the motivation and defines the scope of this study.

1.2 The nature of moist convection

1.2.1 The physics of buoyancy

To understand how buoyancy drives convection, one may first recall the vertical momentum equation:

$$\frac{Dw}{Dt} = -\frac{1}{\rho}\frac{\partial p}{\partial z} - g \tag{1.2.1}$$

where w is the vertical velocity, p is the air pressure, ρ is the air density and g is the acceleration due to gravity. One may split each variable into its background state and a corresponding perturbation, *i.e.*

$$\rho = \bar{\rho} + \rho' \tag{1.2.2}$$

$$p = \bar{p} + p' \tag{1.2.3}$$

$$w = \underbrace{\bar{w}}_{=0} + w' = w' \tag{1.2.4}$$

where an overbar and a prime denote the background state and perturbation respectively. It follows that Equation (1.2.1) may be written as

$$(\bar{\rho} + \rho')\frac{Dw}{Dt} = \underbrace{-\frac{\partial \bar{p}}{\partial z} - \bar{\rho} g}_{=0,\ \text{hydrostatic balance}} - \frac{\partial p'}{\partial z} - \rho' g \tag{1.2.5}$$

Thus, Equation (1.2.5) becomes

$$\frac{Dw}{Dt} = -\frac{1}{\rho}\frac{\partial p'}{\partial z} - \frac{\rho'}{\rho}g \tag{1.2.6}$$

where the second term on the R.H.S. is generally known as *buoyancy*.

Consider the hydrostatic pressure distribution underneath an air parcel with a negative density perturbation. The local pressure directly below the perturbed parcel is smaller than that of the surrounding environment. Air responds to the resultant horizontal pressure gradient and converges towards the perturbed parcel from underneath. As a result, the air parcel is displaced upwards and rises. The opposite holds true for an air parcel with a positive density perturbation.

It is often more convenient to consider perturbation of temperature and moisture in the atmosphere rather than density directly. Consider the ideal gas equation

$$p = \rho R_d T_v \tag{1.2.7}$$

where R_d is the specific gas constant of dry air and T_v is the virtual temperature of air defined as

$$T_v = T(1 + 0.61q) \tag{1.2.8}$$

where q is the specific humidity in kg kg^{-1} and T is the temperature of air in K.

Considering a linear perturbation to Equation (1.2.7) yields

$$\bar{p} + p' = (\bar{\rho} + \rho')R_d(\bar{T_v} + T_v{}') \tag{1.2.9}$$

expanding which gives

$$\bar{p} + p' = \bar{\rho}R_d\bar{T_v} + \bar{\rho}R_dT_v' + \rho'R_d\bar{T_v} + \rho'R_dT_v{}' \tag{1.2.10}$$

Choosing the background state so that the idea gas law holds true

$$\bar{p} = \bar{\rho}R_d\bar{T_v} \tag{1.2.11}$$

and ignoring quadratic terms in perturbation variables, one obtains

$$\rho' = \frac{p'}{R_dT_v} - \bar{\rho}\frac{T_v{}'}{T_v} \tag{1.2.12}$$

It follows that b the buoyancy acceleration can be expressed as

$$b = -g\frac{\rho'}{\rho} = \underbrace{-g\frac{p'}{p}}_{\sim 0} + g\ \underbrace{\frac{\bar{\rho}}{\rho}}_{\sim 1}\ \frac{T_v{}'}{T_v} \tag{1.2.13}$$

$$= g\frac{T_v{}'}{T_v} \tag{1.2.14}$$

Scale analysis (not shown) reveals that the first term on the R.H.S. is related to the propagation of sound waves through the fluid and is relatively small. Hence, the density perturbation is largely contributed by the virtual temperature perturbation. Equation (1.2.13) indicates that a positive temperature anomaly leads to a positive buoyancy acceleration.

1.2.2 Quantifying atmospheric instability

An atmospheric state conducive to convection is referred to be unstable. Atmospheric instability can be quantified by the total buoyancy acceleration an air parcel encounters during an ascent, via

$$\frac{Dw}{Dt} = g\frac{T_v{}'}{T_v} \tag{1.2.15}$$

Recognising that

$$\frac{Dw}{Dt} = \frac{Dw}{Dz}\frac{Dz}{Dt} = w\frac{Dw}{Dz} \tag{1.2.16}$$

the change in vertical velocity due to buoyancy over a vertical distance z is given by

$$\int w\,dw = g\int \frac{T_v{}'}{T_v}\,dz \tag{1.2.17}$$

Integrating Equation (1.2.17) yields the relationship

$$\frac{1}{2}{w_{z_2}}^2 - \frac{1}{2}{w_{z_1}}^2 = g\int_{z_1}^{z_2} \frac{T_v{}'}{T_v}\,dz \tag{1.2.18}$$

Equation (1.2.18) implies that the vertical velocity of an unstable air parcel is governed by the contribution from buoyant energy and the initial vertical kinetic energy. In addition, it implies that an air parcel can overshoot into stable environment given sufficient vertical velocity.

1.2.3 The role of moist processes

Moist convection differs from its dry counterpart due to phase changes of water vapour taking place in ascending air. Saturation is defined as the equilibrium between the rates of evaporation and condensation. The vapour pressure at which saturation occurs is known as the saturation vapour pressure. It is a function of temperature and is governed by the Clausius-Clapeyron relation defined as follows:

$$e_s = e_0 \exp\left\{\frac{L}{R_v}\left(\frac{1}{T_0} - \frac{1}{T}\right)\right\} \tag{1.2.19}$$

where R_v is the specific gas constant for water vapour, and e_0 is the reference saturation vapour pressure at the reference temperature T_0.

In an ascending (and thus cooling) parcel, saturation occurs when the saturation vapour pressure is reduced to the vapour pressure of water vapour, forming cloud droplets and eventually rain drops if cooling continues. Latent heat is released during condensation and reduces the rate of cooling during the ascent (known as the lapse rate). This increases the density perturbation of the air parcel and thus its buoyancy acceleration. This is further discussed in the next section.

1.3 Characteristics of atmospheric convection

An atmospheric convective cell consists of three major components, namely the convective updraught, convective downdraught and the ambient compensating subsidence (Byers and Braham Jr, 1948; Emanuel et al., 1994; Smith, 2013; Plant and Yano, 2015). Each component is discussed in turn below.

1.3.1 The convective updraught

A convective updraught is a column of warm and moist air rising through the atmosphere. It is the direct response to atmospheric instability as explained in the previous section. Its thermodynamic trajectory on a tephigram, as shown in Figure 1.1, can be divided into two components, namely the dry ascent and the moist ascent. As a starting point, it is often assumed that the convective updraught is either adiabatic (i.e. no heat exchange between updraught and environment) or pseudo-adiabatic (i.e. no heat exchange processes other than that of latent heat between the updraught and environment).

1.3.1.1 Dry ascent

The dry stage is characterised by the thermodynamic profile of an unsaturated lifted parcel beneath the cloud base, or lifting condensation level (LCL) as shown in Figure 1.1. The profile is governed by the first law of thermodynamics:

$$dq = c_p dT - \alpha dp \tag{1.3.1}$$

where dq is the external heat exchange, c_p is the specific heat capacity of air at constant pressure, α is the specific volume (the reciprocal of density, $1/\rho$), dT is the change in temperature and dp is the change in pressure. For an adiabatic process, Equation (1.3.1) becomes

$$\frac{dT}{dp} = \frac{\alpha}{c_p} \tag{1.3.2}$$

Assuming the atmosphere is in hydrostatic balance and the pressure of the air parcel instantaneously adjusts to that of the environment, it follows that

$$\frac{dT}{dz} = \frac{dT}{dp}\frac{dp}{dz} = \frac{\alpha}{c_p}\left(-\rho g\right) = -\frac{g}{c_p} = -\Gamma_d \tag{1.3.3}$$

where Γ_d is known as the dry adiabatic lapse rate (DALR). For the atmosphere of the Earth, $c_p \sim 1000\,\mathrm{J\,kg^{-1}}$ and $g \sim 10\,\mathrm{m\,s^{-2}}$, which yields $\Gamma_d \approx 10\,\mathrm{K\,km^{-1}}$, i.e. a lifting parcel cools by 1 K per 100 m before it reaches the LCL.

1.3.1.2 Moist ascent

Upon reaching the LCL, water vapour begins to condense into water droplets and latent heat is released. Assuming the process is pseudo-adiabatic, the first law of thermodynamics becomes

$$c_p dT - \alpha dp = -L dr_s \tag{1.3.4}$$

where $\epsilon = R_d/R_v$ is the ratio of specific gas constant of dry air to that of water vapour and $r_s = \epsilon e_s/(p - e_s)$ is the saturation water vapour mixing ratio. It follows that

$$c_p dT - \alpha dp = -L\left(\frac{\partial r_s}{\partial T}dT + \frac{\partial r_s}{\partial p}dp\right) \tag{1.3.5}$$

$$\left(c_p + L\frac{\partial r_s}{\partial T}\right) dT = \left(\alpha + L\frac{\partial r_s}{\partial p}\right) dp \tag{1.3.6}$$

Using Equation (1.3.6) and assuming hydrostatic balance, the moist adiabatic lapse rate is given by

$$\Gamma_w = g\frac{R_d T^2 + LrT}{c_p R_d T^2 + L^2 r\epsilon} \tag{1.3.7}$$

where $r = \epsilon e/(p-e)$ is the water vapour mixing ratio of the air parcel. Although Γ_w varies with temperature and mixing ratio, the multiplication factor ≤ 1 guarantees that $\Gamma_w < \Gamma_d$. Thus, the rate of cooling reduces above the LCL as latent heat is released, before $\Gamma_w = \Gamma_d$ at the limiting case $r = 0$ (i.e. all water vapour is condensed into liquid) as shown by the moist adiabats (thermodynamic trajectory of pseudoadiabatic process) on Figure 1.1.

1.3.1.3 CAPE and CIN

Depending on the thermodynamic profile of the atmosphere, buoyancy may change sign along the ascent. This may be easily identified on a tephigram by comparing the updraught trajectory with the temperature profile of the environment, as shown in Figure 1.1.The area bounded by the updraught trajectory and environmental trajectory is proportional to its buoyant energy. Positive buoyant energy, represented by areas bounded by environment temperature profile and parcel temperature trajectory where $T_p > T_e$, is known as convective available potential energy (CAPE), while its negative counterpart is known as convective inhibition (CIN). For an atmospheric profile where there is only one layer of CAPE above one layer of CIN, the lower height bound of CAPE is known as the level of free convection (LFC), while the upper bound is known as the equilibrium level (EL). As shown in section 1.2.2, the buoyant energy is conveniently expressed in terms of virtual temperature. Hence,

$$\text{CAPE} = \int_{\text{LFC}}^{\text{EL}} -g\left(\frac{T_{v_{\text{parcel}}} - T_{v_{\text{env}}}}{T_{v_{\text{env}}}}\right) dz \tag{1.3.8}$$

$$\text{CIN} = \int_{z_{\text{BL}}}^{\text{LFC}} g\left(\frac{T_{v_{parcel}} - T_{v_{env}}}{T_{v_{env}}}\right) dz \tag{1.3.9}$$

where z_{BL} is the height of the boundary layer top (See section 1.4.1). As the name suggests, CIN acts to delay or inhibit the onset of convection so that CAPE is not immediately available to generate convection.

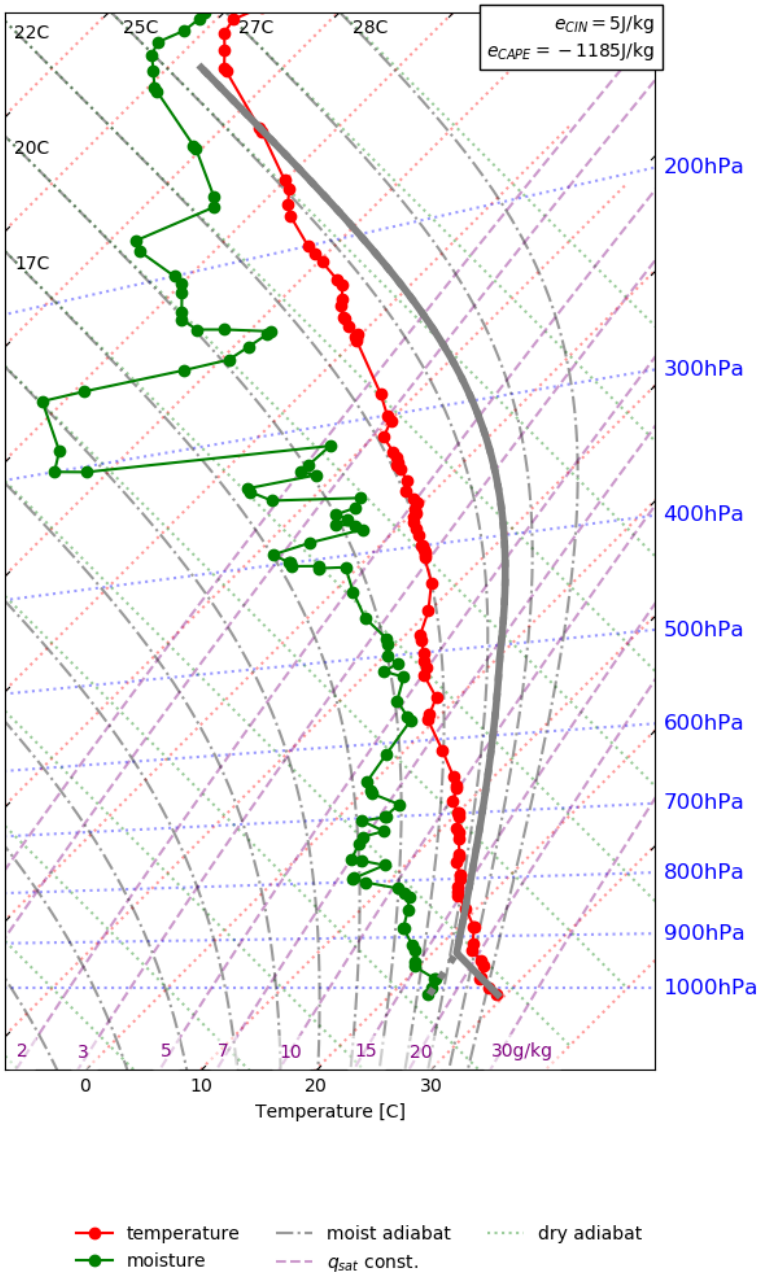

Figure 1.1: *A sample tephigram of a convective atmospheric profile with key metrics annotated.*

1.3.1.4 Entrainment and detrainment

While the parcel perspective assumes an ascent is isolated from its surroundings, a real convective updraught is diluted due to mixing of air with the environment. The intrusion of environmental air into the updraught is known as entrainment and the reverse is known as detrainment. At the cloud base, environmental air entrains into the updraught. At the cloud top, cloudy air detrains away from the convective updraught. This is known as forced detrainment and governs the outflow

of the convective updraught at cloud top.

Since environmental air is typically drier and cooler than the updraught, entrainment tends to cool and dry the updraught. At the same time, the environment is conditioned by detrained moist and warm air from the updraught. Each process acts to reduce the buoyancy of the updraught, resulting in a shallower and weaker updraught compared to the idealised parcel ascent. However, detrainment of shallow convection increases the specific humidity via evaporation of cloud droplets into the unsaturated environment. This reduces the negative effect of entrainment and is found to play an important role in the late onset of deeper convection (Blyth and Latham, 1993; Brown and Zhang, 1997; Bechtold et al., 2004b; Cetrone and Houze Jr, 2006).

1.3.2 Convective downdraught

A convective downdraught is a column of cool, dry and rapidly descending air from a convective cloud caused by the evaporation of water droplets and rain drag. Upon reaching the surface, the downdraught diverges into a cold pool, the enclosing boundary of which is known as gust fronts (Wakimoto, 1982; Mahoney III, 1988; Henneberg et al., 2020). Depending on the intensity of the downdraught and the surface mean wind, convective gusts could reach up to 49 m s^{-1} and cause damages (Nakamura et al., 1996). In addition, enhanced convergence near the surface gust front could also trigger new convection (Weisman and Klemp, 1986; Kingsmill, 1995; Abulikemu et al., 2019). Thus, convective downdraught is an important factor towards predicting the onset of convection.

Similar to the moist phase of the convective updraught, a convective downdraught may reasonably be idealised as a pseudo-adiabatic descent such that its temperature profile follows a pseudo-adiabat on a tephigram (Gilmore and Wicker, 1998; Market et al., 2019). The area on the tephigram bounded by the environment temperature profile and the parcel temperature trajectory where $T_p < T_e$, is known as downdraught convective available potential energy (DCAPE) (Li, 2004).

1.3.3 Compensating subsidence

Compensating subsidence is the downward motion observed in the cloud-free environment which compensates for the net upward convective motions (Bretherton and Smolarkiewicz, 1989). As a convective updraught reaches the tropopause and detrains into the surrounding atmosphere, gravity waves with alternating upward and downward motions are generated and propagate away from the convective cloud. Downward branches, associated with upper-level horizontal convergence, induce

downward motions over an extensive area at a relatively slow rate. The typical vertical velocity of compensating subsidence is $O(0.1\ \mathrm{m\ s^{-1}})$. Compensating subsidence removes instability by warming the large scale environment which reduces the buoyancy of ascending parcels.

1.4 The diurnal cycle of convection

The diurnal cycle of convection is the change of convection over a day driven by the diurnal variation of solar radiation and the associated surface heating (Soden, 2000; Hendon and Woodberry, 1993; Chaboureau et al., 2004). As the surface of the Earth absorbs solar radiation, convective instability grows as the boundary layer heats up. The convection later subsides towards sunset when the boundary layer begins cooling as a result of radiation. Since the land has a lower specific heat capacity than the ocean, the diurnal cycle of convection is significantly more pronounced over land than the ocean (Yang and Slingo, 2001; Zhang and Klein, 2010). To understand this phenomenon, one must understand how the convective boundary layer evolves during the day.

1.4.1 The convective boundary layer

The boundary layer is the lowest part of the Earth's atmosphere in direct contact with the surface and its structure and characteristics are directly influenced by surface processes including surface energy fluxes and friction (Clarke, 1970; Stull, 1988). It is characterised by turbulence as the air flow is disrupted by surface friction, obstacles (such as vegetation, trees, topography and settlements) and thermals, which are columns of rising air in the boundary layer due to solar heating. It is primarily turbulence which redistributes and transports heat and moisture within the boundary layer (Garratt, 1994).

The boundary layer is typically convective during the daytime when radiation from the sun heats up the surface of the Earth (Kaimal et al., 1976; Yang et al., 2004). Figure 1.2 shows the typical structure of the convective boundary layer, which is vertically partitioned into three layers with distinctive characteristics (Stull, 1988):

- The surface layer

  The surface layer is the lowest part of the convective boundary layer in direct contact with the surface. It is superadiabatic, indicating net upward sensible heat flux (i.e. the surface heats the air above). Moisture also decreases of with height, which indicates a net upward

transfer of moisture (i.e. surface moistens the air). Furthermore, this layer is characterised by strong shear of the horizontal wind with height due to surface friction. Both the buoyancy and shear contribute to the generation of turbulence. The vertical profiles are governed by the Monin-Obukhov Similarity Theory (Monin and Obukhov, 1954).

- The mixed layer

  Located above the surface layer, the mixed layer is dominated by convective overturning. Turbulence is predominantly produced via buoyancy and mixing leads to small variations of thermodynamic variables in the vertical.

- The entrainment zone

  The entrainment zone is the buffer between the boundary layer and the free troposphere, where convective overturning is dampened by negative buoyancy due to the stable condition of the free troposphere marked by increasing potential temperature with height. Boundary layer thermals with high vertical momentum are able to overshoot into the free troposphere. This penetration leads to mixing of boundary layer air into the free troposphere as well as entrainment of free tropospheric air downward into the mixed layer. Moisture decreases rapidly with height while wind speed increases sharply with height.

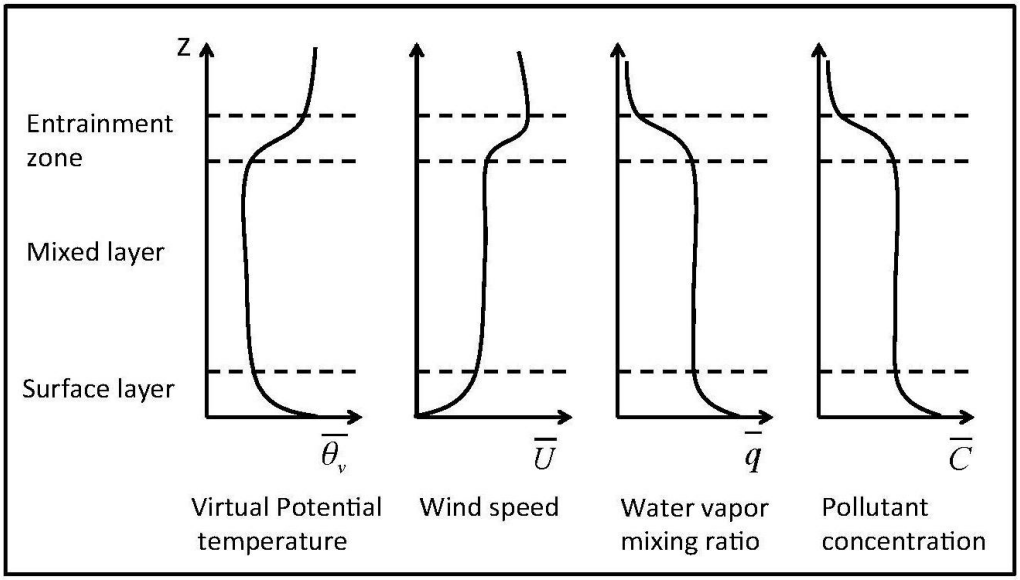

Figure 1.2: *The vertical profile of the daytime convective boundary layer. From Stull (1988).*

1.4.1.1 The evolution of the daytime convective boundary layer

As the energy flux into the boundary layer originates from the surface via absorption of solar radiation, it is important to understand the energy exchange at the surface. The surface energy budget is governed by (Stull, 1988; Flerchinger et al., 1996; Senay et al., 2007; Timmermans et al., 2007):

$$R_n - G_0 = H + \lambda E \tag{1.4.1}$$

where R_n is the net surface irradiance representing the net radiation gained or lost at the Earth's surface, G_0 is the ground heat flux, H and λE are the sensible and latent heat fluxes respectively which are defined as (Stull, 1988; Grant, 1997):

$$H = \rho c_p \overline{w'\theta'} \tag{1.4.2}$$

$$\lambda E = \rho L \overline{w'q'} \tag{1.4.3}$$

where $\overline{w'\theta'}$ and $\overline{w'q'}$ are the eddy covariances between perturbation vertical velocity w and potential temperature θ and specific humidity q. The definitions of H and λE are based on Reynolds averaging at the surface where the mean vertical velocity $\overline{w}$ is zero.

R_n exhibits a diurnal cycle peaking at local midday when the solar zenith angle is at the minimum. $R_n - G_0$ is known as the available energy from the sun into the atmosphere, which is partitioned into H and λE. Thus, the evolution of H and λE follow the diurnal cycle exhibited by R_n.

As turbulence is mainly driven by buoyancy in the CBL, convective overturning becomes increasingly rigorous as H increases during the day due to surface heating. The depth of the boundary layer exhibits a diurnal cycle as shown in Figure 1.3, which is divided into the following four stages (Stull, 1988):

1. Formation of the initial shallow mixed layer

   At sunrise, the surface layer begins to heat up and convective overturning commences. Yet, thermals are initially unable to reach the well-mixed neutral residual layer due to inversion through the stable nocturnal boundary layer, resulting in a slow growth of the mixed layer.

2. Rapid growth

   The initial shallow well-mixed layer warms and becomes coupled with the residual layer where boundary layer thermals begin penetrating into. This results in the rapid deepening of

the boundary layer.

3. Quasi-constant phase

   As the thermals reach the capping inversion, vertical motion is dampened. As thermals overshoot into the capping inversion, entrainment is induced and free tropospheric air subsides into the boundary layer and therefore prevents additional deepening of the boundary layer.

4. Decay

   Upon sunset, the surface layer begins to cool and the nocturnal stable layer forms. Surface-based convective overturning ceases and the well-mixed layer decouples from the surface to become the residual layer, marking the breakdown of the convective boundary layer.

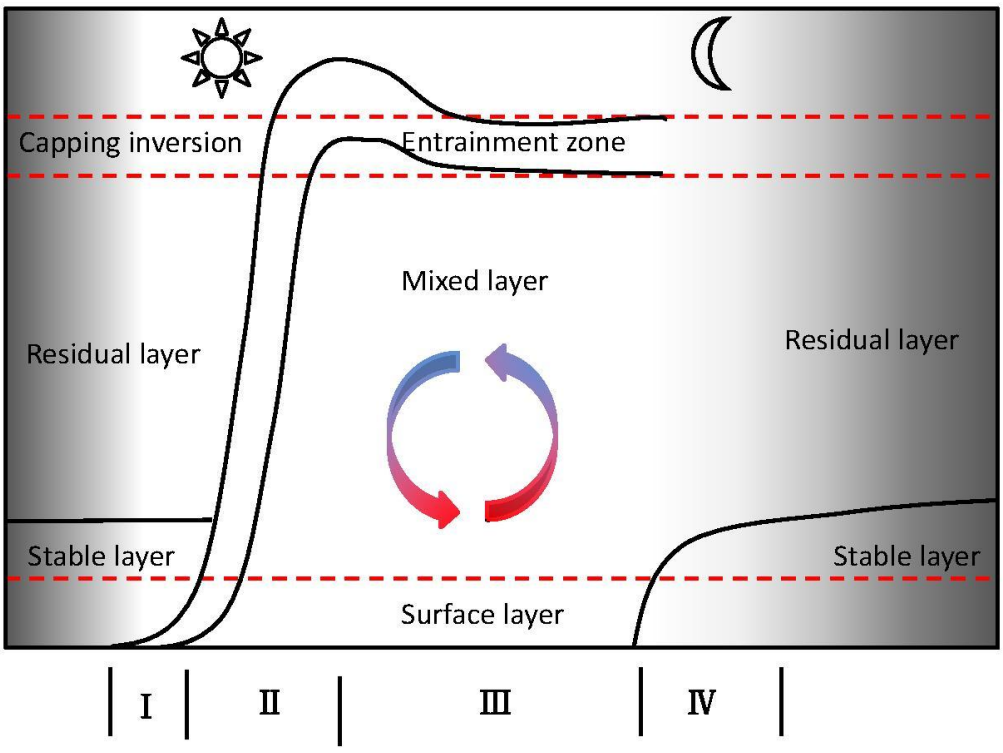

Figure 1.3: *The evolution of the convective boundary layer. From Stull (1988).*

1.4.1.2 The role of boundary layer thermals in triggering moist convection

If the boundary layer is sufficiently moist, cumulus clouds can form as thermals reach their respective lifting condensation levels (LCL). Boundary layer thermals contribute to the formation of three types of clouds defined by Gentine et al. (2013b):

- Forced clouds

  While a thermal may reach its LCL, it may not be able to reach its level of free convection (LFC) due to insufficient positive buoyancy in spite of the release of latent heat. Clouds associated with this type of thermal are classified as forced clouds as they rely on the continued forcing by the parent thermals to exist. They are largely present in the capping inversion.

- Active clouds

  If a thermal is sufficiently strong to reach LFC after reaching its LCL, an active cloud is triggered. Clouds of this nature create their own pressure perturbations in the horizontal, leading to the establishment of a convective circulation even in the absence of the parent thermal. Thus, active clouds may exist beyond the lifetime of the boundary layer thermals responsible for triggering them. In addition, air leaves the mixed layer into the free troposphere, which decreases the rate of growth of the boundary layer.

- Passive clouds

  Active clouds may decouple from the mixed layer upon maturity; air is no longer drawn from the mixed layer into the cloud base. Thus, cloud near to its original base dissipates via evaporation and gradual mixing with the environment.

1.4.2 The significance of the diurnal cycle

Over the tropics where other types of convective forcing (such as large-scale mechanical lifting and cold fronts) are absent, surface heating is the main driver of convection (Hendon and Woodberry, 1993). As boundary layer thermals become increasingly energetic due to increasing solar heating during the first part of the day, the strength and coverage of associated moist convection also increases (Hendon and Woodberry, 1993). Thus, surface-based convective activities exhibit a diurnal cycle coupled with that of the convective boundary layer (Yang and Slingo, 2001). The existence of the capping inversion means that the onset of convection is often delayed or suppressed, allowing instability to accumulate before convection initiates (Yang and Slingo, 2001). Therefore, continental convection is sometimes more vigorous than its marine counterpart, and is often known as ‘afternoon thunderstorms’ (Chen et al., 2014). An extreme and example of capped convection is the severe weather outbreaks in central United States. In spring, intense heating over the elevated

terrain creates an elevated mixed layer as air moves east towards lower terrain. This acts as a strong capping inversion above the convective boundary layer over Central United States which allows instability to accumulate with CAPE reaching 5000 J kg^{-1} (Williams and Renno, 1993). The arrival of an upper level trough induces large-scale upward motion and cooling in the mid-to-upper troposphere. If the capping inversion weakens either due to sufficient surface heating or large-scale cooling, boundary layer thermals may overcome the layer of CIN and become extremely buoyant convective updraughts with vertical velocity exceeding 50 m s^{-1}, creating severe thunderstorms capable of producing hailstones the size of softballs (Barry and Chorley, 2009; Markowski and Richardson, 2011). With a favourable wind profile, thunderstorms may rotate to become supercells which are capable of producing tornadoes (Weisman and Klemp, 1986; Esterheld and Giuliano, 2008).

1.5 Modelling convection

1.5.1 The concept of parameterisation

The resolution defines the lower end of the range of scales a numerical model can simulate. Meteorological phenomena with characteristic length/time scales that are smaller/shorter than the spatial/temporal resolutions cannot be explictly represented by the model. As an example, if the horizontal grid-length is 10 km, the model is able to resolve the evolution of synoptic-scale (characteristic length scale = 1000 km) features such as cold fronts and Rossby waves, but not small-scale processes such as isolated convective cells (characteristics length scale = 1 km), boundary-layer turbulence (characteristic length scale = 1 mm to 1 km) and radiation (molecular scale). While increasing the resolution may allow the model to resolve some sub-grid features, this option is often infeasible due to the limitation in computation resources and heightened costs of the simulations.

However, as discussed below, unresolved processes have an important effect on resolved-scale behaviour and must be captured to obtain a good simulation at resolved scales. This has led to the introduction of parameterisation: the effect of these processes must be estimated based on the resolved flow. The properties of an unresolved feature (e.g. convective updraught, downdraught and compensating subsidence) are first estimated based on observed relationships between the resolved flow and the sub-grid process. The sub-grid feature is then represented as a forcing on the resolved flow based on how it is observed to modify the larger-scale environment. Despite its

empiricism, parameterisation is found to improve the performance of numerical simulations (e.g. Ooyama, 1964; Irannejad et al., 2003).

1.5.2 The 'grey-zone' of convective parameterisation

With a characteristic length scale of 1 km (Emanuel et al., 1994; Miyamoto et al., 2013; Houze, 2014), convection should be parameterised in models with grid-length greater than approximately 1 km. Its importance became more fully appreciated when Ooyama (1964) proposed and implemented a simple convective parameterisation based on the theory of Conditional Instability of Second Kind (CISK, Charney and Eliassen, 1964) and led to the first successful simulation of tropical cyclone development at $\Delta x \geq 50$ km. However, modern models are run at higher resolutions for better simulation of convective phenomena such as squall lines and thunderstorms (e.g. Weisman et al., 1997; Romero et al., 2001; Done et al., 2004). For instance, the UK Met Office operates a regional numerical weather forecasts for the British Isles (UKV) with varying resolutions down to a grid-length of 1.5 km using the Unified Model (Davies et al., 2005). As the grid-length approaches 1 km, part of the spectrum of convective motions may be represented explicitly by the model dynamics, a regime for which conventional convective parameterisation schemes (convection schemes hereafter) are not designed. This implies that employing conventional schemes at such resolutions may yield undesired representation of convection such as scale-dependence of results (see Chapter 2 for further discussion). The range of resolutions within which convection is partially resolved is known as the 'grey-zone' of convective parameterisation.

1.6 Project motivation

Given that convection affects the evolution of the atmosphere and can bring significant weather risks, it is important to simulate convection correctly for accurate forecasts and research. Responding to the movement of modelling at kilometre-scale resolutions, it is worthwhile to explore a solution to the 'grey-zone' problem in convective parameterisation when:

- neither the use of conventional schemes nor no scheme is a reasonable approach in the 'grey-zone' (shown in Chapter 6);
- simulating at O (100 m) to fully resolve convection (Bryan and Rotunno, 2005; Petch, 2006) may not become practical in the near future (especially for climate modelling); and

- there is a demand for good ensemble numerical weather predictions at 'grey-zone' resolutions.

Another motivation comes from the fact that conventional schemes produce convection too early in a diurnal cycle (Yang and Slingo, 2001; Lean et al., 2008) (see Chapter 2 for detailed discussions). Given its significance, as discussed in Section 1.4.2, improving the simulation of the diurnal cycle at 'grey-zone' resolution would be an important goal for the project.

1.7 Research aim

The aim of this project is to develop a new scheme to parameterise convection in 'grey-zone' simulations in order to improve simulations of the diurnal cycle of convection over land. Thus, the objective of this research is to better predict the onset time and strength of the convective diurnal cycle over land. Through this approach, this research focuses on answering two research questions:

1. Is it possible to construct a convection scheme that produces results that are relatively resolution independent in the 'grey-zone'?
2. Is an accurate parameterisation of boundary layer turbulence important for a successful simulation of diurnal cycle of convection in the 'grey-zone'?

1.8 Chapter summary

This chapter has introduced the characteristics and physics of moist convection in the atmosphere, followed by the concept of convective parameterisation and the 'grey-zone', and a justification of the motivation and necessity of this project. The following chapter will describe the conventional convective parameterisation approach, including the underlying non scale-aware assumptions and how they ultimately lead to unrealistic representation of convection in simulations at 'grey-zone' resolutions.

Chapter 2

The conventional convective parameterisation

2.1 Introduction

Prior to finding a solution, it is important to explain the problems of conventional convection schemes when implemented in simulations at 'grey-zone' resolutions. This chapter describes in detail the underlying conventional assumptions made for convective parameterisation and identifies the limitations of these assumptions in the 'grey-zone'. Section 2.2 describes the conventional assumptions on the interactions between sub-grid plumes and the resolved-scale flow. Section 2.3 introduces the conventional algorithms of triggering a convection scheme (a.k.a. trigger functions). Section 2.4 identifies how the traditional assumptions are violated when the resolution of the simulation increases.

2.2 Representing the cloud-environment interactions

2.2.1 Determining properties of sub-grid updraughts

Instead of scenario-specific approaches (e.g. Yanai, 1971; Bates, 1972; Ogura, 1972), Arakawa and Schubert (1974) proposed a generalised convection scheme by evaluating the effect of an ensemble of cumulus clouds on the large-scale environment, after Gray (1972) showed that detrainment is the primary mechanism through which cumulus clouds modify the static energy and moisture of the surrounding environment. Arakawa and Schubert (1974) emphasised that for the entire cloud

ensemble, the detrainment rate D is related to the entrainment rate E and its mass flux M_c via the mass continuity equation, *i.e.*

$$E - D = \frac{\partial M_c}{\partial z} + \rho \frac{\partial \sigma_c}{\partial t} \tag{2.2.1}$$

where

$$M_c = \sum_i M_i = \sum_i \rho w_i \tag{2.2.2}$$

where w_i is the vertical velocity of an individual convective updraught i and σ_c is the fractional area covered by cumuli. As there exist various cloud types λ in a cumulus ensemble, M_c may also be expressed as the integral of mass fluxes across all cloud type, i.e.,

$$M_c = \int M(\lambda)\, d\lambda \tag{2.2.3}$$

Assuming $\partial \sigma_c / \partial t = 0$, $\partial M_c / \partial z$ could be diagnosed via Equation (2.2.1). For parameterisation, M_c must be expressed in terms of large-scale processes. Arakawa and Schubert (1974) normalised M_c by the mass flux at cloud base M_b and argued that the mass flux distribution of a cumulus ensemble should be related to the kinetic energy budget of convective updraughts, i.e.,

$$\frac{dK(\lambda)}{dt} = A(\lambda) M_b(\lambda) - D(\lambda) \tag{2.2.4}$$

where $K(\lambda)$ is the kinetic energy of convective updraughts and $D(\lambda)$ is its dissipation rate. The first term on the R.H.S. of (2.2.4) denotes the generation of $K(\lambda)$, which is calculated as the work done by buoyancy force. They coined the term $A(\lambda)$ the cloud work function and define it as:

$$A(\lambda) = \int_{z_B}^{z_D(\lambda)} \frac{g}{c_p \overline{T}(z)} \eta(z, \lambda) [s_{vc}(z, \lambda) - \overline{s}_v(z)]\, dz \tag{2.2.5}$$

where s_{vc} and $\overline{s}_v$ are the virtual dry static energy of the cloud and the environment respectively, and $\eta(z, \lambda)$ is the normalised time-averaged mass flux distribution.

Without an existing theory which relates the convective mass flux distribution to a single cloud work function, Arakawa and Schubert (1974) assumed that the number of sub-grid convective clouds is sufficiently large so that the average properties of local sub-grid plumes equal the ensemble mean. This simplification was sensible for simulations at their time with grid lengths of order O(100 km). This allowed Arakawa and Schubert (1974) to assume that all sub-grid updraughts at any given

time may be represented by a bulk plume, and thus

$$\int M_b(\lambda)\, d\lambda \approx N_{\mathrm{sp}} \overline{M_b} \tag{2.2.6}$$

where N_{sp} is the number of sub-grid plumes (which is effectively σ_c) and $\overline{M_b}$ is the cloud base mass flux of the bulk plume.

To determine σ_c (a.k.a. the closure problem), Arakawa and Schubert (1974) examined the budget of the cloud work function

$$\frac{dA}{dt} = \left.\frac{dA}{dt}\right|_{\mathrm{C}} + \left.\frac{dA}{dt}\right|_{\mathrm{LS}} \tag{2.2.7}$$

where the subscripts C and LS refer respectively to cloud-scale and large-scale processes. The consumption of cloud work function by clouds occurs with a time-scale of the life cycle of a cloud. Arakawa and Schubert (1974) assumed that this time-scale, which they referred to as the convective adjustment time-scale, is much shorter than that of the production of cloud work function by large-scale processes. Although the large-scale forcing can vary with time and the exact balance between consumption and generation will never be reached, Arakawa and Schubert (1974) argued that the large-scale forcing is only relevant over the period characterised by the adjustment time-scale. The dependence of convection on the past history of the large-scale forcing vanishes when τ_{LS}, the time scale of the large-scale forcings, is significantly larger than τ_{C}, the convective adjustment time-scale. In other words, the amplitude of the convective response may be estimated with the current large-scale forcing only since the sub-grid convection reacts sufficiently quickly to remove the cloud work function (i.e. instability) that is being generated by large-scale processes, i.e.

$$\frac{dA}{dt} = 0 \tag{2.2.8}$$

Under these assumptions, the state of the sub-grid cumulus ensemble follows a sequence of quasi-equilibria with the large-scale forcing. Arakawa and Schubert (1974) coined this assumption the 'quasi-equilibrium assumption', and it became the fundamental concept of closure for later convective parameterisation techniques. In addition to closing the parameterisation, the quasi-equilibrium assumption also enables the estimation of properties of the cloud ensemble based on a steady-state (i.e. fully developed) plume. This is realistic as long as $\tau_{\mathrm{LS}} \gg \tau_{\mathrm{c}}$ such that sub-grid clouds are able to complete their full life cycle in less than τ_{LS}. As a consequence, the properties of the bulk plume can be diagnosed based on the current large-scale environment, further simplifying

the parameterisation problem.

Another consequence of impairing the quasi-equilibrium assumption is that the model dynamics should not be able to generate explicit convection at the resolved scale. This is because the quasi-equilibrium assumption ensures that nearly all of the instability is removed by sub-grid convection such that the resolved flow is always convectively stable. For simulations with grid lengths greater than 10 km, this consequence is desirable since it is unrealistic to represent any resolved convective updraught with such a scale. In other words, the quasi-equilibrium assumption implies that convection is exclusively represented by the convection scheme by suppressing explicit convection.

2.2.2 *Modelling compensating subsidence*

To parameterise its stabilisation effect of compensating subsidence on the resolved scale flow, Arakawa and Schubert (1974) made use of two observations about the relationship between the sub-grid convection and the large-scale environment. The first is that over a large area, convection only occupies a small fractional area while the majority of the convective area is dominated by the dry environment in which compensating subsidence takes place, i.e.

$$\sigma_c \ll 1 \tag{2.2.9}$$

The second assumption is that the net mass flux is zero over the area represented by a grid box as a result of continuity, which Arakawa and Schubert (1974) enforced within each grid column. In other words, all compensating subsidence occurs in the same grid-column as the driving convection and reduces convective parameterisation to a one dimensional problem.

With these two assumptions, the magnitude of the compensating subsidence at each height is given by

$$w_e(z) = \frac{(\overline{w}(z) - \sigma_c w_c)}{1 - \sigma_c} \tag{2.2.10}$$

where z is the height, w is the vertical velocity, σ is the fractional area, the overbar signifies the grid-mean value and the subscript e refers to the dry environment.

2.2.3 *Calculating the forcing on the resolved-scale flow*

Arakawa et al. (2011) considered that the grid-mean value of an arbitrary quantity $\bar{\psi}$ is the combined

effect of a convective contribution ψ_c and the environmental contribution $\tilde{\psi}$, i.e.

$$\bar{\psi} = \sigma_c \psi_c + (1 - \sigma_c)\tilde{\psi} \tag{2.2.11}$$

This is true for w and for the vertical transport of the quantity $w\psi$, *i.e.*

$$\overline{w} = \sigma_c w_c + (1 - \sigma_c)\tilde{w} \tag{2.2.12}$$

$$\overline{w\psi} = \sigma_c w_c \psi_c + (1 - \sigma_c)\tilde{w}\tilde{\psi} \tag{2.2.13}$$

Taking the Reynolds averaging of the vertical eddy transport of ψ yields

$$\overline{w\psi} - \bar{w}\bar{\psi} = \sigma_c(1 - \sigma_c)(w_c - \tilde{w})(\psi_c - \tilde{\psi}) \tag{2.2.14}$$

Given a grid length Δx which is substantially greater than the characteristic horizontal length scale of a single plume x_i, *i.e.*

$$x_i \ll \Delta x \tag{2.2.15}$$

it follows that the total area of the convective plume is significantly smaller than the area of the grid box $(\Delta x)^2$. If the total area of all convective plumes A_c is also small, it follows that

$$\sigma_c = \frac{A_c}{(\Delta x)^2} \ll 1 \tag{2.2.16}$$

For the regime in which σ_c is small, (2.2.12) can be approximated as

$$\overline{w} \approx \tilde{w} \tag{2.2.17}$$

Since the vertical velocity in a convective updraught is of the order of 10 m s^{-1} and the synoptic scale vertical velocity is of the order of 1 cm s^{-1}, $\tilde{w} \ll w_c$ and it follows, according to (2.2.17), that

$$\overline{w} \ll w_c \tag{2.2.18}$$

This allows the effect of convection to be represented by the convective flux of ψ via

$$\rho\left(\overline{w\psi} - \bar{w}\bar{\psi}\right) = \rho\sigma_c w_c(\psi_c - \tilde{\psi}) \tag{2.2.19}$$

where ρ is the density of air. It follows that the tendency of ψ due to sub-grid convection is given by

$$\left.\frac{\partial \psi}{\partial t}\right|_{\text{conv}} = -\frac{1}{\rho}\frac{\partial}{\partial z}\left[\rho\left(\overline{w\psi} - \bar{w}\bar{\psi}\right)\right] = -\frac{1}{\rho}\frac{\partial}{\partial z}\left[\rho\sigma_c w_c(\psi_c - \tilde{\psi})\right] \tag{2.2.20}$$

This equation implies that if the cumulative mass flux due to all sub-grid convection is known, its effect on the large-scale atmosphere can be represented. Together with the ensemble assumption, this assertion gives rise to the ensemble bulk plume approach, which represents the entire population of convective elements within the grid box as one single bulk convective plume. The advantage of such an assumption is that one can simply calculate the convective characteristics (ψ_c and $\rho\sigma_c w_c$) of the bulk plume instead of performing an averaging of some assumed distributions of convection.

A typical implementation of the conventional convective parameterisation is as follows (Fritsch and Chappell, 1980):

1. Calculate the properties of the bulk updraught, including temperature, moisture, cloud precipitates and vertical velocity.

2. Assuming a small fractional area, calculate the properties of the local compensating subsidence using the zero net mass flux argument.

3. Compute the new grid-mean values due to the effect from the bulk plume.

4. Iterate steps 1 - 3 until the closure assumption is satisfied, i.e. all instability generated by the large-scale within a time-step is removed.

2.2.4 Variations and refinements within the conventional framework

There have been some key developments based on the approach by Arakawa and Schubert (1974). Instead of the cloud work function, Fritsch and Chappell (1980) used CAPE to close their convection scheme. In their approach, the vertical profile of the bulk plume is calculated via an undiluted parcel ascent which originates from the surface if the triggering condition is satisfied (see Chapter 3). Fritsch and Chappell (1980) also used a microphysics scheme to calculate the properties of the bulk moist downdraught. Since moist downdraughts also act to stabilise the atmosphere, the inclusion of this feature led to a more realistic parameterisation. Their scheme iterates the parameterisation procedure until at least 90% of the instability generated by large-scale processes is removed, which is a relaxation of the quasi-equilibrium assumption.

Based on Fritsch and Chappell (1980), Kain and Fritsch (1990) adopted a steady-state entraining and detraining plume model to estimate the properties of the bulk plume for more realistic cloud-top heights. Instead of assuming a single entrainment/detrainment rate for the updraught, Kain and Fritsch (1990) introduced the buoyancy sorting entrainment/detrainment parameterisation, a concept based on the turbulent mixing between cloudy air and environmental air at the edge of clouds. Negatively buoyant mixtures leave the updraught and detrain into the environment while positively buoyant mixtures entrain into the updraught.

Kain and Fritsch (1990) began by estimating the rate at which dry environmental air mixes with the updraught air δM_{e} via

$$\delta M_{\mathrm{e}} = M_{\mathrm{u0}}(-0.03\delta p / R_{\mathrm{u}}) \tag{2.2.21}$$

where R_{u} is the radius of the updraught, M_{u0} is the cloud-base mass flux and δp is the vertical pressure interval between two model levels. The total rate of air entering the region in which mixing occurs δM_{t} is thus given by

$$\delta M_{\mathrm{t}} = \delta M_{\mathrm{e}} + \delta M_{\mathrm{u}} \tag{2.2.22}$$

where the subscript u denotes the property of the updraught. Suppose a probability distribution function $f(x)$ describing the frequency distribution of mixtures is known, it follows that

$$\delta M_{\mathrm{t}} \int_0^1 f(x)\, dx = \delta M_{\mathrm{e}} + \delta M_{\mathrm{u}} \tag{2.2.23}$$

which further implies that

$$\delta M_{\mathrm{e}} = \delta M_{\mathrm{t}} \int_0^1 x f(x)\, dx \tag{2.2.24}$$

$$\delta M_{\mathrm{u}} = \delta M_{\mathrm{t}} \int_0^1 (1-x) f(x)\, dx \tag{2.2.25}$$

The exact form of $f(x)$ was tunable and a sensitivity test was performed in Kain and Fritsch (1990).

Gregory and Rowntree (1990) proposed a similar scheme to that from Kain and Fritsch (1990). However, instead of sorting buoyancy on cloud-environment mixtures, they followed Simpson and Wiggert (1969) and Simpson (1971) to parameterise the entrainment rate ϵ as

$$\epsilon = \frac{0.2}{R_u} \tag{2.2.26}$$

and set $\epsilon = \delta$, where δ is the fractional entrainment rate. Gregory and Rowntree (1990) also differ from Arakawa and Schubert (1974), Fritsch and Chappell (1980) and Kain and Fritsch (1990) in the

closure assumption. Instead of closing the parameterisation with the quasi-equilibrium assumption, the initial cloud base mass flux M_{I} is set to be proportional to the buoyancy excess one layer below the initiation layer, i.e.

$$M_{\mathrm{I}} = 10^{-3} c\{[({\theta_v}^{\mathrm{P}})_{k-1} - ({\theta_v}^{\mathrm{E}})_{k-1} - b]/\Delta\sigma_{k-1}\} \tag{2.2.27}$$

where θ_v is the virtual temperature and the superscripts P and E denote "parcel" and "environment" respectively. b is a tunable constant representing the minimum buoyancy excess required to initiate the scheme. $\Delta\sigma$ is the interval between two σ-levels in a terrain following vertical grid and k labels the initial level. Gregory and Rowntree (1990) argued that this allows the initiation of sub-grid convection in the absence of large-scale forcing. However, these convective updraughts are likely to cease over a rather short time-scale as no large-scale forcing exists to maintain the availability of instability to further convective activities. Despite not explicitly enforced, Gregory and Rowntree (1990) showed that their approach would also achieve quasi-equilibrium.

2.3 Trigger function

In a convection scheme, the trigger function determines whether the scheme is activated in a grid column over a time-step. Although a mean profile may be stable, the use of a trigger function recognises that sub-grid variability may cause a fraction of a column to be favourable for deep convection. Conventional convection schemes incorporate threshold-based trigger functions, a few of which are described below.

2.3.1 Instability thresholds

A classic approach is to evaluate parameters associated with buoyant energy available since this must be present for convection to occur. Arakawa and Schubert (1974) selected the level of maximum moist static energy to be the source of sub-grid convection but did not specify a threshold for triggering the scheme. Moorthi and Suarez (1992) and Anderson et al. (2004) used a fixed value of cloud work function as the threshold for triggering the scheme, while Lee et al. (2007) opted to trigger convection if the lifting condensation level (LCL) of the lifted parcel is within 150 hPa of the surface. Zhang and McFarlane (1995) triggers their convection scheme if CAPE exceeds 70 J kg^{-1} based on an adiabatic parcel ascent originated from the level of maximum moist static energy below 600 hPa, while a threshold of the generation rate of CAPE by the large-scale advective processes is

also used instead as the triggering criterion in some studies (Xie and Zhang, 2000; Zhang, 2002; Zhang and Mu, 2005; Zhang and Wang, 2006; Wu et al., 2007; Song and Zhang, 2009; Zhang and Song, 2010). Simpler buoyancy-related trigger criteria have also been introduced. For instance, the Gregory and Rowntree (1990) scheme is triggered when an entraining parcel, lifted from any layer in the model with a positively perturbed temperature (0.2 K), remains buoyant with a temperature excess over 0.2 K at the next model level.

The presence of buoyant energy is necessary but not sufficient to initiate convection. Torn and Romine (2015) determined that the presence of CIN plays a role in delaying the onset of convection. Bennett et al. (2006) argued that dynamical factors such as convergence, upper-level forcings and orography also affect the initiation of convection. Hence, schemes which use instability alone as a trigger function may perform poorly in certain convective scenarios. For example, Lean et al. (2008) found that the scheme by Gregory and Rowntree (1990) led to early or unrealistic convective initiation in the diurnal cycle of convection where CIN is present.

2.3.2 Dynamical thresholds

Since dynamical forcing also plays an important role in triggering convection, an alternative approach is to trigger convection based on dynamical criterion. Fritsch and Chappell (1980) introduced a temperature excess threshold ΔT between an adiabatic lifted parcel and the grid-mean environment at the LCL as the triggering criteria for sub-grid deep convection. ΔT varies according to $\overline{w}$ (in cm s^{-1}) in the form of

$$\Delta T = -c_1 \overline{w}^{1/3} \tag{2.3.1}$$

where c_1 is a constant with dimensions °C s$^{1/3}$ cm$^{-1/3}$. Kain and Fritsch (1990) employed the same temperature perturbation approach but with a different quantification of ΔT of the form

$$\Delta T = k \left[\overline{w} - c(z) \right]^{1/3} \tag{2.3.2}$$

where k is a constant and $c(z)$ is the threshold vertical velocity which varies with height. Bechtold et al. (2001) employed a modified version of the temperature perturbation threshold which depends on a grid-mean vertical velocity normalised by the domain size of the simulation in the form

$$\Delta T = \frac{\overline{w}}{|\overline{w}|} c_w \left| \frac{\overline{w}\sqrt{A}}{\Delta x} \right| \tag{2.3.3}$$

where c_w is a constant, A is the size of the domain in km^2 and Δx is the grid-length of the simulation in km.

While the above schemes do take the dynamics of the resolved model state into account, they do not directly address the amount of resolved CIN. Deep convection initiates once the CIN layer is eroded by ascent cooling of the mid-troposphere or is breached by a sufficiently buoyant thermal. Donner (1993); Donner et al. (2001) introduced a trigger function which requires the time integrated large-scale forcing be sufficient to lift the parcel from its initiation level to the LFC, and that CIN must not exceed an arbitrary threshold (10 J kg^{-1} in the original scheme, modified to 100 J kg^{-1} by Wilcox and Donner (2007)).

2.3.3 Other types of thresholds

A modified version of the Zhang-MacFarlane scheme (Xie and Zhang, 2000; Zhang, 2002) requires the relative humidity at the initiating level of the parcel ascent to be greater than 80%. The original Tiedtke scheme (Tiedtke, 1989) also requires the lower level atmosphere to be sufficiently close to saturation, with a relative humidity of at least 90%. It also assesses the large-scale moisture convergence as an indicator for triggering convection, following studies which suggested that moisture convergence is an important quantity which controls convective activities (e.g Kuo, 1965, 1974).

2.4 Limitations of the conventional approach

2.4.1 The scale-unawareness of assumptions

Traditional assumptions on cloud-environment interactions are scale-dependent. Firstly, the number of clouds a grid box can accommodate is very limited for grid-boxes with grid-lengths of O(1 km). The deterministic bulk plume approach is unable to replicate variations among grid-columns due to sampling error (Craig and Cohen, 2006; Cohen and Craig, 2006) over a horizontally homogeneous domain. This may also be suppressed by threshold-based trigger functions which activates a convection scheme in all grid-columns with similar properties. This scale-unawareness has been found to prevent simulations from producing sensible wave spectra in the middle atmosphere (Ricciardulli and Garcia, 2000; Horinouchi et al., 2003), affecting the performance of models. Variability implies that local sub-grid plumes could also be in different stages of development, implying that the quasi-equilibrium may not hold over the local grid column. This suggests that

a steady-state solution from a deterministic closure becomes inappropriate to represent sub-grid convection in 'grey-zone' resolution simulations. Secondly, σ_c can approach unity at 'grey-zone' resolutions and enforcing Equation (2.2.10) for large values of σ_c will lead to very large w_e with very small σ_e. It also implies that convection is partially resolved at 'grey-zone' resolution and explicit convection could take place. Thus, the complete suppression of resolved convection due to the quasi-equilibrium assumption is no longer realistic.

2.4.2 The problem of the diagnostic nature

The negligence of the tendency term in Equation (2.2.1) makes convention schemes diagnostic; the properties of sub-grid plumes are parameterised based on the instantaneous state of the resolved-scale flow. For this to be realistic, a clear distinction between the convective-scale and large-scale tendencies is required, which Pan and Randall (1998) described as "ambiguous and subjective". The distinction becomes undefined at kilometre-scale simulations, making conventional schemes not appropriate for 'grey-zone' simulations.

2.4.3 Performance in simulations of the diurnal cycle

Conventional convection schemes are known to perform poorly in simulations of the diurnal cycle of convection over land, which is a case of non-equilibrium convection (Slingo et al., 1992; Betts and Jakob, 2002; Bechtold et al., 2004a). The common issue is that convection initiates too early in the diurnal cycle, which is a result of convection schemes responding immediately to the generation of CAPE by boundary layer forcings and neglecting the presence of CIN. For example, results from Lean et al. (2008) showed that at a grid-length of 4 km, the onset of convection from Gregory and Rowntree (1990) is approximately an hour earlier than radar observation as shown in Figure 2.1. In addition, the early removal of instability leads to a lower peak instability such that the strength of the convective activities are underestimated. This is also evident in Figure 2.1 where rain rate is weaker in the 4-km run. In addition, since the domain was not homogeneous (the study aimed to investigate how different approaches affect simulations of convection over the British Isles), the conventional scheme induced large horizontal temperature gradients at places. This in turn led to spurious local explicit convection (a.k.a. grid-point storms).

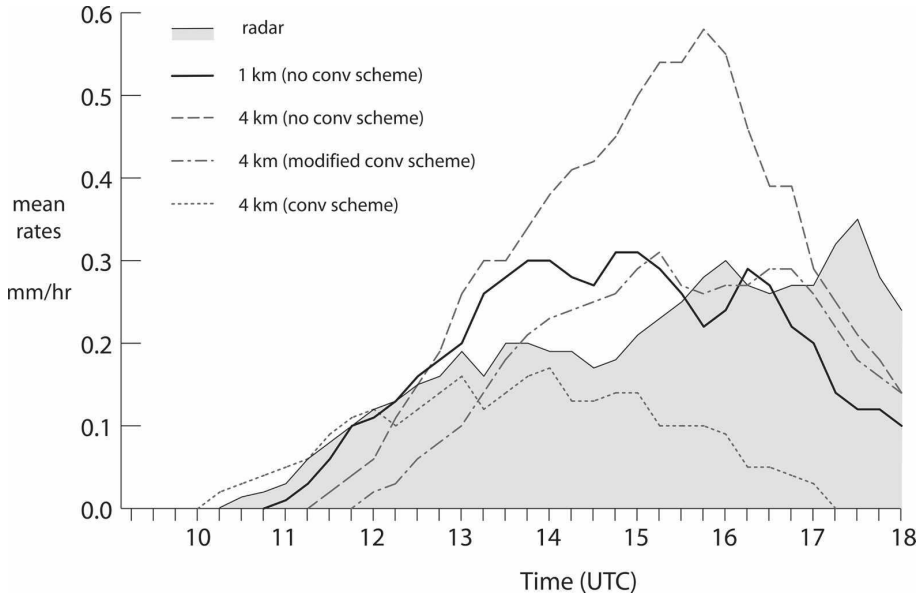

Figure 2.1: *Evolutions of precipitation in different simulations of a diurnal cycle of convection over the UK. From Lean et al. (2008)*

2.5 Chapter summary

This chapter has explained how the break-down of assumptions regarding the interactions between convection and the resolved-scale flow leads to poor performance of conventional schemes as the grid length approaches the length scale of a convective updraught. With convection partially resolvable, a 'grey-zone' convection scheme must separate the spectrum into the resolved and unresolved parts, and represent the unresolved range without fully suppressing explicit convection. Moreover, the convection scheme must also produce scale-dependent variability over a horizontally homogeneous domain to replicate sample error due to limited number of plumes over individual grid columns. The next chapter will discuss the latest efforts on parameterising convection in the 'grey-zone'.

Chapter 3

Existing 'grey-zone' convection schemes

3.1 Introduction

As discussed in Chapters 1 and 2, many conventional assumptions must be relaxed in order for a convection scheme to represent convection realistically in 'grey-zone' simulations. With this in mind, some newer schemes designed for the 'grey-zone' use relaxed or even new assumptions. This chapter discusses the development of 'grey-zone' convection schemes, focusing on closure and trigger functions in Section 3.2 and treatment of compensating subsidence in Section 3.3.

3.2 Non-equilibrium closure

3.2.1 Relaxed quasi-equilibrium approach

To improve the performance of conventional schemes in simulations of the diurnal cycle of convection, Bechtold et al. (2013) proposed a relaxation term in the quasi-equilibrium assumption such that

$$\left.\frac{\partial \mathrm{CAPE}}{\partial t}\right|_{\mathrm{CONV}} = -\frac{\mathrm{CAPE}}{\tau} - \alpha \frac{1}{T_*} \int_0^h \left.\frac{\partial T_v}{\partial t}\right|_{\mathrm{BL}} dz \tag{3.2.1}$$

where

$$\alpha = \frac{\tau_{\mathrm{BL}}}{\tau} \tag{3.2.2}$$

where τ is the convective adjustment time-scale, τ_{BL} is the boundary layer adjustment time-scale and h is the height of the boundary layer. T_* scales as $c_p^{-1}gh$. This closure prevents the convection scheme from always producing sub-grid convection which consumes all the CAPE generated by the large-scale forcings in the free troposphere. Bechtold et al. (2013) defined τ_{BL} as

$$\tau_{\mathrm{BL}} = \begin{cases} \tau_{\mathrm{c}} & \text{over land} \\ \dfrac{h_{\mathrm{cb}}}{\overline{u}_{\mathrm{BL}}} & \text{over water} \end{cases}$$

where τ_c is the convective overturning time-scale defined as $H/\overline{w_{\mathrm{u}}}$, with H being the average cloud depth and $\overline{w_{\mathrm{u}}}$ being the vertically averaged updraught velocity. h_{cb} is the height of the cloud base and $\overline{u}_{\mathrm{BL}}$ is the mean horizontal wind velocity in the sub-cloud layer. Rather than an assumed constant, Bechtold et al. (2013) defined τ as

$$\tau = \tau_{\mathrm{c}} f(n); f(n) = 1 + \frac{264}{n} \tag{3.2.3}$$

where n is the spectral truncation of the model simulation.

Two major concerns exist in the approach by Bechtold et al. (2013). Firstly, the definition of τ_{BL} is based on the overturning of an entire deep convective plume instead of the boundary layer thermals, which may not reflect the adjustment time-scale of the boundary layer. Secondly, their approach assumes a steady-state plume which always reaches its maximum height, which does not always hold as will be discussed in Section 3.2.3.

3.2.2 Stochastic closure

Stochasticity has been introduced in some convection schemes to promote variability in convective mass fluxes in smaller grids. Palmer (2001) employed a cellular automaton in a convection scheme, while Bright and Mullen (2002) introduced randomness in the trigger function of the Kain-Fritsch scheme (Kain and Fritsch, 1990). Majda and Khouider (2002) and Khouider et al. (2003) proposed a stochastic method to quantify the fractional area of sub-grid updraughts. Lin and Neelin (2003) proposed a modified version of the Zhang-McFarlane scheme (Zhang and McFarlane, 1995) which perturbed the assessed CAPE or derived vertical heating profile of sub-grid convection to produce variability. However, many of these perturbations are based on arbitrary assumptions on the temporal and spatial variability in the convective state, hence lacking the physical reasoning behind the perturbation and the appropriate scale-awareness.

Plant and Craig (2008) developed a stochastic CAPE closure, in which the convective response perturbation is based on the equilibrium statistics of convection from the CRM studies conducted by Cohen and Craig (2006). Craig and Cohen (2006) showed that for non-interacting clouds in equilibrium, the distribution of total cloud base mass flux $p(M)$ can be described by an exponential pdf with the equation

$$p(M) = \frac{1}{\langle m \rangle}\sqrt{\frac{\langle M \rangle}{M}}\exp\left(-\frac{M+\langle M \rangle}{\langle m \rangle}\right) \times I_1\left(\frac{2}{\langle m \rangle}\sqrt{\langle M \rangle M}\right) \tag{3.2.4}$$

where $\langle M \rangle$ is the ensemble mean total cloud base mass flux, $\langle m \rangle$ is the mean cloud-base mass flux of a single cloud and I_1 denotes the modified Bessel function of order 1. The large-scale environment is defined as the horizontal average of vertical thermodynamic and moisture profiles of the atmosphere over a region centred at each grid point. The size of the averaging region is set to be proportional to L^2, where $L = \sqrt{\langle m \rangle / \langle M \rangle}$ is a length scale which represents the separation distance between convective plumes. A spectrum of plumes with radii r ranging up to 2 km, which is binned into 50 equal intervals, is initiated with initial cloud base mass fluxes of each binned plume m varying by

$$m = \frac{\langle m \rangle}{\langle r^2 \rangle} r^2 \tag{3.2.5}$$

The profile of each plume is computed using the plume model employed in the Kain-Fritsch scheme and an initial guess of the total convective mass flux is obtained. The final total convective mass flux $\langle M \rangle$ is then obtained by scaling the initial guess such that at least 90% of the dilute CAPE is removed over the closure time-scale T_c, which is given by $T_c = kL$ where k is a tunable parameter with dimensions s m^{-1}.The equilibrium convective distribution is then obtained using (3.2.4) with the calculated value for $\langle M \rangle$ and an assumed value for $\langle m \rangle$. In addition, the probability of a plume with radius between r and $r + dr$ initiating in a single time step of duration dt is computed as

$$\langle N \rangle p(r) dr \frac{dt}{T} = \frac{\langle M \rangle}{\langle m \rangle}\frac{2r}{\langle r^2 \rangle}\exp\left(\frac{-r^2}{\langle r^2 \rangle}\right) dr \frac{dt}{T} \tag{3.2.6}$$

where $\langle N \rangle$ is the ensemble-mean number of convective clouds given by $\langle M \rangle / \langle m \rangle$, and T is the lifetime of a plume which is chosen to be 45 minutes. The large-scale tendencies due to the newly initiated population of sub-grid convection is then computed.

Plant and Craig (2008) is a first step towards the development of a fully scale-aware convection scheme for the 'grey-zone'. However, it is still based on the statistics of plumes in quasi-equilibrium.

Hence, the scheme might not perform well in non-equilibrium conditions such as the diurnal cycle of convection where significant CIN might be present. Since this project focuses on the diurnal cycle, other options must be explored.

3.2.3 Prognostic closure

To represent the evolution of sub-grid plumes in non-equilibrium cases, Pan and Randall (1998) derived a prognostic relaxation to the quasi-equilibrium assumption by Arakawa and Schubert (1974). They define the bulk convective kinetic energy (CKE) K as

$$K = \frac{1}{2}\int_{z_S}^{z_T} \rho_0 \overline{u_i^2}\, dz \tag{3.2.7}$$

where z_S and z_T are the heights of the surface and maximum cloud top respectively, ρ_0 is the reference state density and $\overline{u_i}$ is the mean three dimensional velocity vector of a convective updraught. It is important to realise that the bulk CKE includes kinetic energy from all components of the sub-grid convective ensemble, including convective updraughts/downdraughts and the horizontal wind.

By making an analogy to the budget equation for turbulent kinetic energy, Pan and Randall (1998) proposed that the evolution of CKE for each cloud type λ is governed by

$$\frac{\partial K(\lambda)}{\partial t} = B(\lambda) + S(\lambda) - D(\lambda) \tag{3.2.8}$$

where B is the buoyancy production term, S is the shear production term and D is the vertically-integrated dissipation term. Neglecting the shear production term and parameterising $D(\lambda)$ as $K(\lambda)/\tau_D$ where τ_D is the dissipation time-scale for CKE, Pan and Randall (1998) arrived at

$$\frac{\partial K(\lambda)}{\partial t} = M_B(\lambda)A(\lambda) - \frac{K(\lambda)}{\tau_D} \tag{3.2.9}$$

where $M_B(\lambda)$ is the cloud base mass flux and $A(\lambda)$ is the cloud work function introduced by Arakawa and Schubert (1974). Following Xu et al. (1992), M_B is parameterised as

$$M_B = \sqrt{\frac{K}{\alpha}} \tag{3.2.10}$$

where α is a parameter with unit $m^4\ kg^{-1}$ that governs the conversion coefficient from CKE to convective mass flux. The amount of sub-grid convection is then quantified according to the rate of

change of CKE obtained via Eq. (3.2.9). With their approach, the quasi-equilibrium assumption is relaxed as the prognostic closure allows the accumulation of CKE. In the limiting case that τ_D is sufficiently small, quasi-equilibrium becomes the steady-state solution of Pan and Randall (1998). However, similar to Bechtold et al. (2013)'s approach, Pan and Randall (1998) does not recognise the fact that the bulk ensemble does not reach the steady-state vertical extent instantly. Moreover, their parameterisation of the cloud-base mass flux, as well as the remaining parameterisation procedures, are based on the assumption that σ_{u} is small. Hence, although Pan and Randall (1998) offered the insight of a prognostic closure, it is not suitable as being a convection scheme for the 'grey-zone'.

Gerard and Geleyn (2005) also proposed a convection scheme with a prognostic closure. Rather than CKE, they derived prognostic equations for the fractional area and vertical velocity of updraughts based on the budget of moist static energy. Expressed in pressure coordinates, the evolution of the the relative vertical velocity of updraught ω^*_{u}, which is defined as $\omega_{\mathrm{u}} - \omega_{\mathrm{e}}$, is

$$\frac{\partial \omega^*_{\mathrm{u}}}{\partial t} = -\frac{g^2}{1+\gamma'}\frac{p}{R_{\mathrm{d}}}\frac{T_{\mathrm{v_u}} - \overline{T_v}}{\overline{T_v} T_{\mathrm{v_u}}} + \frac{\omega^{*2}_u}{p}\left\{1 + (\lambda_{\mathrm{u}} + \frac{K_{\mathrm{du}}}{g}) R_{\mathrm{d}} T_{\mathrm{v_u}}\right\} - \frac{1}{2}\frac{\partial \omega^{*2}_u}{\partial p} \tag{3.2.11}$$

where K_{du} is the aerodynamic friction coefficient, γ' is an apparent mass coefficient.

For the evolution of the updraught fractional area σ_{u}, Gerard and Geleyn (2005) followed the prognostic closure proposed by Chen (1991) and Bougeault (1985). The evolution of σ_{u} is governed by

$$\frac{\partial \sigma_{\mathrm{u}}}{\partial t}\int_{p_{\mathrm{t}}}^{p_{\mathrm{b}}}\left(h_{\mathrm{u}} - \overline{h}\right)\frac{\mathrm{d}p}{g} = L\int_{p_{\mathrm{t}}}^{p_{\mathrm{b}}}\sigma_{\mathrm{u}}{\omega_{\mathrm{u}}}^*\frac{\partial \overline{q}}{\partial p}\frac{\mathrm{d}p}{g} + L\cdot \mathrm{TMC} \tag{3.2.12}$$

where h is the moist static energy, q is the specific humidity and TMC is the total moisture convergence towards the local grid box.

Nonetheless, Gerard and Geleyn (2005) assumed other properties of the updraught, such as temperature and moisture, to be in steady-state such that they are diagnostic quantities. Most importantly, similar to Pan and Randall (1998), they assumed that the vertical cloud extent is always at steady-state, neglecting the time for the updraught to develop. Using a typical updraught velocity of 5 m s^{-1}, they estimated that the time required for the updraught to reach the top of the troposphere would be of the order 20 minutes. The large-scale adjustment time-scale due to the diurnal cycle is of the order 10 minutes, which is comparable to the convective overturning time-scale. Hence, assessing the effect of sub-grid convection based on a fully-developed plume might result in earlier-than-expected conditioning of the troposphere via detrainment.

Tan et al. (2018) proposed a prognostic eddy diffusivity mass flux (EDMF) convection scheme for unified representation of sub-grid turbulence and convection and solved the prognostic equations explicitly to simulate the vertical growth of sub-grid plumes. They considered the general budget equation

$$\frac{\partial\left(\rho_{\mathrm{u}}\sigma_{\mathrm{u}}\psi_{\mathrm{u}}\right)}{\partial t}+\frac{\partial\left(\rho_{\mathrm{u}}w_{\mathrm{u}}\psi_{\mathrm{u}}\right)}{\partial z}+\nabla_h\cdot\left(\rho_{\mathrm{u}}\psi_{\mathrm{u}}\sigma_{\mathrm{u}}\overline{\boldsymbol{u}}_h\right)=S_{\rho_{\mathrm{u}}\psi_{\mathrm{u}}\sigma_{\mathrm{u}}} \tag{3.2.13}$$

where $S_{\rho_{\mathrm{u}}\psi_{\mathrm{u}}\sigma_{\mathrm{u}}}$ represents all the source terms of ψ_{u}, σ_{u} is the fractional area of the updraught, $\overline{\boldsymbol{u}}_{\boldsymbol{h}}$ is the horizontal velocity vector. Decomposing the horizontal model domain into subdomains, they use Equation (3.2.13) to govern five prognostic variables in each subdomain: updraught scalars, updraught vertical velocity, environmental scalars, environmental covariances and the environmetal turbulent kinetic energy (TKE). Specifically, the prognostic equations for scalars ψ and vertical velocity w of updraught and environment (represented by subscripts u and 0 respectively) are as follows:

$$\frac{\partial\left(\rho\sigma_{\mathrm{u}}\psi_{\mathrm{u}}\right)}{\partial t}+\frac{\partial\left(\rho\sigma_{\mathrm{u}}w_{\mathrm{u}}\psi_{\mathrm{u}}\right)}{\partial z}+\nabla_h\cdot\left(\rho\psi_{\mathrm{u}}\sigma_{\mathrm{u}}\overline{\boldsymbol{u}}_h\right)=\rho\sigma_{\mathrm{u}}w_{\mathrm{u}}\left(\epsilon\psi_{u_j}-\delta\psi_{u_i}\right)+\rho\sigma_{\mathrm{u}}S_{\psi} \tag{3.2.14}$$

$$\frac{\partial\left(\rho\sigma_{\mathrm{u}}w_{\mathrm{u}}\right)}{\partial t}+\frac{\partial\left(\rho\sigma_{\mathrm{u}}w_{\mathrm{u}}^2\right)}{\partial z}+\nabla_h\cdot\left(\rho w_{\mathrm{u}}\sigma_{\mathrm{u}}\overline{\boldsymbol{u}}_h\right)= \rho\sigma_{\mathrm{u}}w_{\mathrm{u}}\left(\epsilon w_{u_j}-\delta w_{u_i}\right)+\rho\sigma_{\mathrm{u}}B_{\mathrm{u}}-\rho\sigma_{\mathrm{u}}\frac{\partial\overline{p}}{\partial z} \tag{3.2.15}$$

$$\frac{\partial\left(\rho\sigma_0\psi_0\right)}{\partial t}+\frac{\partial\left(\rho\sigma_0w_0\psi_0\right)}{\partial z}+\nabla_h\cdot\left(\rho\psi_0\sigma_0\overline{\boldsymbol{u}}_h\right)= \rho\sigma_0w_0\left(\epsilon\psi_{0_j}-\delta\psi_{0_i}\right)+\frac{\partial}{\partial z}\left(\rho\sigma_0K\frac{\partial\psi_0}{\partial z}\right)+\rho\sigma_0S_{\psi} \tag{3.2.16}$$

$$\frac{\partial\left(\rho\sigma_0\overline{\psi_0'w_0}\right)}{\partial t}+\frac{\partial\left(\rho\sigma_0w_0\overline{\psi_0'w_0}\right)}{\partial z}+\nabla_h\cdot\left(\rho\sigma_0\overline{\psi_0'w_0}\overline{\boldsymbol{u}}_h\right)= \frac{\partial}{\partial z}\left(\rho\sigma_0K\frac{\partial w_0}{\partial z}\right)+\rho\sigma_0w_0\left(\epsilon_0w_{0_j}-\delta_0w_{0_i}\right)+\rho\sigma_0B_0-\rho\sigma_0\frac{\partial\overline{p}}{\partial z} \tag{3.2.17}$$

where the subscript j represents the quantity from the neighbouring subdomains. Their results, as shown in Figure 3.1, suggest that solving the budget equations for the plume variables is promising towards simulating non-equilibrium convection. However, they only present solutions of their equations in one dimension.

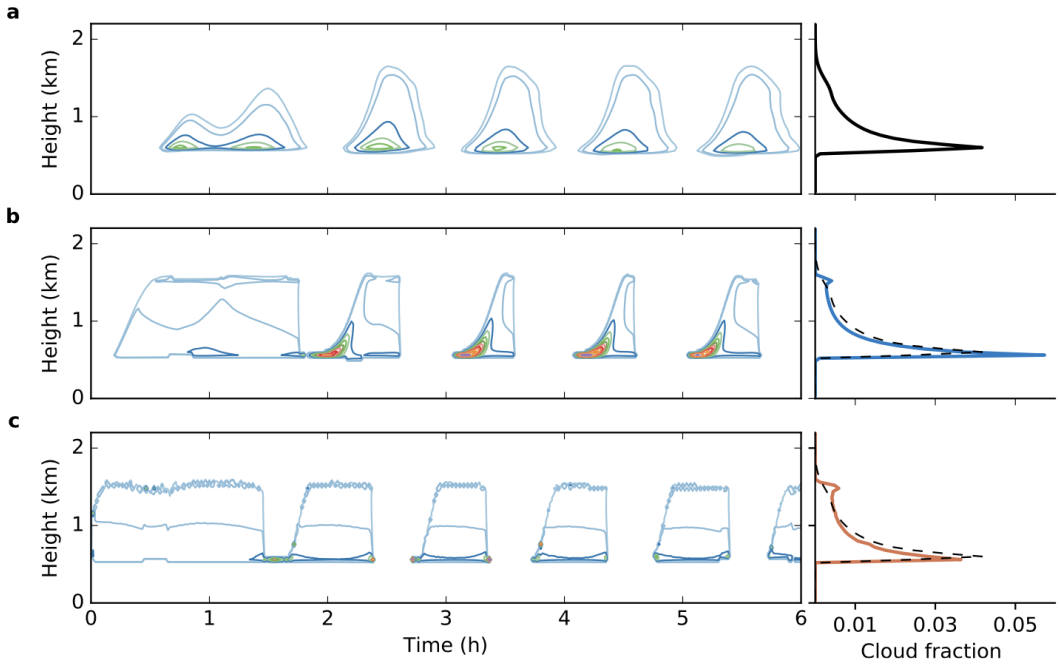

Figure 8. Cloud fraction in life cycle simulations. (a) LES; (b) prognostic EDMF scheme; and (c) diagnostic EDMF scheme. Contours are plotted at 0.005, 0.01, 0.03, and then in intervals of 0.03 up to 0.33. Plots on the right are again 6 h averages.

Figure 3.1: *Comparison of simulated cloud fraction in the BOMEX shallow convection case between LES and parameterised simulations using prognostic EDMF and diagnostic EDMF schemes. From Tan et al. (2018).*

3.2.4 Boundary layer closure

In line with studies (Mapes and Houze, 1992; Neggers et al., 2004; Sobel et al., 2004; Kuang and Bretherton, 2006) showing that correlation between CAPE and cloud-base mass flux is weak, Raymond (1995) proposed the theory of boundary layer quasi-equilibrium (BLQ) as a closure for cloud-base mass flux. In BLQ, the equivalent potential temperature in the mixed layer is regulated at a constant convective threshold value via a balance between the production of conditional instability by surface fluxes and its removal by convective downdraughts. However, BLQ failed to replicate observed large diurnal and synoptic-scale variability of the mixed-layer equivalent potential temperature over land.

Through examining large eddy simulations, Grant and Brown (1999) revealed that the convective cloud-base mass flux is proportional to the boundary layer convective velocity scale w^* (*a.k.a.*

Deardorff velocity, see Deardorff (1970)), given by

$$w_* = \left(\frac{gHh}{\rho C_p \overline{\langle \theta_v \rangle}} \right)^{\frac{1}{3}} \tag{3.2.18}$$

where $\overline{\langle \theta_v \rangle}$ is the vertical average of the ensemble-mean θ_v. This finding shows that boundary layer turbulence is tightly connected with the cloud-base mass flux. Mapes (2000) also emphasised the role of boundary layer turbulence in triggering convection and proposed that the fractional area of sub-grid convective updraught σ_c is quantified by

$$\sigma_c = \exp\left(-k \frac{\text{CIN}}{\text{TKE}} \right) \tag{3.2.19}$$

where TKE is the turbulent kinetic energy and k is a constant. This paved the path for identifying σ_c as the probability of a thermodynamic quantity exceeding a threshold given by a known or assumed probability distribution function.

Fletcher and Bretherton (2010) followed the approach of Mapes (2000) and proposed a CIN closure for the cloud-base mass flux m_{cb} of the form

$$m_{\text{cb}} = c_1 W \exp\left(-c_2 \frac{\text{CIN}}{\text{TKE}} \right) \tag{3.2.20}$$

where c_1 and c_2 are constants which, via analysing results from cloud resolving model simulations, are chosen to be 0.06 and 1 respectively. They also recommended W to take the form

$$W = 0.28\sqrt{\text{TKE}} + 0.64\,\text{m}\,\text{s}^{-1} \tag{3.2.21}$$

i.e. the cloud-base vertical velocity of convection is a function of the strength of turbulence in the boundary layer.

Following methods to model sub-grid moisture variability in cloud parameterisation schemes (e.g. Sommeria and Deardorff, 1977; Chen and Cotton, 1987), Golaz et al. (2002) proposed that the sub-grid variability in buoyancy near the surface can be represented by a joint double Gaussian pdf of vertical velocity w, potential temperature θ and water vapour specific humidity q. The variance and skewness of the distribution is found by parameterising higher-order turbulence moments. Cheinet (2003, 2004) proposed a simpler approach which represents the sub-grid variability with a composite pdf. Their scheme modelled the variability of w in the surface layer with a pdf, in which

the branch of $w < 0$ is a delta function while the branch $w > 0$ is Gaussian-shaped. The same form of pdf is also used to model the variation in θ. The variance in the Gaussian pdf is governed by free convection similarity. They introduced a vertical velocity scale w_s given by

$$w_s = u_* \left(-\frac{z_s}{L} \right)^{1/3} = \left[\kappa g z_s \frac{\left(F_{\theta_v}\right)_S}{\overline{\theta_v}} \right]^{1/3} \tag{3.2.22}$$

where u_* is the friction velocity, L is the Monin-Obukhov length, κ is the von-Karman constant, g is acceleration due to gravity, $\left(F_{\theta_v}\right)_S$ is the surface buoyany flux, $\overline{\theta_v}$ is the mean virtual potential temperature of the surface layer and z_s is any height within the surface layer. Drawing from Wyngaard et al. (1971), they suggested that the standard deviations of θ and w, denoted as σ_θ and σ_w respectively, take the form

$$\begin{aligned} \sigma_w &= C_w w_s \\ \sigma_\theta &= C_\theta \frac{\left(F_{\theta_v}\right)_S}{\overline{\theta_v}} \end{aligned} \tag{3.2.23}$$

where C_w and C_θ have the values of 1.9 and 0.95 respectively. To quantify the updraught mass-flux, the w pdf where $w > 0$ is discretised into 512 intervals, each representing the initial vertical velocity of an updraught w_i which originates from the surface layer. The updraught mass flux (which is not necessarily saturated) is thus the weighed mean of all w_i by fractional area. A steady-state entraining plume model governs the vertical profile of each updraught, with equations for the vertical velocity w_i and a conserved quantity X_i as follows:

$$\begin{aligned} \frac{\partial X_i}{\partial z} &= -\epsilon_i X_i' \\ \frac{\partial {w_i}^2}{\partial z} &= 2a \frac{g}{\overline{\theta_v}} (\theta_v')_i - 2b\epsilon_i {w_i}^2 \end{aligned} \tag{3.2.24}$$

where a and b are dimensionless constants, while ϵ_i is the lateral entrainment rate which is updraught-dependent and is given by

$$\epsilon_i = \max\left(\frac{1}{\tau w_i}, \frac{1}{C_s z} \right) \tag{3.2.25}$$

where τ is the plume turnover time and C_s is set to be 3.

Gentine et al. (2013a,b) developed the probabilistic bulk convective model (PBCM) for dry and shallow convection, the concept of which is similar to that of Cheinet (2003, 2004). They represented the surface variability of θ, w and q with a Gaussian pdf which is centred at the respective

grid-mean values $\overline{\theta}$, $\overline{w}$ and $\overline{q}$. Based on Stull (1988), a similarity relationship was applied to quantify the variances of the pdfs ($\overline{w'^2}$, $\overline{\theta'^2}$ and $\overline{q'^2}$) such that

$$\begin{aligned} \overline{w'^2} &= 0.33{w_*}^2 \\ \overline{\theta'^2} &= 5{\theta_*}^2 \\ \overline{q'^2} &= 5{q_*}^2 \end{aligned} \tag{3.2.26}$$

where w_* is the convective velocity scale as defined in (3.2.18), while θ_* and q_* are defined as

$$\begin{aligned} \theta_* &= \frac{\overline{w'\theta'_v}(0)}{w_*} \\ q_* &= \frac{\overline{w'q'}(0)}{w_*} \end{aligned} \tag{3.2.27}$$

where $\overline{w'\theta'_v}(0)$ and $\overline{w'q'}(0)$ are the surface buoyancy and latent heat fluxes respectively. They classified cloud-forming thermals into three regimes as mentioned in Chapter 1:

1. Forced clouds which do not reach the top of the boundary layer, i.e. thermals with θ'_v that $\theta'_{v,\mathrm{LCL}} < \theta'_v \leq \theta'_{v,h}$, where $\theta'_{v,h}$ is the minimum potential temperature departure from $\overline{\theta_v}$ an updraught must possess to reach the top of the boundary layer at height h.

2. Forced clouds which reach the top of the boundary layer but not the LFC, i.e. thermals with θ'_v satisfying $\theta'_{v,h} < \theta'_v \leq \theta'_{v,\mathrm{LFC}}$, where $\theta'_{v,\mathrm{LFC}}$ is the minimum potential temperature departure from $\overline{\theta_v}$ an updraught must possess to reach its LFC.

3. Active clouds formed by thermals with θ'_v where $\theta'_v > \theta'_{v,\mathrm{LFC}}$.

In this framework, the total fractional area of cloud cover generated from the θ'_v pdf σ_c is

$$\sigma_c = \frac{1}{2}\,\mathrm{erfc}\left(\frac{\theta'_{v,\mathrm{LCL}}}{\sqrt{2}s_{\theta_v}}\right), \tag{3.2.28}$$

the fractional area of updraughts σ_u is

$$\sigma_u = \frac{1}{2}\,\mathrm{erfc}\left(\frac{\theta'_{v,h}}{\sqrt{2}s_{\theta_v}}\right) \tag{3.2.29}$$

and the fractional area of active convective updraughts σ_a is

$$\sigma_a = \frac{1}{2}\,\mathrm{erfc}\left(\frac{\theta'_{v,\mathrm{LFC}}}{\sqrt{2}s_{\theta_v}}\right) \tag{3.2.30}$$

In (3.2.28), (3.2.29) and (3.2.30), s_{θ_v} is the standard deviation of the pdf of θ_v. This is given by $s_{\theta_v} = s_\theta + \overline{\theta}\gamma s_q$, where $s_\theta = \sqrt{\overline{\theta'^2}}$, $s_q = \sqrt{\overline{q'^2}}$ and γ is the ratio of the density of water vapour to that of dry air.

A boundary layer closure makes no scale-specific assumption on the population of deep convective updraughts or their interactions with large-scale processes. In addition, the framework by Gentine et al. (2013a,b) paved the path towards a unified parameterisation of both shallow and surface-driven deep convection. D'Andrea et al. (2014) followed this and introduced ice physics in moist adiabats and precipitation in the updraught formulation. In addition, the lateral entrainment of the updraughts is modified for deep convection, marked by the arrival of precipitation at the surface. A unified parameterisation approach ensures better consistency between the properties of both types of convection.

3.3 Non-local compensating subsidence

Recognising the limitation of the conventional no-net-mass-flux assumption at the 'grey-zone', Grell et al. (2014) spreads the compensating subsidence across a 3×3 grid area based on Grell and Dévényi (2002),. However, the size of spread is arbitrarily chosen and does not vary with resolution of the simulation, lacking physical reasoning as well as scale-awareness.

In non-hydrostatic models, it is possible to allow the model dynamics to resolve the compensating subsidence. Kuell et al. (2007) first implemented this approach in Lokal-Modell (LM) of Deutscher Wetterdienst (Doms and Schättler, 2002; Doms et al., 2007) and found good results. For hydrostatic models, Malardel and Bechtold (2019) introduced a new convection–dynamics coupling to represent compensating subsidence with a modified continuity equation of the dynamical core.

3.4 Chapter summary

In this chapter, solutions to individual aspects of the 'grey-zone' problem of convective parameterisation have been discussed. The stochastic approach by Plant and Craig (2008) produces a scale-aware variability in convective mass fluxes. Schemes with boundary-layer closure have been developed to recognise the role of the convective boundary layer in the diurnal cycle of convection. Prognostic treatment of sub-grid convection by Gerard and Geleyn (2005) and Tan et al. (2018) have improved the representation of non-equilibrium convection in models. Kuell et al. (2007), Grell et al. (2014) and Malardel and Bechtold (2019) relaxed the 'zero net mass flux' assumption

and allowed the effect of compensating subsidence to spread beyond one grid-column. Yet, a convection scheme which unifies the above new solutions is yet to be seen. Thus, designing and evaluating such a scheme is an appropriate research direction for this project.

In the next chapter, a new mass-flux convection scheme, namely Stochastic Prognostic Mass Flux (SPMF), will be described. It features a stochastic trigger function based on scale-aware convective boundary-layer scalings, a prognostic closure and non-local treatment of compensating subsidence. The scheme will then be evaluated in later chapters.

Chapter 4

The Stochastic Prognostic Mass Flux Scheme

4.1 Introduction

A convection scheme for representing the diurnal cycle of convection at 'grey-zone' resolutions simulations should:

- produce scale dependent horizontal variability across a homogeneous resolved-scale flow,
- use a stochastic trigger function,
- incorporate a prognostic boundary-layer based closure to represent non-equilibrium convection, and
- not restrict compensating subsidence from sub-grid convection to one grid column.

The above forms the fundamentals of the Stochastic Prognostic Mass Flux Scheme (SPMF), which is to be described in this chapter. Section 4.2 describes the stochastic trigger function based on the occurrence of thermals within the convective boundary layer. Section 4.3 introduces prognostic equations used to represent the vertical growth of sub-grid convection. Section 4.5 explains how SPMF treats compensating subsidence induced by sub-grid convection. Section 4.4 describes how the forcing on the resolved-scale flow due to sub-grid convection is calculated.

4.2 The stochastic boundary layer trigger function

4.2.1 Stochastic occurrence of boundary layer thermals

SPMF features a trigger function which combines the probabilistic thermal approach of Gentine et al. (2013a,b) and D'Andrea et al. (2014) with the stochastic approach by Plant and Craig (2008). The trigger function assumes that the area of all of the cloud-base thermals present in a grid box at a time-step A_{un} is a first order autoregressive stochastic process. In other words, a fraction of A_{un} is contributed by thermals that persist from previous time-steps A_{un-1}, while the other fraction originates from the new ones triggered at the time-step. Mathematically,

$$A_{un} = \mu A_{un-1} + \sum_{r=1}^{N_n} \Delta A_{ur} \tag{4.2.1}$$

where N_n is the number of CBL thermals which have been initiated in time-step n and ΔA_{ur} is the cloud-base area delivered by each of these. The parameter $\mu \in [0,1)$ controls the decay of the pre-existing cloud-base area. A_{ur} is zero for thermals which are unable to penetrate the CIN layer in order to deliver a non-zero contribution at cloud base. The number of independent boundary layer thermals generated at a time-step is modelled by a Poisson process, while the vertical velocity of each thermal w_T is determined by randomly drawing numbers from a pdf. Both the Poisson process and the pdf of w_T are controlled by convective boundary layer scalings.

4.2.1.1 Scalings of a convective boundary layer

Surface-driven convection is associated with a convective boundary layer (CBL) with height h in which solar heating provides a positive surface buoyancy flux, given by

$$H = \rho c_p \left\langle w' \theta_v' \right\rangle_0 = \rho c_p w_* \theta_* \tag{4.2.2}$$

where $\left\langle w' \theta_v' \right\rangle_0$ the ensemble mean of the covariance of fluctuations of vertical velocity and virtual potential temperature at the surface. The fluctuations of vertical velocity is scaled by w_*, while the parameters h, H and $\overline{\langle \theta_v \rangle}$ in Equation (3.2.18) are assumed to be known. In addition, the condition $H > 0$ must be satisfied to qualify for a CBL, and no sub-grid convection is triggered by a stable boundary layer.

4.2.1.2 The Poisson process

The probability of a random discrete event occurring over a given time and space interval is represented with a Poisson distribution. The only parameter that determines a Poisson distribution is the expected mean of event occurrence E. Therefore, a relationship between the mean number of sub-grid thermals and the properties of the boundary layer must be found. The trigger assumes that only thermals associated with the largest eddies within the boundary layer can contribute to the onset of deep convection. This is in contrast to the real-world situation where a large spectrum of turbulence exists within the boundary layer. While such an assumption neglects the contribution from thermals associated with the rest of the turbulence spectrum, it nonetheless serves as a starting point. A next step might be to use a method similar to Plant and Craig (2008) to produce a size spectrum of boundary layer thermals.

Each occurrence of a boundary layer thermal is considered as an entirely random and independent event with probability p per unit area per unit time. It follows that the probability that a boundary layer thermal develops within a time Δt over an area ΔA, is

$$Pr(n) = \frac{\left(p\Delta A\Delta t\right)^n}{n!} e^{-\left(p\Delta A\Delta t\right)} \tag{4.2.3}$$

where n is the number of thermals. If a single thermal circulation occupies an area A_t over a period of time τ_t, it follows that

$$p = \frac{1}{A_t \tau_t} \tag{4.2.4}$$

which implies that

$$Pr(n) = \frac{\lambda^n}{n!} e^{-\lambda} \tag{4.2.5}$$

with

$$\overline{n} = \lambda \equiv \frac{\Delta A \Delta t}{A_t \tau_t} \tag{4.2.6}$$

τ_t is assumed to be the characteristic eddy turnover time $\tau_* = \left(k_1 h\right) / w_*$ where k_1 is a constant. For A_t, one can employ a simple model of a large eddy which has a symmetric circulation in 3D space, giving

$$A_t = k_2 h^2 \tag{4.2.7}$$

so that $A_t \tau_* = k_3 h^3 / w_*$ with $c_3 = k_1 k_2$. It is reasonable to assume $k_1 \sim 1$ as τ_* and w_* are both characteristic scales of the boundary layer. For k_2, which determines the relative size of the rising

branch (thermal) of the large eddy circulation, one may refer to Lenschow and Stephens (1980), who, via aircraft measurements, suggested that the average length d of thermals in a CBL is

$$\frac{d}{h} = 0.16 \left(\frac{z}{h}\right)^{1/3} \left(1 - \frac{0.25z}{h}\right) \tag{4.2.8}$$

where z is the height. They noted that if all thermals are assumed to be identical circular structures in the horizontal with a random chance of overlapping, the values of d above would then relate to a thermal diameter $D = (4/\pi)d$. It follows that the area of a thermal would be $(\pi/4)D^2$, implying that one could estimate k_2 to be

$$k_2 = \frac{\pi D^2}{4h^2} = (\pi/4)(4/\pi)^2 0.16^2 \left(\frac{z}{h}\right)^{2/3} \left(1 - \frac{0.25z}{h}\right)^2 \tag{4.2.9}$$

For thermals at the top of the boundary layer (*i.e.* $z = h$),

$$k_2(z = h) = (4/\pi)0.16^2 \left(0.75\right)^2 = 0.018 \tag{4.2.10}$$

One should note that $k_2(z)$ within the range $0 < z \leq h$ is a montonically increasing function and so $k_2(z = h)$ is the maximum possible k_2. However, given that this is a fairly weak function of z (*e.g.* $k_2(z = 0.5h) = 0.015$), one does not expect a significant sensitivity of the triggering function to the choice of z.

In a follow-up paper, Lenschow and Stephens (1982) explicitly stated that the fractional area covered by thermals is 0.28 while the environment covers the remaining 0.72 on average. This implies that a thermal on average 28% of its entire parent circulation. Incorporating with the above results gives

$$A_t = \frac{0.018h^2}{0.28} = 0.065h^2 \tag{4.2.11}$$

and thus $k_2 = 0.065$, implying that approximately 15 thermals can co-exist within an area of 1 km^2 if the boundary layer is 1 km deep.

It is worth noting that the thermal studies by Lenschow and Stephens (1980) defines a thermal to have a fluctuation in q which must be at least half the standard deviation. This is inconsistent with the assumption that only the vertical velocity of the thermal is randomised.

4.2.2 The auto-correlation of boundary layer thermals

The auto-regression of boundary layer thermals is assumed to be related to τ_* as it indicates the timescale of overturning of large eddies. Therefore, μ is set to scale with τ_*.

By taking expected values of (4.2.1), one finds

$$E\left(A_{un}\right) = \mu E\left(A_{un-1}\right) + E\left(\phi_n\right) \tag{4.2.12}$$

where $\phi_n = \sum_{r=1}^{N_n} \Delta A_{ur}$. The assumption that each boundary layer thermal is independent implies that

$$E\left(\phi_n\right) = E\left(N_n\right) E\left(\Delta A_{ur}\right) \tag{4.2.13}$$

where $E\left(\Delta A_{ur}\right) \equiv \overline{\Delta A_u}$ includes the thermals which do not produce deep convection. Since $E\left(N_n\right) = \lambda$, it follows that

$$E\left(A_{un}\right) = \mu E\left(A_{un-1}\right) + \lambda\overline{\Delta A_u} \tag{4.2.14}$$

This leads to

$$E\left(A_{un}\right) \equiv \overline{A_u} = \frac{\lambda\overline{\Delta A_u}}{1-\mu} \tag{4.2.15}$$

assuming that $E\left(A_{un}\right) \approx E\left(A_{un-1}\right)$. In other words, the boundary layer is assumed to be in a quasi-equilibrium state. While this is not universally true, it will be shown that the auto-correlation derived from this assumption vanishes if the timescale concerned exceeds τ_*. Thus, this supposition does not lead to $\mu \equiv 1$.

The variance of A_u can be derived as follows:

$$E\left(A_{un}^2\right) = E\left(\mu^2 A_{un-1}^2 + 2\mu A_{un-1}\phi_n + \phi_n^2\right) \tag{4.2.16}$$

It is important to note that the first term on the right is simply $\mu^2 E\left(A_u{}^2\right)$. In addition, since A_u is uncorrelated with the thermals, the second term becomes $2\mu\overline{A_u}\lambda\overline{\Delta A_u}$. The third expands to the sum over all combinations $\Delta A_{ur}\Delta A_{us}$. However, since each thermal is uncorrelated with the others, the expectation is just the sum over N_n expectations of ΔA_{ur}^2, i.e. $\lambda\overline{\Delta A_u{}^2}$. Thus

$$\left(1-\mu^2\right) E\left(A_u{}^2\right) = 2\mu\overline{A_u}\lambda\overline{\Delta A_u} + \lambda\overline{\Delta A_u{}^2} \tag{4.2.17}$$

The autocorrelation function of (4.2.1) is given by:

$$\begin{aligned} E\left(A_{un}A_{un+m}\right) =& \mu E\left(A_{un}A_{un+m-1}\right) + E\left(A_{un}\phi_{n+m}\right) \\ =& \mu E\left(A_{ui}A_{ui+m-1}\right) \end{aligned} \tag{4.2.18}$$

with $E\left(A_{un}\phi_{n+m}\right) = 0$ as there is no correlation between A_{un} and the random event ϕ_{n+m}. Here, one should recognise that (4.2.18) is of the form

$$x_m = \mu x_{m-1} \tag{4.2.19}$$

which has the general form

$$x_m = \mu^{|m|} x_0 \tag{4.2.20}$$

Therefore, (4.2.18) may be written as

$$E\left(A_{un}A_{un+m}\right) = \mu^{|m|} E\left({A_{un}}^2\right) \tag{4.2.21}$$

Thus, the 'integral timescale' for this process is given by

$$\sum_{m=0}^{\infty} \mu^m \Delta t = \frac{1}{1-\mu}\Delta t \tag{4.2.22}$$

It may be helpful for interpretation to relate this result to an exponential correlation timescale. If the autocorrelation function is in the form $E\left(A_{ui}A_{ui+m}\right)/E\left(A_{ui}^2\right) = \exp(-t/\tau_e)$ then one obtains $\exp(-t/\tau_e) = \mu^{t/\Delta t}$ (assuming positive m for the moment, for ease of notation) which implies that $\tau_e = -\Delta t/\ln\mu$. An alternative form for the autocorrelation function is therefore

$$\mu^{|m|} = e^{-\frac{|m|\Delta t}{\tau_e}} \tag{4.2.23}$$

For small $\frac{\Delta t}{\alpha\tau_*}$, $\ln\mu \approx -\frac{\Delta t}{\alpha\tau_*}$ so $\tau_e \approx \alpha\tau_*$.

Clearly, the chosen parameterisation of μ in terms of τ_* provides a cut-off. If $\Delta t \geq \alpha\tau_*$ then the formulation is reverted to the 'uncorrelated' version without any 'memory'. Physically, the interpretation would be that the model time-step is so large that no memory of earlier times is retained, but rather that the behaviour at the current time-step only depends on the conditions at that time-step.

One should also note that since

$$1 - \mu = \frac{\Delta t}{\alpha \tau_*} \tag{4.2.24}$$

it follows that

$$\overline{A_u} = \frac{\lambda \overline{\Delta A_u} \alpha \tau_*}{\Delta t} = \frac{\overline{\Delta A_u} \alpha \Delta A}{A_t} \tag{4.2.25}$$

One can interpret this as saying that the area of boundary layer thermals is given by the product of average cloud-base area associated with a single CBL thermal ($\overline{\Delta A_u}$) and the number of CBL thermals that is expected to be present which is $\alpha \Delta A / A_t$. One can also go a step further in this interpretation by saying that because an average number of thermals λ being generated in area ΔA over time Δt is known, then the average lifetime of those thermals must be $(\alpha \Delta A / A_t) \times (\Delta t / \lambda) = \alpha \tau_*$. On this basis, α is assumed to be 1.

4.2.3 The vertical velocity of boundary layer thermals

4.2.3.1 The distribution of vertical velocity at the top of the boundary layer

To determine the initial vertical velocity of each boundary layer thermal initiated by the Poisson process, the trigger function follows an assumed pdf approach similar to Gentine et al. (2013b,a). It assumes that the vertical velocity at the top of the boundary layer $w(z_{bl})$ follows a Gaussian distribution, as in Gentine et al. (2013b,a) and D'Andrea et al. (2014). The assumption is supported by Kuang and Bretherton (2006) found that near-surface pdf is close to a Gaussian distribution. More sophisticated pdfs for atmospheric conditions at cloud-top have been proposed, such as the multivariate Gaussian pdf by Golaz et al. (2002) and non-Gaussian pdf by Mellado et al. (2010). A simple single-variate Gaussian approach is preferred for a proof-of-concept.

The mean of the distribution is taken as the grid-mean velocity at the top of boundary layer $\overline{w_i(z_{\mathrm{bl}})}$ with a standard deviation $s = \beta w_*$ where β is a constant. Lenschow and Stephens (1980) found that the normalised variance of the vertical velocity distribution of thermals is given by

$$\frac{\overline{w_T'^2}}{w_*^2} = 3.2 \left(\frac{z}{h}\right)^{2/3} \left[1 - 0.75 \left(\frac{z}{h}\right)^{1/2}\right]^2 \tag{4.2.26}$$

For thermals at the top of the boundary layer (*i.e.* $z = h$), it follows that

$$\beta(z = h) = 3.2(0.25)^2 = 0.2 \tag{4.2.27}$$

For every thermal g generated from the Poisson process, its vertical velocity w_g is determined by drawing a random number from the Gaussian distribution. As a boundary layer thermal is, by definition, the rising branch of a boundary layer eddy, only positive values are accepted as the vertical velocity of boundary layer thermals.

A boundary layer thermal contributes to the cloud fractional area if it is capable of reaching the lifting condensation level (LCL) by overcoming any layer of CIN beneath the LCL. This criterion is met if the thermal possess vertical kinetic energy ${w_g}^2/2 > \text{CIN}$, which implies that $w_g > w_c$, where $w_c = \sqrt{2\text{CIN}}$ is the critical vertical velocity (Mapes, 2000). The area of new deep updraught in a time-step can hence be calculated via

$$\sum_{r=1}^{N_n} \Delta A_{ur} = N_d A_t \tag{4.2.28}$$

where N_d is the number of newly triggered deep convective updraughts in a time-step. In SPMF, CIN is calculated via a simple undiluted ascent from the surface.

4.2.4 Heat and moisture of convective updraught at cloud base

Apart from a positive vertical velocity perturbation, real BL thermals are usually associated with higher T and q and thus lead to horizontal temperature and moisture variability at the top of BL (Lenschow and Stephens, 1980, 1982). Therefore, the stochastic trigger function should ideally initiate sub-grid convection with $\psi_\text{u} = \overline{\psi} + \delta\psi$ for $\psi = \theta$, q and q_cl at cloud base where $\delta\psi \neq 0$. In conventional bulk-plume schemes (e.g. Fritsch and Chappell, 1980; Gregory and Rowntree, 1990), the buoyancy of the bulk plume at cloud base is determined by an arbitrary choice of $\delta T > 0$ with $\delta q = \delta q_\text{cl} = 0$. With a positive initial w_u at cloud base given by the trigger function as well as a prognostic equation for w_u, a small initial upward buoyancy is not necessary in the present approach to promote vertical growth of the bulk plume. Thus, as a starting point, $\delta T = \delta q = \delta q_\text{cl}$ is here assumed to be 0 as a simplification.

4.2.5 Updating convective updraught properties at cloud base

When a new sub-grid convective updraught is initiated, the properties of the local bulk plume at cloud base are updated by computing the new weighed mean as follows:

$$\sigma_\text{u}(n+1) = \sigma_\text{u}(n) + \Delta\sigma_\text{u} \tag{4.2.29}$$

$$\psi_{\mathrm{u}}(n+1) = \frac{\psi_{\mathrm{u}}\sigma_{\mathrm{u}}(n) + \Delta\sigma_{\mathrm{u}}\psi_{\mathrm{t}}}{\sigma_{\mathrm{u}}(n+1)} \tag{4.2.30}$$

where $\Delta\sigma_{\mathrm{u}}$ is the increment of σ_{u} from the stochastic trigger function, ψ_{t} is the value of a quantity ψ of the undiluted parcel ascent at cloud base.

4.3 The prognostic plume model

The prognostic plume model in the SPMF scheme is based on Equations (3.2.14) and (3.2.15) proposed by Tan et al. (2018) with the following modifications:

1. Terms involving $\overline{\mathbf{u}}_h$, i.e the horizontal advective tendencies, are assumed to be zero for simplicity.

2. Analogous to the CKE budget idea proposed by Pan and Randall (1998), a dissipation term is introduced to Equation (3.2.14) and is parameterised as

$$\frac{\partial\left(\sigma_{\mathrm{u}}\psi_{\mathrm{u}}\right)}{\partial t} = -\frac{\sigma_{\mathrm{u}}\psi_{\mathrm{u}}}{\tau_c} \tag{4.3.1}$$

   where τ_c is the dissipation time-scale of convective updraughts.

3. Instead of (3.2.15), the updraught vertical velocity w_{u} is governed by the non-steady state form of the plume model proposed by Siebesma et al. (2003); Bretherton and Park (2008) as follows:

$$\frac{\partial w_{\mathrm{u}}}{\partial t} = -\frac{\partial}{\partial z}\left(\frac{1}{2}{w_{\mathrm{u}}}^2\right) + c_1 B_{\mathrm{u}} - c_2 \epsilon {w_{\mathrm{u}}}^2 \tag{4.3.2}$$

   where c_1 and c_2 are constants.

4.4 Calculation of forcing on the resolved-scale flow

From Chapter 3, it has been established that the general form of the eddy mass flux of a quantity ψ' due to sub-grid convection is given by

$$\rho(\overline{w\psi} - \overline{w}\,\overline{\psi}) = \rho\sigma_{\mathrm{u}}(1-\sigma_{\mathrm{u}})(w_{\mathrm{u}} - w_{\mathrm{e}})(\psi_{\mathrm{u}} - \psi_{\mathrm{e}}) \tag{4.4.1}$$

Instead of making conventional assumptions, i.e. $\sigma_u << 1$, $w_u >> w_e$ and $\psi_e \approx \overline{\psi}$, Equation (4.4.1) is directly used to calculate the sub-grid turbulent mass flux due to convection. ψ_e and w_e are calculated via

$$\psi_e = \frac{\overline{\psi} - \sigma_u \psi_u}{1 - \sigma_u} \tag{4.4.2}$$

$$w_e = \frac{\overline{w} - \sigma_u w_u}{1 - \sigma_u} \tag{4.4.3}$$

for $\psi = \theta$, w, q and q_{cl}.

The forcing on a grid-mean quantity due to sub-grid convective updraughts is given by

$$\left.\frac{\partial \overline{\psi}}{\partial t}\right|_{conv} = -\frac{1}{\rho}\frac{\partial}{\partial z}\left(\rho \sigma_u (1 - \sigma_u)(w_u - w_e)(\psi_u - \psi_e)\right) \tag{4.4.4}$$

which is then applied to the model simulation as an additional local source term over one time-step.

4.5 Treatment of compensating subsidence

Following Kuell et al. (2007) and Malardel and Bechtold (2019), SPMF does not directly parameterise compensating subsidence by assuming zero net mass flux. Instead, it relies on the dynamical core of a non-hydrostatic model to adjust the pressure field in response to the additional source term on $\overline{w}$ due to sub-grid convection given by (4.4.4), which in turn modifies the flow field to maintain mass continuity. This approach not only limits SPMF to non-hydrostatic models but could also give rise to two serious problems:

1. The dynamical core could produce inconsistent adjustments to the pressure field and hence net vertical mass fluxes by sub-grid convection, which could lead to instabilities if $\sigma_u \approx 1$, i.e. w_u becomes resolved.

2. The dynamical core continues to solve for $\overline{w}$ which includes w_u in SPMF-activated grid points instead of only solving for w_e. This discrepancy could induce time-step sensitivity and large errors when σ_u is large, which could induce instability in simulations towards the higher-resolution end of the 'grey-zone'.

4.6 Chapter summary

To summarise, SPMF differs from a conventional convection scheme as it

- incorporates a scale-aware stochastic trigger function which models thermals as Poisson events and closes on CIN,
- models the evolution of sub-grid plumes by explicitly solving a similar set of prognostic equations as Tan et al. (2018),
- calculates the forcings from sub-grid updraughts on the resolved-scale flow (including $\overline{w}$) using the unsimplified mass flux equation (Equation (4.4.4)), and
- allows the dynamical core of a non-hydrostatic model to represent the effect of compensating subsidence via continuity.

Some uncertain aspects in SPMF include the parameterisations of the distribution of w_{u} at BL top, size of a BL thermal, entrainment/detrainment and the prognostic equation for w_{u}. The next chapter will explain the implementation of SPMF in the Met-Office NERC Cloud (MONC) model (Brown et al., 2018, 2020), the model to be used in the evaluation of the performance of the convection scheme.

Chapter 5

Implementation of SPMF in MONC

5.1 Introduction

A convection scheme must be made compatible with its host model before implementation. This chapter explains how SPMF scheme is implemented in MONC. Section 5.2 describes the dynamical core and numerical schemes used in MONC. Section 5.3 describes the changes made in MONC to become compatitble with SPMF. Section 5.5 describes the adaptation of SPMF to become compatitble with MONC.

5.2 The Met Office - NERC Cloud Model

MONC is a community large eddy simulation (LES) model initially co-developed by the Met Office in the United Kingdom and the Natural Environment Research Council (NERC) as the highly-scalable successor of the well-regarded Met-Office Large Eddy Model (LEM, Brown et al., 1994). Its capability of performing idealised non-hydrostatic simulations at 'grey-zone' resolutions as well as its simple code structure makes it ideal for convection scheme development projects with limited time allowance.

5.2.1 Dynamical Core

MONC solves the Boussinesq-type equations of motion:

$$\frac{Du_i}{Dt} = -\frac{\partial}{\partial x_i}\left(\frac{p'}{\rho_s}\right) + \delta_{i3}B' + \frac{1}{\rho_s}\frac{\partial \tau_{ij}}{\partial x_j} - 2\epsilon_{ijk}\Omega_j u_k \tag{5.2.1}$$

$$\frac{\partial}{\partial x_i}(\rho_s u_i) = 0 \tag{5.2.2}$$

$$\frac{D\theta'}{Dt} + w\frac{d\theta_s}{dz} = \frac{1}{\rho_s}\frac{\partial h_i^{\theta'}}{\partial x_i} + \frac{1}{\rho_s}\frac{\partial h_3^{\theta'}}{\partial z} + \left(\frac{\partial \theta'}{\partial t}\right)_{\text{mphys}} + \left(\frac{\partial \theta'}{\partial t}\right)_{\text{rad}} \tag{5.2.3}$$

$$\frac{Dq_n}{Dt} = \frac{1}{\rho_s}\frac{\partial h_i^{q_n}}{\partial x_i} - \left(\frac{\partial q_n}{\partial t}\right)_{\text{mphys}} \tag{5.2.4}$$

where

ψ_s denotes the horizontally uniform reference state of a quantity ψ,

ψ' denotes the perturbation from ψ_s,

u is the three-dimensional vector flow velocity,

θ is the potential temperature,

q_n denotes all other scalar variables,

p is the pressure,

ρ is the air density,

B' is the buoyancy,

τ is the sub-grid stress,

h^θ is the sub-grid scalar flux of θ,

h^{q_n} is the sub-grid scalar flux of q_n,

δ_{i3} is the Kroneker delta function,

Ω is the Earth's angular velocity (assuming f-plane),

ϵ_{ijk} is the alternating pseudo-tensor,

$\left(\frac{\partial \psi}{\partial t}\right)_{\text{mphys}}$ denotes the source term due to microphysics, and

$\left(\frac{\partial \psi}{\partial t}\right)_{\text{rad}}$ denotes the source term due to radiation.

MONC supports both Boussinesq (vertically uniform reference states) and anelastic (vertically varying reference states) simulations.

5.2.2 Discretisation

MONC incorporates an Arakawa C-grid in the horizontal and a Lorenz grid in the vertical. Each component of the velocity vector is staggered in respective direction, while scalars quantities are held on the centre point. Viscosities and diffusivities are held on the w-points. The centred time-stepping (leap-frog with the option to apply a Robert-Asselin filter) scheme was used in this project. The model is designed for high-resolution (with grid-length of the order of 100 metres) simulations of an extensive range of turbulent-scale and cloud-scale problems, including boundary layers, shallow and deep convective studies (e.g. Gu et al., 2020).

5.2.3 Advection scheme

The ULTIMATE Total Variation Diminishing (TVD) scheme by Leonard et al. (1993), one of the supported advection schemes in MONC, was chosen. This scheme is linearly conserving and positive definite (i.e. monotonicity preserving) as it introduces limits on fluxes so that initially positive fields remain positive even at sharp gradients such as cloud boundaries. Gray et al. (2001) provide a full description of the implementation of the ULTIMATE scheme in the LEM (which is also applicable to MONC since the two models share the same dynamical core).

5.2.4 Turbulence scheme

The only turbulence scheme (effectively a boundary-layer scheme) available in MONC is the three-dimensional Smagorinsky mixing scheme (Smagorinsky, 1963). The Smagorinsky scheme represents the dissipation of turbulent kinetic energy (TKE) unresolved by LEMs as diffusion resulting from eddy viscosity ν_t, which is modelled as

$$\nu_t = (C_s \Delta x)^2 |S| \tag{5.2.5}$$

where C_s is a constant and S is the rate of strain tensor. Please refer to Smagorinsky (1963), Gray et al. (2001) and Brown et al. (2020) for additional details.

5.2.5 Cloud scheme

The cloud scheme chosen is a simple all-or-nothing condensation scheme, a simpler alternative to the more sophisticated Cloud Aerosol Interacting Microphysics (CASIM) scheme. It is a first-moment microphysics scheme which only approximates the rate of phase change between water vapour to cloud liquid water via the following equations:

$$\begin{aligned} \frac{\partial \overline{q_{\mathrm{cl}}}}{\partial t} &\approx \frac{\max\{-\overline{q_{\mathrm{cl}}}, (\overline{q_{\mathrm{v}}} - \overline{q_{\mathrm{sat}}}) f_{\mathrm{sat}}\}}{\Delta t} \\ \frac{\partial \overline{q_{\mathrm{v}}}}{\partial t} &= -\frac{\partial \overline{q_{\mathrm{cl}}}}{\partial t} \end{aligned} \tag{5.2.6}$$

where $\overline{q_{\mathrm{cl}}}$ is the grid-mean liquid (cloud) water mixing ratio, $\overline{q_{\mathrm{v}}}$ is the grid-mean water vapour mixing ratio and $\overline{q_{\mathrm{sat}}}$ is the grid-mean saturation water vapour mixing ratio. f_{sat} is a correction factor defined as:

$$f_{\mathrm{sat}} = \left(1 + \frac{L}{c_p} \frac{\partial q_{\mathrm{sat}}}{\partial T}\right)^{-1} \tag{5.2.7}$$

where $\frac{\partial q_{\mathrm{sat}}}{\partial T}$ is the rate of change of saturation vapour mixing ratio with temperature calculated using Tetens formula (Tetens, 1930).

The change in grid-mean potential temperature $\overline{\theta}$ associated with the latent heat exchange is thus given by

$$\frac{\partial \overline{\theta}}{\partial t} \approx \frac{L}{c_p \Pi} \frac{\partial \overline{q_{\mathrm{cl}}}}{\partial t} \tag{5.2.8}$$

where Π is the Exner function defined as

$$\Pi = \left(\frac{p}{p_0}\right)^{R/c_p} \tag{5.2.9}$$

where p is the pressure and $p_0 = 1000$ hPa is the reference pressure.

The all-or-nothing approach is valid for 100-metre scale resolutions (which MONC is originally designed for), but not for simulations at kilometre-scale resolutions where convective updraughts and clouds are only partially resolved. However, partial cloud schemes (e.g. Kuwano-Yoshida et al., 2010; Kim and Hong, 2018) are not available in MONC at the time of writing. Thus, one should be aware that the simulated cloud cover might be less than expected as partial clouds were

not parameterised at unsaturated grid points in the absence of sub-grid convection. This applies to 'grey-zone' simulations in which SPMF was enabled. However, this slight loss of realism does not invalidate the evaluation of SPMF, which is based on comparing the results with the scheme enabled to the reference control truth.

5.3 Modifying MONC for SPMF

5.3.1 Modification to the adaptive time-stepping algorithm

To accommodate the implementation of the prognostic equations for convective plumes as well as the use of the Smagorinsky scheme at 'grey-zone' grid-lengths, it was necessary to modify the adaptive time-stepping in MONC. The model calculates the largest viscous stability parameter c_{vis} via

$$c_{\text{vis}} = \max_{\text{flowdomain}} \left[4\Delta t \nu_{\mathbf{max}} \left(\frac{1}{\Delta x^2} + \frac{1}{\Delta y^2} + \frac{1}{\Delta z^2} \right) \right] \tag{5.3.1}$$

where Δt is the time-step and ν_{max} is the larger between the horizontal viscosity ν_h and vertical viscosity ν. Similarly, the largest advective Courant number CVEL is calculated as

$$c_{\text{vel}} = \Delta t \left(\left(\frac{|u|}{\Delta x} \right)_{\text{max}} + \left(\frac{|v|}{\Delta y} \right)_{\text{max}} + \left(\frac{|w|}{\Delta z} \right)_{\text{max}} \right) \tag{5.3.2}$$

The CFL number is then calculated as

$$\text{CFL} = \frac{c_{\text{vis}}}{c_{\text{vis}_{\text{max}}}} + \frac{c_{\text{vel}}}{c_{\text{vel}_{\text{max}}}} \tag{5.3.3}$$

where $c_{\text{vis}_{\text{max}}}$ and $c_{\text{vel}_{\text{max}}}$ are the user-configurable maximum values for c_{vis} and c_{vel}. The model time-step is then chosen such that CFL = 1.

To maintain numerical stability when calculating the advective tendencies in the prognostic equations for updraught quantities, the calculation of CVEL is modified such that

$$c_{\text{vel}} = \delta t \left(\left(\frac{|u|}{\Delta x} \right)_{\text{max}} + \left(\frac{|v|}{\Delta y} \right)_{\text{max}} + \left(\frac{max(|\overline{w}|, |w_{\text{u}}|}{\Delta z} \right)_{\text{max}} \right) \tag{5.3.4}$$

According to Equation (5.2.5), ν_t becomes excessively large (as preliminary experiments indicated) as $\Delta x > 1$ km, leading to unrealistically efficient removal of horizontal gradients as well as the use

of very short time-steps. To alleviate this problem, a maximum allowed viscosity was implemented in the Smagorinsky scheme such that

$$\nu = \min(\nu_t, \nu_{\max}) \tag{5.3.5}$$

where

$$\nu_{\max} = \frac{c_{\mathrm{vis}_{\max}}}{4\Delta t_{\min}\left(\frac{1}{\Delta z}\right)^2} \tag{5.3.6}$$

where $\Delta t_{\min}$ is the user-configurable minimum time-step, which was set to 0.5 s for this project.

5.4 Additional prognostics and diagnostics

To predict the evolution of the sub-grid updraughts using the above equations, the following prognostics are added to the model:

- Fractional mass (density) of the sub-grid updraughts $\sigma_{\mathrm{u}}\rho_{\mathrm{u}}$
- Fractional density-weighted potential temperature of the sub-grid updraughts $\sigma_{\mathrm{u}}\rho_{\mathrm{u}}\theta_{\mathrm{u}}$
- Fractional water vapour of the sub-grid updraughts $\sigma_{\mathrm{u}}\rho_{\mathrm{u}}q_{\mathrm{u}}$
- Fractional cloud liquid water of the sub-grid updraughts $\sigma_{\mathrm{u}}\rho_{\mathrm{u}}q_{\mathrm{cl_u}}$
- The vertical velocity of the sub-grid updraughts w_{u}

θ_{u}, q_{u}, and $q_{\mathrm{cl_u}}$ are diagnosed directly from the prognostics. The updraught virtual temperature $T_{\mathrm{v_u}}$ is calculated from

$$T_{\mathrm{v_u}} = \theta_{\mathrm{u}}(1 + 0.61q_{\mathrm{u}})\left(\frac{p}{p_{\mathrm{ref}}}\right)^{R_d/c_p} \tag{5.4.1}$$

where p_{ref} is reference surface pressure and R_d is the specific gas constant for dry air. ρ_{u} is calculated using the ideal gas law:

$$\rho_{\mathrm{u}} = \frac{p}{R_d T_{\mathrm{v_u}}} \tag{5.4.2}$$

and then σ_{u} is

$$\sigma_{\mathrm{u}} = \frac{\sigma_{\mathrm{u}}\rho_{\mathrm{u}}}{\rho_{\mathrm{u}}} \tag{5.4.3}$$

The calculation of ρ_{u} and hence σ_{u} uses the assumption that the pressure is the same inside and outside the plumes.

5.5 Modifying SPMF for MONC

5.5.1 Discretisation of the prognostic equations

Prognostic equations in SPMF were modified to adapt to the centred-in-time temporal integration and the Arakawa C-grid in MONC. In time, the prognostic equations were numerically solved using

$$\Psi_{u_{n+1}} = \Psi_{u_{n-1}} + 2\Delta t \left(\frac{\Delta \Psi_u}{\Delta t}\right)_n \tag{5.5.1}$$

where Ψ_u is the convective prognostic in question, Δt is the model time-step, $\left(\frac{\Delta \Psi_u}{\Delta t}\right)_n$ is the cumulative tendency from all source terms and n is the current time-step.

The convective prognostics were discretised in space according to the C-grid and ULTIMATE for advection. The scalar convective prognostics were solved at the pressure levels while the updraught vertical velocity w_u was solved at the w-levels (labelled as 1/2 levels).

5.5.2 Density of updraught

The anelastic approximation implies that there is no horizontal density variation and thus density is a function of height defined by a reference profile $\rho_r(z)$ which is constant in time. This implies that the prognostic equation set for sub-grid updraught scalar quantities may be simplified to:

$$\frac{\partial \sigma_u}{\partial t} = -\frac{1}{\rho_r} w_u \frac{\partial(\sigma_u \rho_r)}{\partial z} + \sigma_u w_u (\epsilon - \delta) + \left.\frac{\partial \sigma_u}{\partial t}\right|_{trig} + \left.\frac{\partial \sigma_u}{\partial t}\right|_{mphys} - \frac{\sigma_u}{\tau_c} \tag{5.5.2}$$

$$\frac{\partial\left(\sigma_u \psi_u\right)}{\partial t} = -\frac{1}{\rho_r} w_u \frac{\partial(\sigma_u \rho_r \psi_u)}{\partial z} + \sigma_u w_u (\epsilon \psi_e - \delta \psi_u) + \left.\frac{\partial(\sigma_u \psi_u)}{\partial t}\right|_{trig} + \left.\frac{\partial(\sigma_u \psi_u)}{\partial t}\right|_{mphys} - \frac{\sigma_u \psi_u}{\tau_c} \tag{5.5.3}$$

for $\psi = \theta$, q and q_{cl}.

5.5.3 Potential temperature

MONC can solve the anelastic Navier-Stokes equations based on perturbations to a reference profile. Therefore, instead of the absolute potential temperature, MONC calculates the buoyancy

and advection of heat based on the perturbation potential temperature θ', which is defined as

$$\theta'(t,\mathbf{x}) = \theta(t,\mathbf{x}) - \theta_{\mathrm{r}}(t,z) \tag{5.5.4}$$

where θ is the absolute potential temperature, θ_{r} is the reference profile potential temperature and $\mathbf{x}$ is the three-dimensional space vector. For consistency, the updraught potential temperature in the convection scheme is represented by the perturbation updraught potential temperature θ'_u, which is defined as

$$\theta'_u(t,\mathbf{x}) = \theta_u(t,\mathbf{x}) - \theta_{\mathrm{r}}(t,z) \tag{5.5.5}$$

The potential temperature anomalies of the sub-grid updraught are represented by the prognostic variable $\sigma_{\mathrm{u}}\theta'_u$, the governing equation for which is obtained by substituting ψ_{u} with $\theta'_{\mathrm{u}} + \theta_{\mathrm{r}}$ in Equation (5.5.3).

5.5.4 *Minimum threshold for σ_{u}*

The convection scheme must identify whether sub-grid convection is present in a grid point. Ideally, this translates to the condition $\sigma_u > 0$. However, despite efforts made to ensure the highest floating point precision, it is inevitable that extremely small numbers are produced to represent the value of 0 in numerical modelling. This is likely to lead to problems in numerical simulations of the atmosphere when conditional statements are used to determine whether convective activity is present in a particular grid point. In addition, numerical diffusion induced by the advection scheme may also lead to unrealistically small values. Therefore, it is necessary to introduce a minimum $\sigma_{\mathrm{u_{min}}}$ to ensure that the presence of sub-grid convection at a grid point is realistically identified. In this study, $\sigma_{\mathrm{u_{min}}}$ was set to 10^{-5} for all 'grey-zone' simulations with SPMF enabled.

5.5.5 *Parameterisation of entrainment and detrainment rates in the plume model*

For this project, ϵ and δ are parameterised based on Simpson and Wiggert (1969) and Simpson (1971) as

$$\epsilon = \delta = \frac{0.2}{r_{\mathrm{u}}} \tag{5.5.6}$$

where $r_{\mathrm{u}} = \sqrt{\Delta x \Delta y \sigma_u / \pi}$ is the radius of the sub-grid bulk plume.

5.6 Chapter summary

The above modifications allow SPMF to be implemented in MONC. However, pressure tendencies due to sub-grid convection have been neglected as it requires modifications to MONC so extensive that would effectively become a separate model and is thus beyond the scope of this project. This introduces an inconsistency in treatment of net mass transport by convection as the pressure equation in the dynamical core was not modified accordingly. This limitation could have negative effects on the behaviour of SPMF-enabled simulations, which is evident in the evaluation of the scheme documented in the next two chapters.

Chapter 6

Performance of SPMF scheme in simulating the diurnal cycle of convection

6.1 Introduction

This chapter presents results of the SPMF scheme in simulating the diurnal cycle of convection using the modified version of MONC. Section 6.2 describes the Large-scale Biosphere and Atmosphere (LBA) case, the chosen test case for the evaluation, including its specification and reference results. Section 6.3 compares the MONC simulations of the LBA case at 'grey-zone' resolutions between without and with the SPMF scheme. Section 6.4 describes the characteristics of sub-grid convective updraughts in the SPMF-enabled simulations.

6.2 The LBA case

6.2.1 A brief introduction

The LBA case (Grabowski et al., 2006) was developed following a field campaign conducted over Amazonia. With ground-based and satellite (Tropical Rainfall Measuring Mission, TRMM) instruments, observations were taken over a diurnal onset of convection, including the transition from shallow to deep convection, over the Amazon rainforest on 23^{rd} February 1999. The primary purpose of the field campaign was to compare model results from different cloud-resolving models

and single column models (SCMs) and establish a set of benchmark results for this case of diurnal cycle of convection over land. There is little interference from other large-scale processes so that the daytime development of convection is purely driven by the diurnal cycle of surface heat fluxes.

The daytime convective development over the observed area features the development of a well-mixed convective boundary layer from the early morning, followed by the initiation of shallow convection as the boundary layer grows in height. Transition from shallow to deep convection occurs near local noon, followed by the upscale growth of convection into mesoscale systems in the afternoon. The study of the LBA case by Grabowski et al. (2006) focuses on the onset and development of convection before upscale growth, i.e. between sunrise (07:30 LST) and early afternoon (13:30 LST).

6.2.2 Specification

In the LBA case, there are two sources of external forcings: prescribed surface fluxes and radiative cooling. The surface sensible heat flux $H(t)$ and latent heat flux (λE) in W m^{-2} are prescribed as:

$$\begin{aligned} H(t) &= 270 f(t)^{1.5} \\ \lambda E(t) &= 554 f(t)^{1.3} \end{aligned} \tag{6.2.1}$$

where

$$f(t) = \max\left\{0, \cos\left(\frac{\pi}{2}\frac{5.25 - t}{5.25}\right)\right\} \tag{6.2.2}$$

and t is the model time in hours.

The initial condition consists of a horizontally homogeneous field with a vertical profile which matches the sounding obtained at 0730 LST on 23 February 1999 (documented in Appendix 8.3.9. During simulation, the mean horizontal wind (i.e. u and v) relaxes to the initial profile with a time-scale of 1 hour. The lateral boundary conditions are bi-periodic. To excite instabilities across the domain, small-scale random perturbations are imposed at the initialisation and throughout the simulation. This included introducing random perturbations to both surface sensible and latent fluxes with a 10% amplitude every time step). At initialisation, random perturbations were introduced to the potential temperature and water vapour mixing ratio fields, with amplitudes of 0.1 K and 0.1 g kg^{-1}, applied in the lowest 1 km of the model domain. It should be noted that the random perturbation method described above slightly deviates from that specified in Grabowski et al. (2006), in which the temperature and moisture fields are perturbed every 15 minutes of model

time.

6.2.3 Case characteristics

A reference set of results was produced by a MONC simulation of the LBA case at 100-metre resolution over a 32 km $\times$ 32 km domain with 101 quadratically spaced vertical levels up to 30 km. This was compared to the 3D simulations performed by Grabowski et al. (2006) (referred to as the benchmark simulations hereafter) to evaluate the validity of the reference simulation.

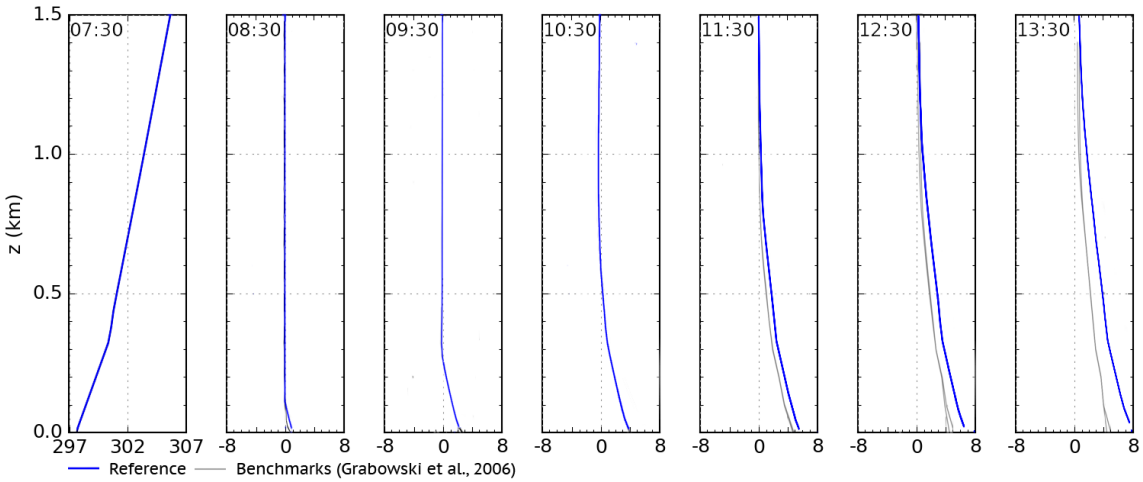

Figure 6.1: *Evolutions of domain average potential temperature (in K) within the lowest 1.5 km in the LBA benchmark simulations and reference run. The first profile from the left is the initial profile of potential temperature, while the remaining profiles are plotted as the deviation from the initial profile. The simple cloud scheme was used to represent cloud formation and dissipation.*

Figure 6.1 shows the domain mean evolution of the boundary layer temperature of the LBA case. Increasing sensible heat flux causes the well-mixed layer to gradually reach a depth of 1200 m by the end of the simulation. Detrainment and evaporation of shallow clouds causes air above the boundary layer to slightly cool down between the second and fourth hour of the simulations. Since rain is not represented, the boundary layer in the reference simulation becomes warmer than that in the benchmark simulations beyond the fourth hour when convective downdraughts cool the boundary layer in the latter.

Figure 6.2 shows the tephigrams of the LBA reference simulation at whole hours after initialisation.The absence of initial CIN leads to the complete erosion of the capping inversion by the second hour of simulations as the convective boundary layer deepens.

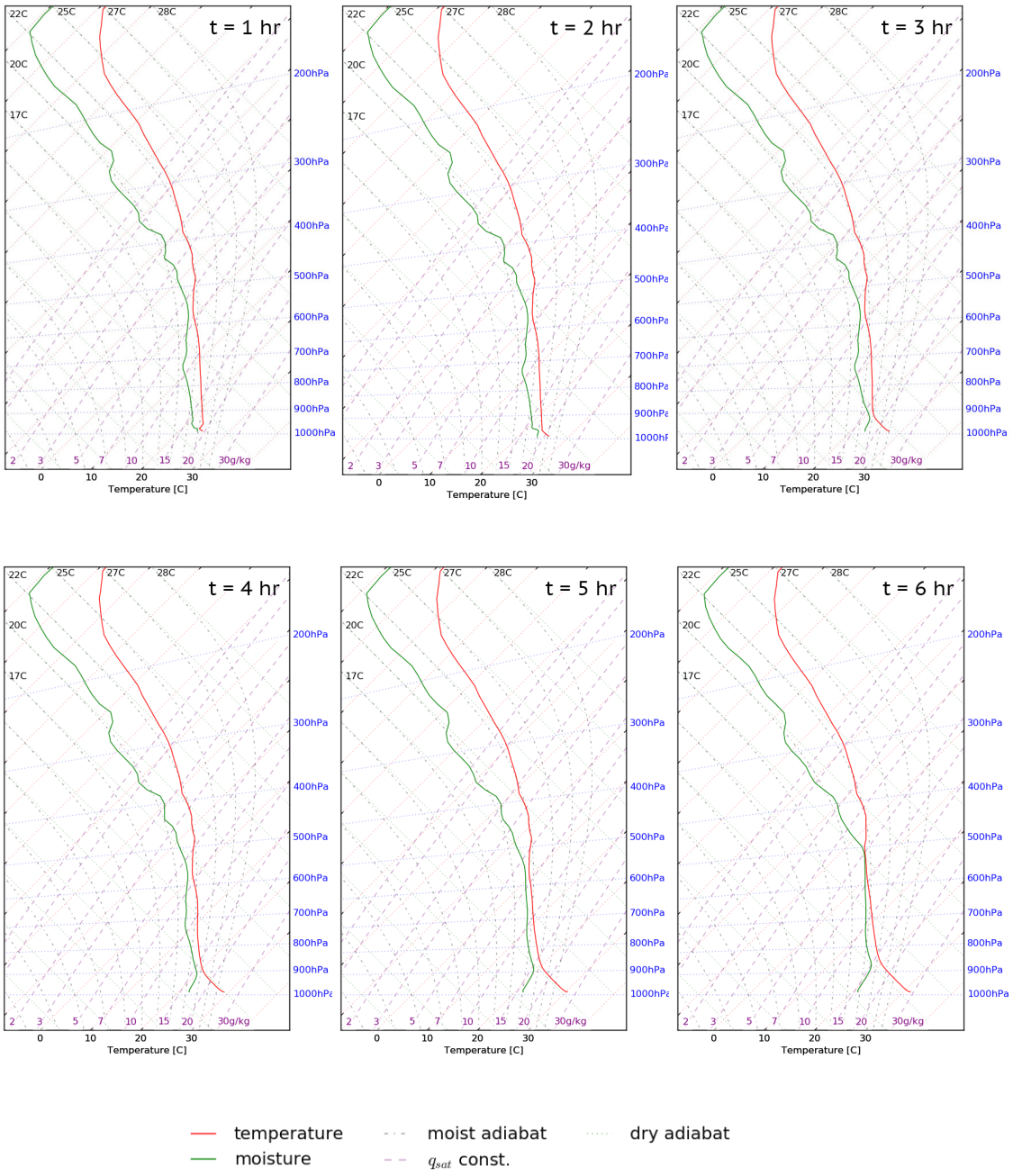

Figure 6.2: *Soundings at whole hours after initiation of the LBA reference simulation.*

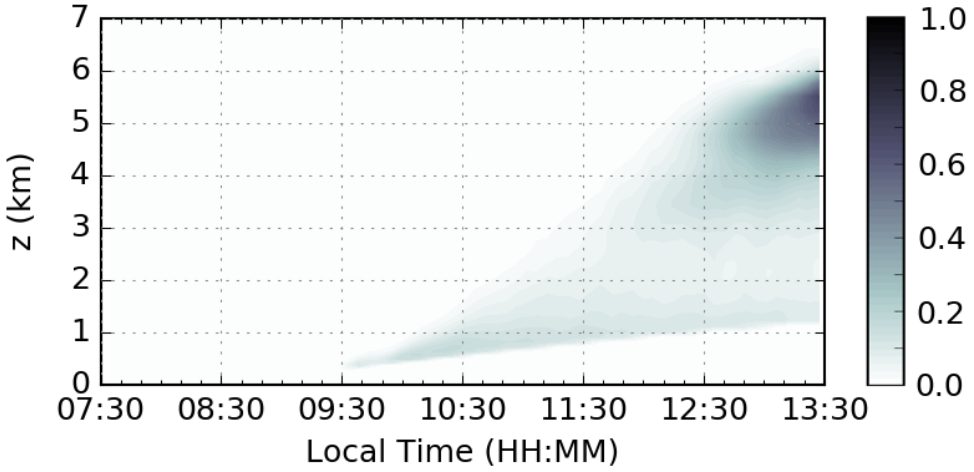

Figure 6.3: *Evolution of cloud fraction in the LBA reference simulation. The horizontal cloud fraction at a given model level is defined as the fraction of grid points across the horizontal domain at which the cloud condensate (the total of cloud water and cloud ice) mixing ratio* $Q \geq \min(10^{-5}, 0.01 q_{\text{sat}})$ *kg / kg*$^{-1}$.

Figure 6.3 shows the development of domain cloud coverage at different heights throughout the simulation. Shallow cumuli initiate at approximately $t = 2$ hr and gradually transition into deeper clouds (cloud top reaching 6.5 km) with increasingly higher base. Unlike the benchmark simulations, cloud liquid accumulates at cloud top since rain is not parameterised. The consequent absence of convective downdraughts, as indicated by Figure 6.6, leads to reduced low-level convergence associated with cold pools after $t = 4$ hr. In conjunction with the lack of latent heat release from freezing, this could explain the lower cloud top heights and centre of mass in the reference simulation as shown in Figures 6.4 and 6.5.

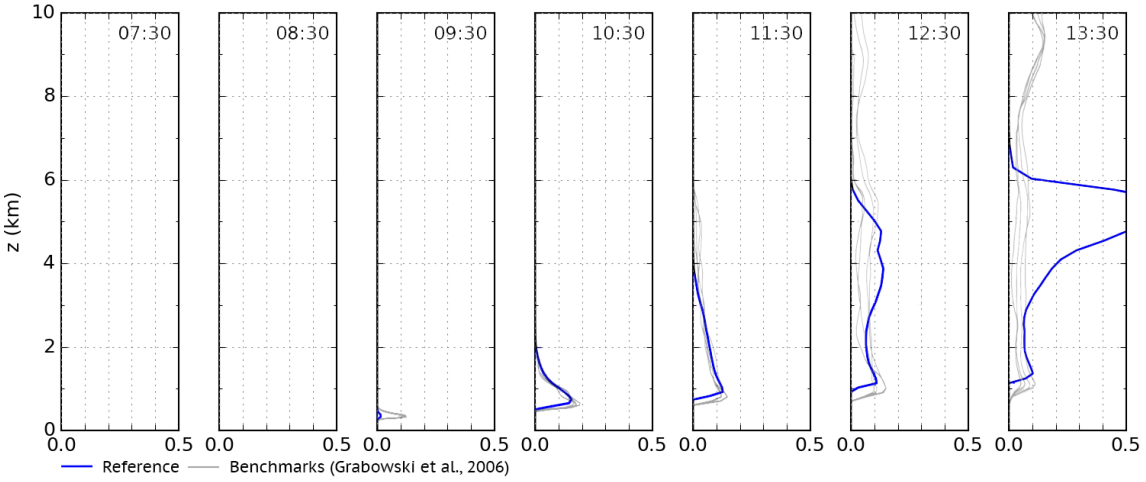

Figure 6.4: *Vertical profiles of horizontal cloud fraction (as defined in Figure 6.3) at whole hours after initialisation in the LBA reference and benchmark simulations.*

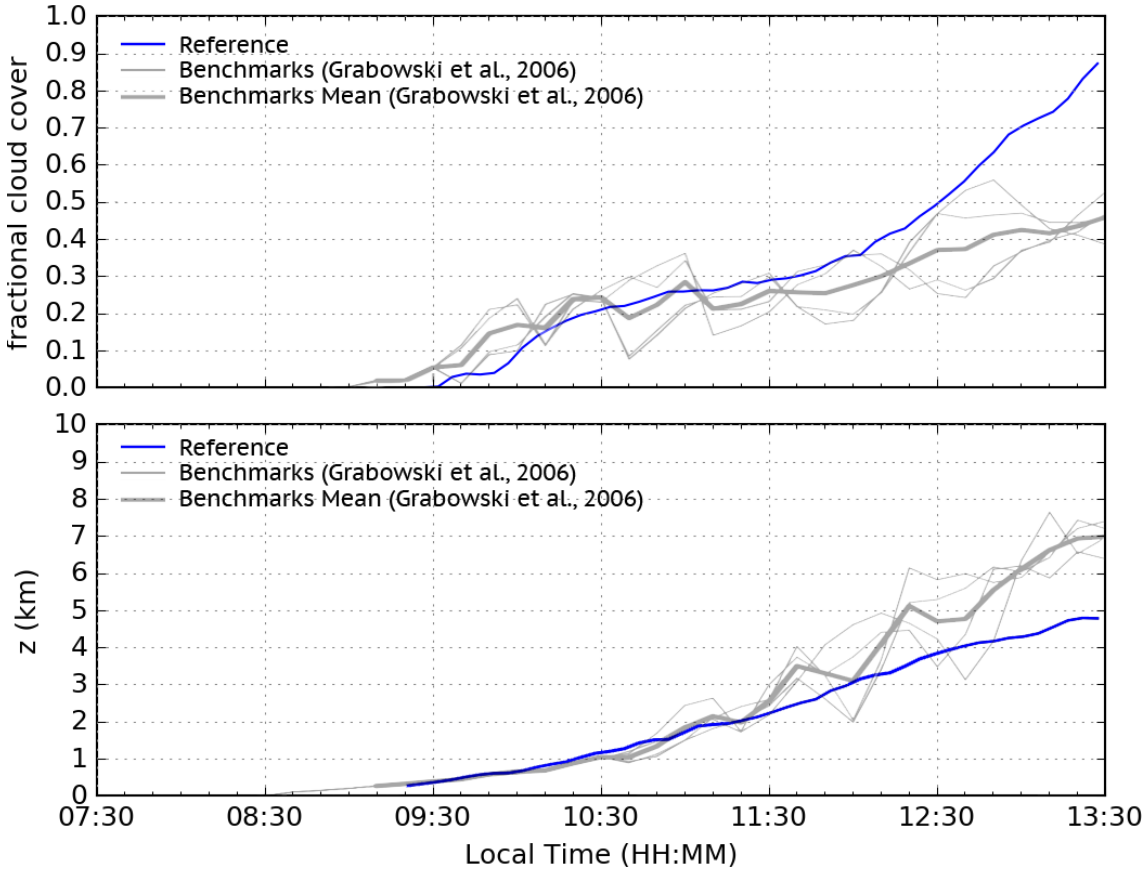

Figure 6.5: *Evolution of total cloud cover (top) and height of centre of mass of clouds (bottom) in the LBA reference and benchmark simulations. Total cloud cover is defined as the fraction of grid columns in which the vertically integrated $Q \geq 0.01$ kg m^{-2}. The height of the centre of mass of clouds is given by $\int zQ\,dV / \int Q\,dV$, where V is the volume represented by a grid point.*

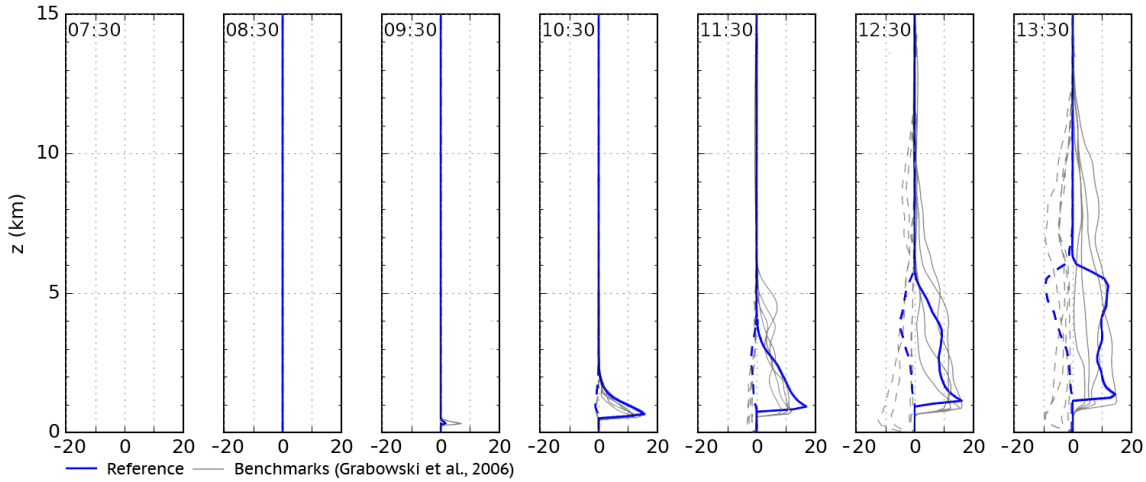

Figure 6.6: *Vertical profiles of domain-mean updraught (solid lines) and downdraught (dashed lines) mass fluxes (in 0.01 kg m^{-2} s^{-2}) at whole hours in the reference and benchmark simulations. Local cloud updraught and downdraught mass fluxes are defined as $\delta\rho\max(0,w)$ and $\delta\rho\min(0,w)$ respectively, where ρ is the density of air and w is the vertical velocity. $\delta = 1$ if $Q \geq min(10^{-5}, 0.01q_{sat})$ kg kg^{-1} or 0 otherwise where q_{sat} is the saturation mixing ratio. Times are local time of the LBA case.*

6.3 Performance of the SPMF scheme in 'grey-zone' LBA simulations

6.3.1 Assessement strategy

Simulation	Δx (km)	$L_x \times L_y$	Domain size
S1P0K, S1P0KCP	1.0	96 km × 96 km	96 × 96
S2P0K, S2P0KCP	2.0	96 km × 96 km	48 × 48
S3P0K, S3P0KCP	3.0	96 km × 96 km	32 × 32
S4P0K, S4P0KCP	4.0	96 km × 96 km	24 × 24
S5P0K, S5P0KCP	5.0	100 km × 100 km	20 × 20
S6P0K, S6P0KCP	6.0	96 km × 96 km	16 × 16

Table 6.1: *The 'grey-zone' simulations of the LBA case for evaluation of the SPMF scheme. All other settings are identical to those in the reference simulation.*

MONC was run with and without the SPMF scheme at various 'grey-zone' resolutions (see Table 6.1 for details).

6.3.2 Clouds

Figure 6.7 shows the evolution of domain cloud fraction in 'grey-zone' simulations without SPMF. Regardless of the resolution, a stratocumulus layer (suggested by cloud fraction 1.0 and lack of upward mass fluxes as indicated in Figure 6.8) develops at approximately 2.5 hours after initialisation. This is consistent with the findings by Petch (2006), who concluded that the formation of the stratocumulus layer is controlled by the boundary layer scheme. At $\Delta x \sim 1$ km, the Smagarinsky scheme behaves as a Reynolds-averaged boundary layer scheme with very large horizontal diffusivity. This leads to the formation of a horizontally homogeneous well-mixed layer capped by a layer of stratocumulus. The higher the resolution, the later and more rapid the onset of deep convection (characterised by increase in cloud vertical extent and convective updraught mass fluxes) is in the simulation, which is consistent with conventional findings (e.g. Lean et al., 2008). The above suggests that MONC produces scale dependent 'grey-zone' LBA simulations without SPMF.

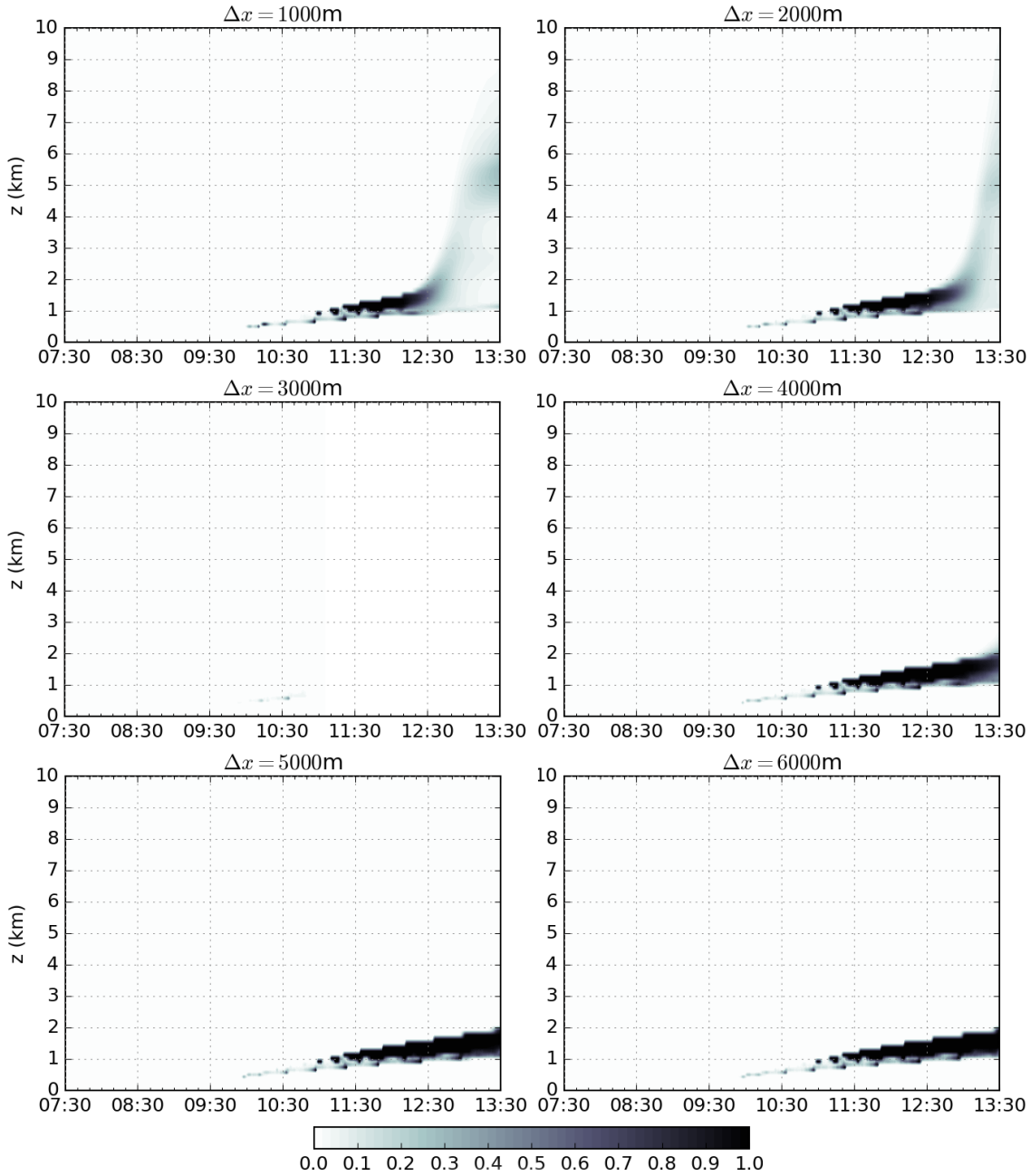

Figure 6.7: *Evolution of cloud fraction (as defined in Figure 6.3) in simulations of the LBA case at different 'grey-zone' resolutions without the convection scheme. No data is shown for the simulation at $\Delta x = 3$ km beyond 11:30 LST as the model has crashed.*

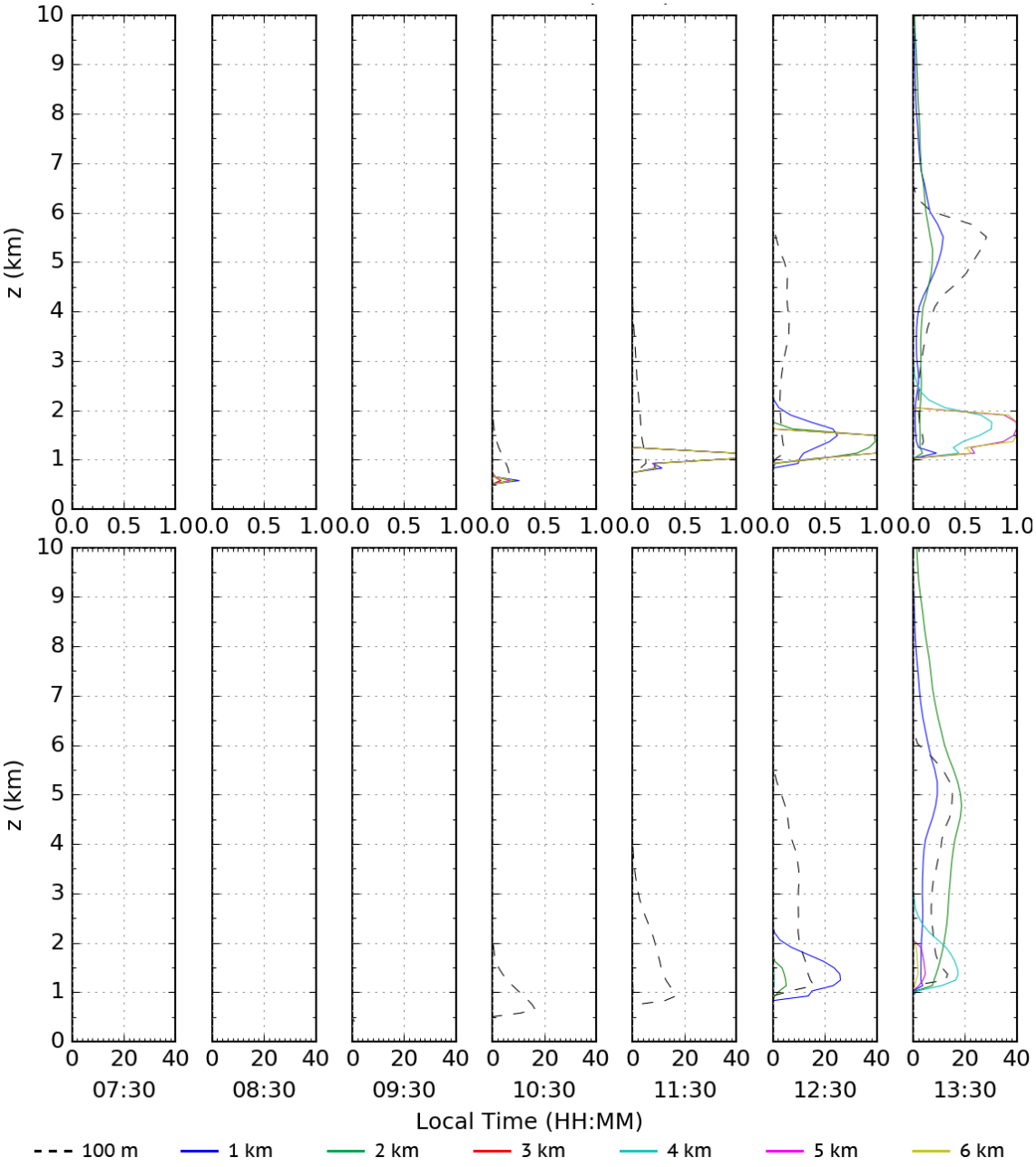

Figure 6.8: *Evolutions of vertical cloud fraction (top) and updraught mass-flux (bottom) profiles of all six 'grey-zone' simulations of the LBA case without the convection scheme at different model times. No data is shown for the simulation at $\Delta x = 3$ km beyond 11:30 LST as the model has crashed.*

Figure 6.9 shows the evolutions of domain-mean vertically integrated liquid water path (LWP) in the reference and the six 'grey-zone' simulations without SPMF enabled. The lack of convective clouds in all 'grey-zone' simulations contributes to the lower vertically integrated LWP when compared with the reference. Between the fifth and sixth hour, explicit convection initiates in the 1-km and 2-km simulations and leads to a sharp increase in LWP. It is clear that the simulation of convective clouds is highly scale-dependent among the 'grey-zone' simulations without a convection scheme.

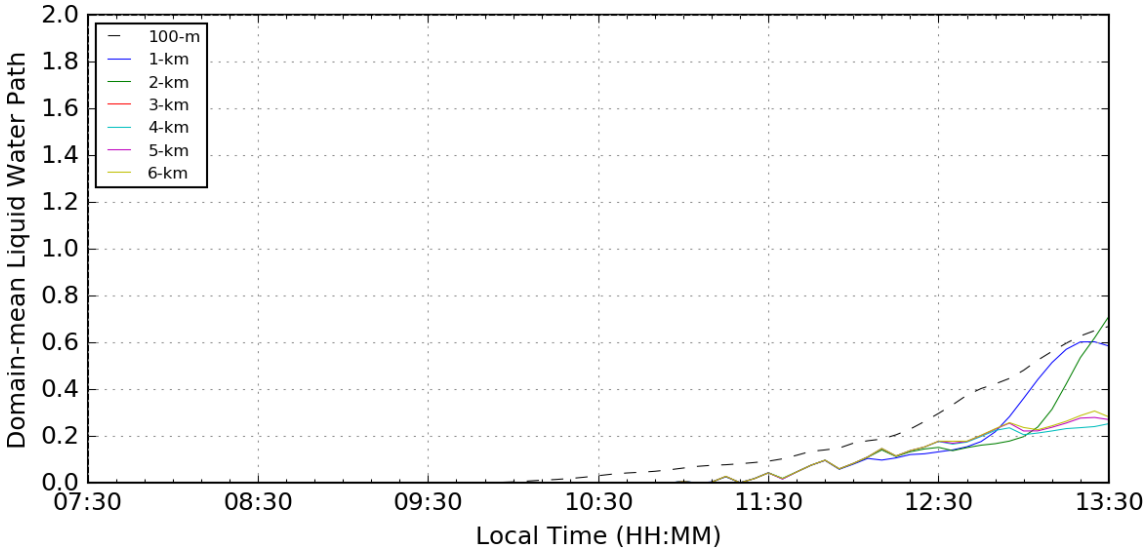

Figure 6.9: *Evolution of domain mean vertically integrated LWP of all six 'grey-zone' simulations without a convection scheme and the reference simulation of the LBA case at different model times. The vertically integrated LWP is defined as* $\text{LWP} = \int_0^z \rho q_l \, dz$ *where* q_l *is the liquid water mixing ratio.*

With SPMF enabled however, the discrepancy in convective cloud development among the simulations are reduced. First clouds appear at approximately 3 hours after initiation regardless of model resolution as shown in Figure 6.10. Cloud coverage at the top of the boundary layer and the rate of vertical growth are also in better agreement, although the reduction of cloud top height with increasing resolution implies some scale-dependence remains. Figure 6.11 reveals a more consistent evolution of updraught mass flux profiles across the simulations. These suggest that the SPMF scheme could reduce scale-dependence across simulations of convection at different 'grey-zone' resolutions.

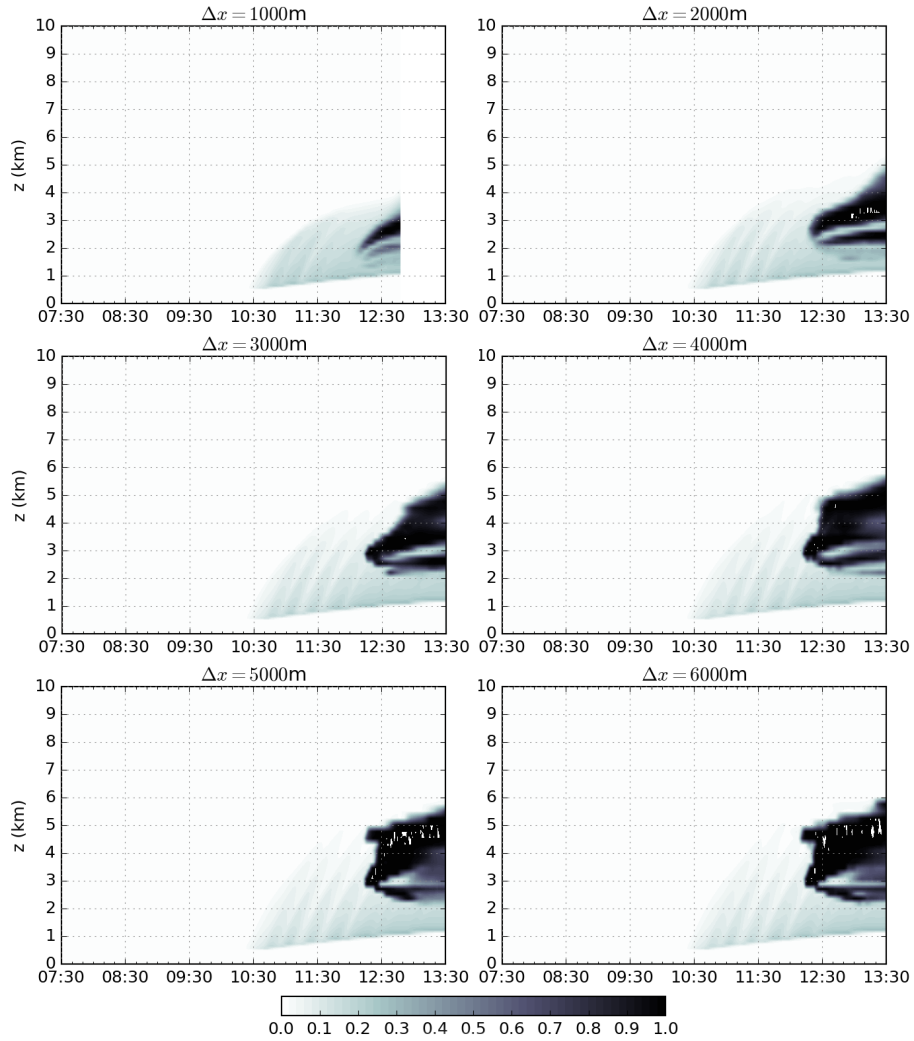

Figure 6.10: *Evolution of cloud fraction (as defined in Figure 6.3) in SPMF-enabled simulations of the LBA case at different 'grey-zone' resolutions.*

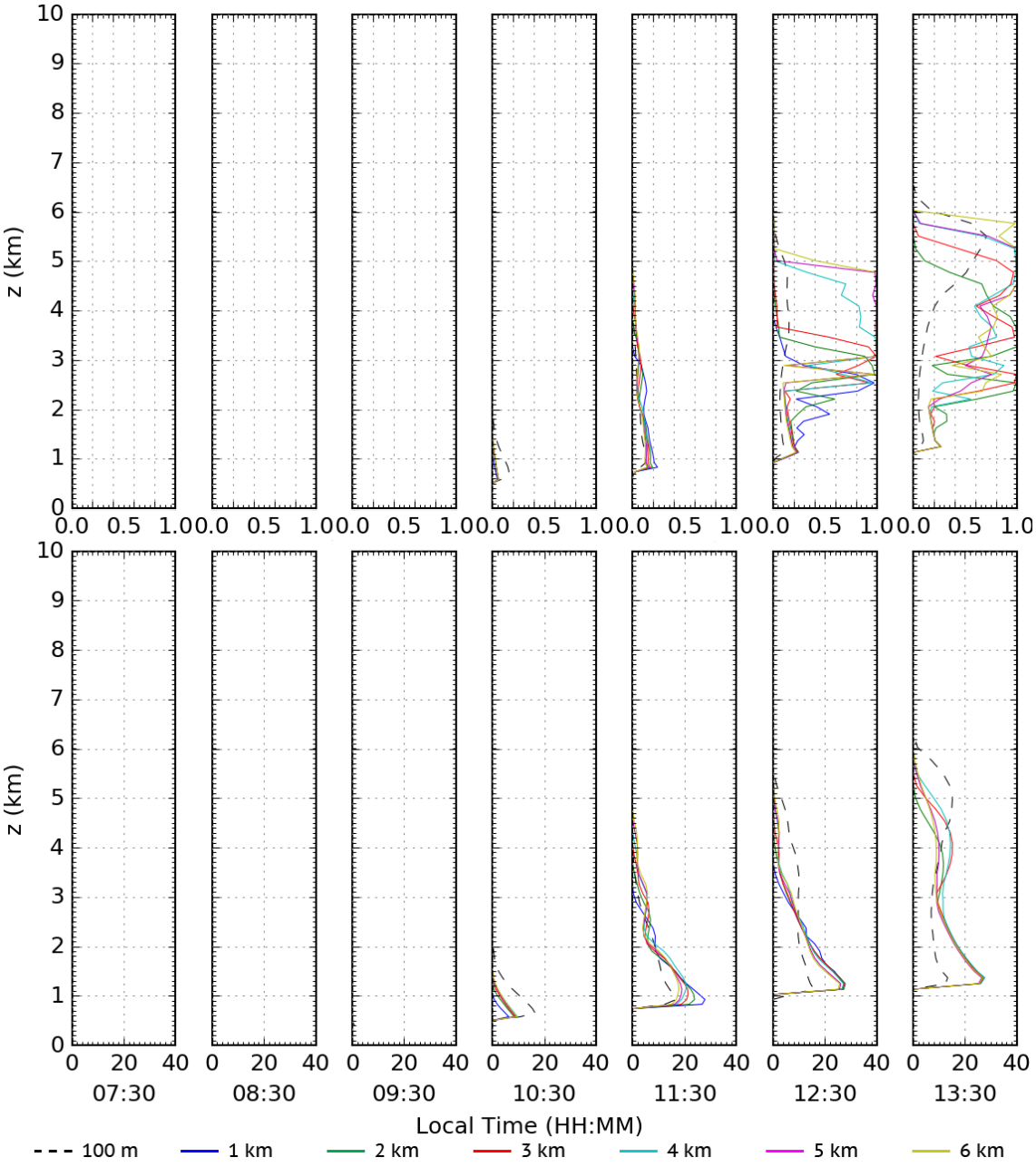

Figure 6.11: *Evolutions of vertical cloud fraction (top) and updraught mass-flux (bottom) profiles of all six SPMF-enabled 'grey-zone' simulations of the LBA case at different model times.*

The simulations share two other common undesired characteristics: an excessively saturated layer between 3 km and 6 km after 4.5 hours into the simulations, as well as intermittent initiation of sub-grid convection. Figure 6.12 shows that the saturated layer is produced by the explicit cloud scheme, which is consistent with the assertion that the large-scale condensation scheme is scale-dependent. The intermittent initiation may be correlated with a fluctuating temporal profile of CIN as shown in Figure 6.13. This may arise from the limited number of grid points across the

domain (especially for the 16 x 16 simulation at $\Delta x = 6$ km) such that the entire domain alternates between convective (low-CIN) and subsidence (high-CIN) phases.

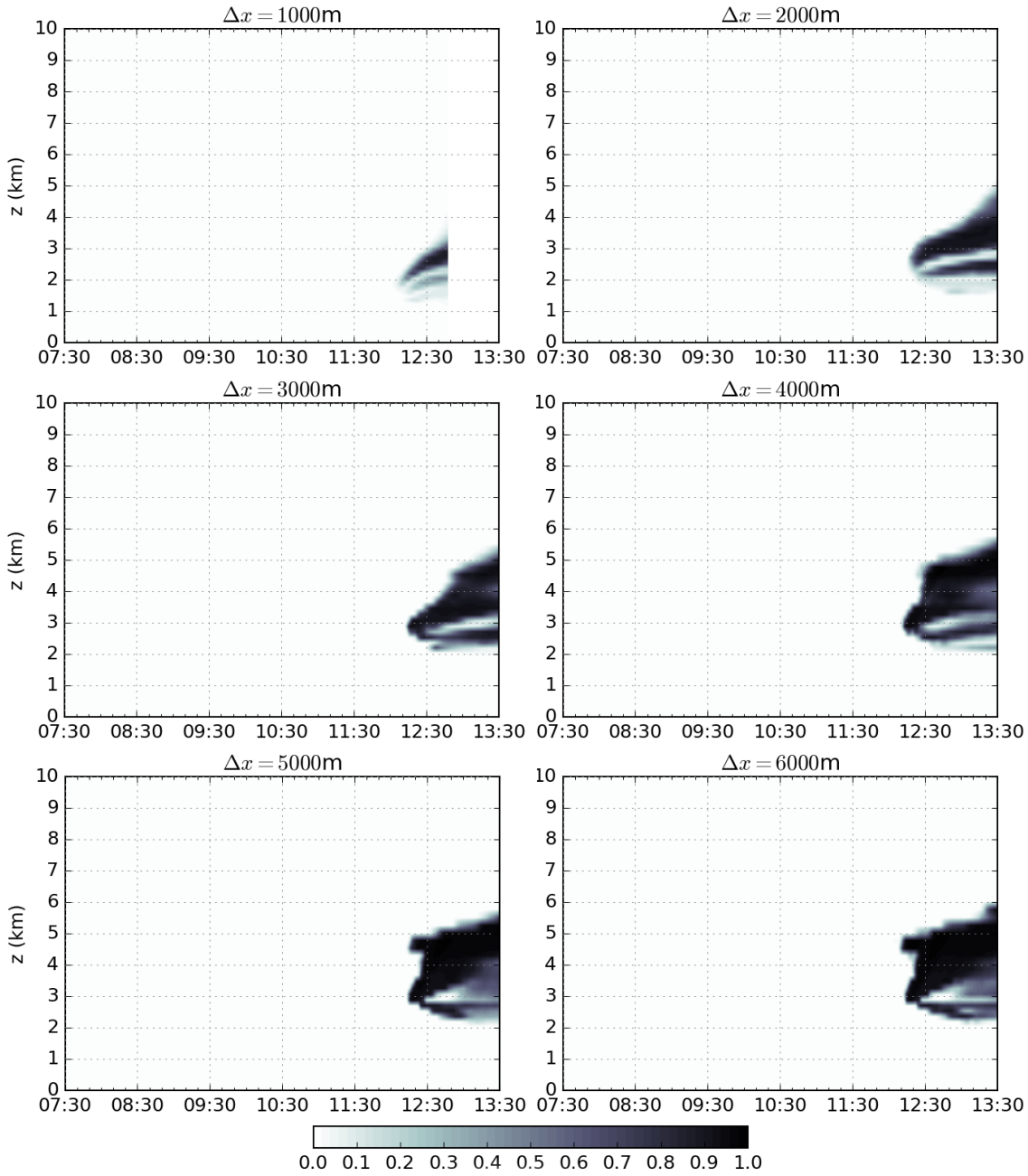

Figure 6.12: *Evolution of explicit cloud fraction in SPMF-enabled simulations of the LBA case at different 'grey-zone' resolutions. The explicit cloud fraction at a grid point is* $1 - \sigma_{\mathrm{u}}$ *if* $Q_{\mathrm{e}} \geq \min(10^{-5}, 0.01 q_{\mathrm{e_{sat}}})$ *kg / kg*$^{-1}$*, or 0 otherwise.* Q_{e} *and* $q_{\mathrm{e_{sat}}}$ *are the environmental cloud condensate mixing ratio and saturation water vapour mixing ratio respectively and are diagnosed using Equation* (4.4.2)*.*

'

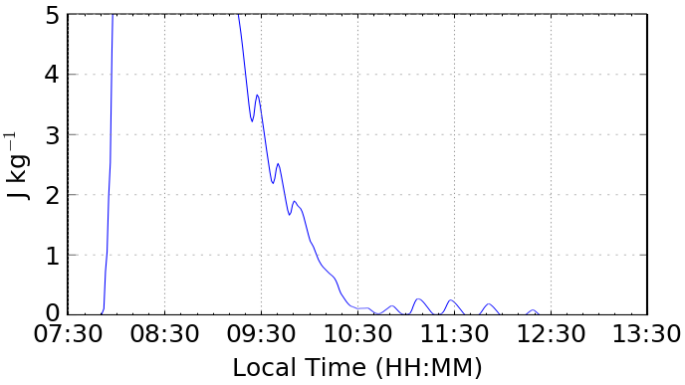

Figure 6.13: *The evolution of CIN in the simulation of the LBA case at $\Delta x = 6$ km with SPMF enabled.*

Figure 6.14 shows that the evolution of vertically integrated LWP among the 'grey-zone' simulations with SPMF enabled is in better agreement when compared with their no-scheme counterpart. The mean profile is consistent with the initiation of sub-grid convection at $\Delta t = 3$ hours as well as the accumulation of liquid water between 3 and 6 km in the vertical. However, the liquid water path slightly decreases with increasing resolution, which is consistent with the vertical cloud fraction profile analysis which shows that the maximum height of convective plumes decreases as the resolution increases. This reinstates that the vertical extent of sub-grid convection produced by SPMF is scale-dependent.

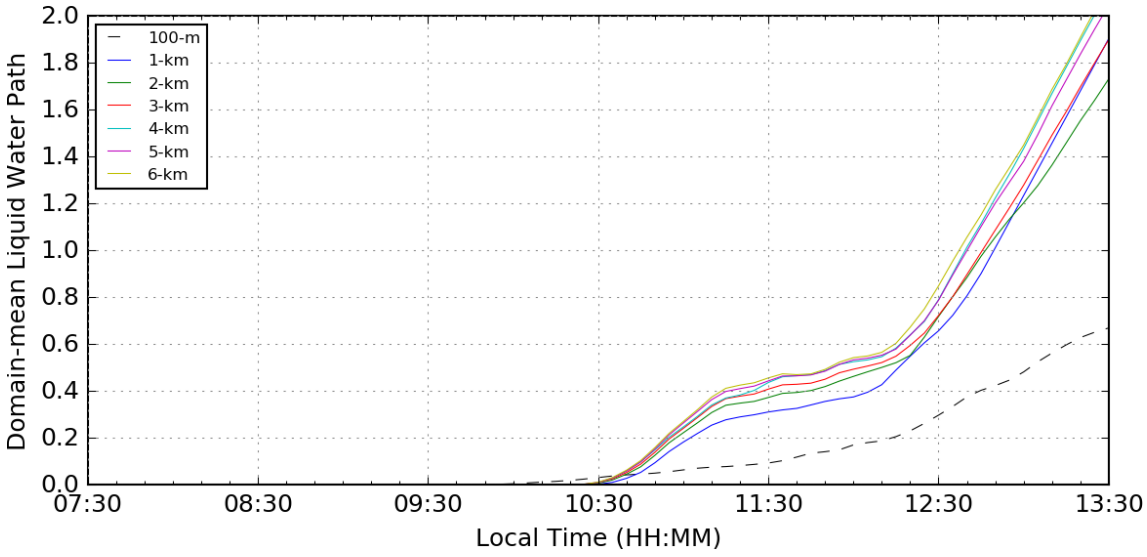

Figure 6.14: *Evolution of domain mean vertically integrated LWP of all six SPMF-enabled 'grey-zone' simulations and the reference simulation of the LBA case at different model times.*

6.3.3 Thermodynamic profile

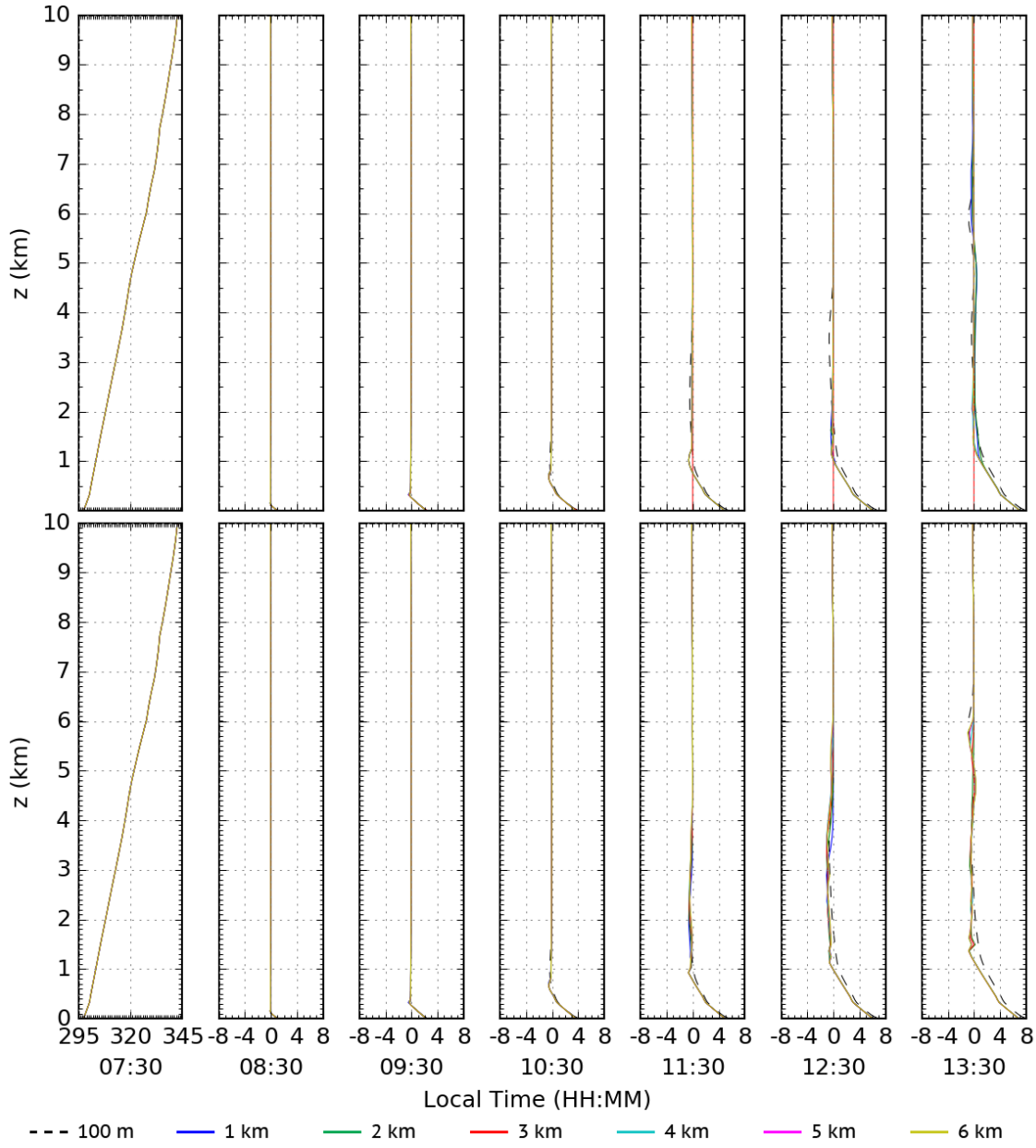

Figure 6.15: *Evolutions of potential temperature vertical profile of all six 'grey-zone' simulations of the LBA case without (top) and with (bottom) SPMF enabled at whole hours after initiation. The left-most graph shows the initial profile as in Grabowski et al. (2006), while the remaining show the deviation from the initial.*

Figure 6.15 and 6.16 compare the evolutions of the vertical profile of domain-mean potential temperature and water vapour between 'grey-zone' simulations without and with SPMF enabled. The lack of convection in all 'grey-zone' simulations without a convection scheme leads to little scale dependence in the evolutions of both quantities up to the fifth hour into the simulation. At

the sixth hour, higher resolution members develop a slightly warmer and moister layer above the boundary layer, which is consistent with condensation heating and moisture transport associated with explicit convection. In contrast, the evolutions among SPMF-enabled simulations are in tight agreement with each other through the entire simulation. However, the consensus deviates from the reference simulation with a cooler and moister boundary layer and warmer and drier free troposphere towards the last two hours. This suggests that while the vertical transports of heat and moisture are scale-independent, SPMF leads to a small systematic bias.

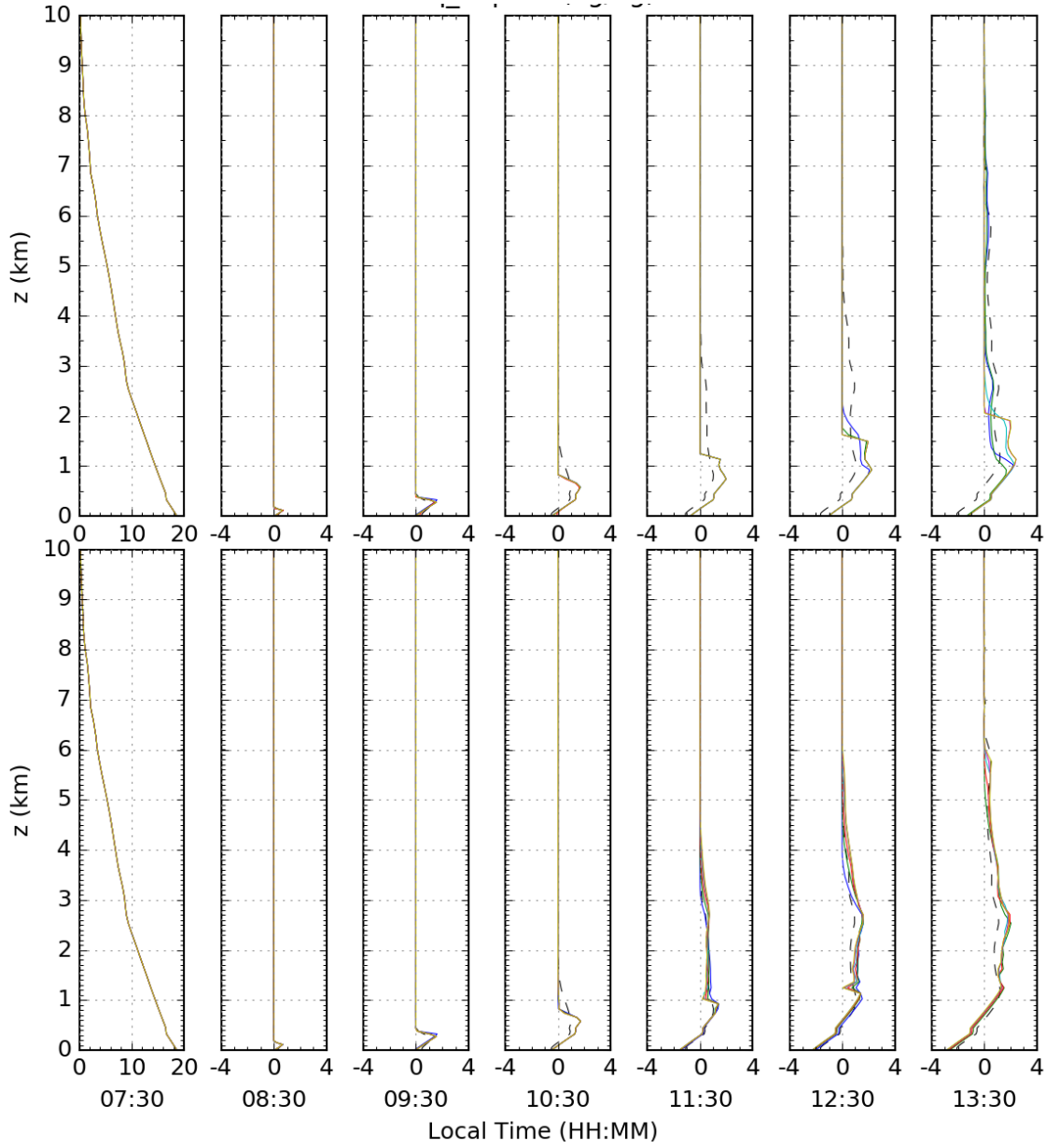

Figure 6.16: *Evolutions of water vapour vertical profile of all six 'grey-zone' simulations of the LBA case without (top) and with (bottom) SPMF enabled at whole hours after initiation. The left-most graph shows the initial profile as in Grabowski et al. (2006), while the remaining show the deviation from the initial.*

6.3.4 Energy conservation

Figure 6.17 shows the evolution of domain-mean vertically integrated moist static energy (MSE) in each of the 'grey-zone' simulations with the SPMF scheme enabled, as well as the expected evolution which is calculated by taking into account the prescribed cooling and surface fluxes. There is a 10% loss of moist static energy between the fourth hour and fifth hour into the simulation. An additional analysis (not shown) suggests that the loss is related with the sensible heat. Since a mass flux scheme only induces tendencies to redistribute quantities, it is by design energy conserving. This suggests that the loss of heat energy could be due to some mishandling of residual sub-grid convection causing spurious negative tendencies.

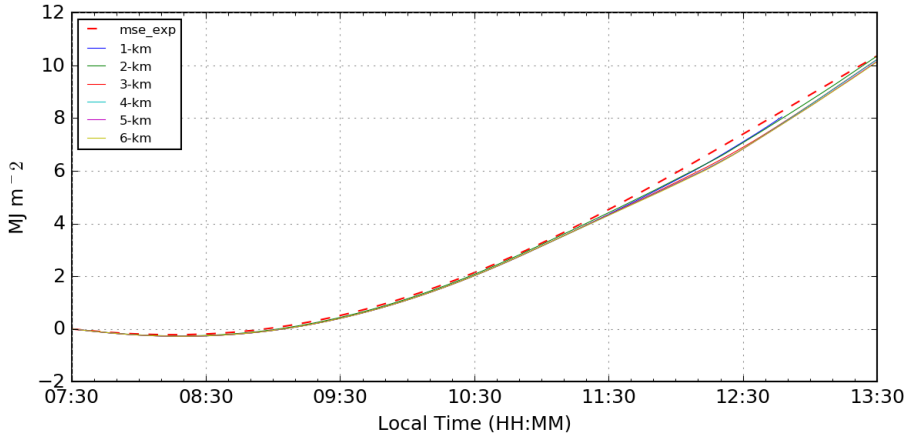

Figure 6.17: *The evolution of domain-mean vertically integrated MSE in each 'grey-zone' simulation of the LBA case with the SPMF enabled. The MSE S is defined as* $S = c_p T + gz + Lq_v$*, where* T *is the dry-bulb temperature,* z *is the height and* q_v *is the water vapour mixing ratio of the parcel.*

6.4 Characteristics of sub-grid updraughts

6.4.1 Vertical profile

Figure 6.18 shows the evolution of mean vertical temperature profile of sub-grid convective updraughts parameterised by SPMF. It illustrates that scale awareness holds for the updraught for both quantities at cloud base, but the profiles gradually diverge at increasing height. The discrepancy is the greatest at the onset of sub-grid convection and gradually decreases with time. In addition, the maximum height, temperature and moisture of sub-grid convective updraughts decrease with increasing resolution. In fact, this identical trend also exists in the liquid water mixing ratio and vertical velocity as shown in Figure 6.19. The discrepancy in updraught vertical velocity explains the scale-dependence of the cloud top height and the onset of grid-scale condensation, as weaker

convective updraught velocity corresponds to a slower vertical transport of heat and moisture up the troposphere. This is found to be related to the scale dependence of the entrainment source term as shown in Figure 6.20. As I will explain in detail in the next chapter, the scale dependence arises from the use of the bulk plume approach and the chosen entrainment parameterisation which depends on the radius of the bulk plume.

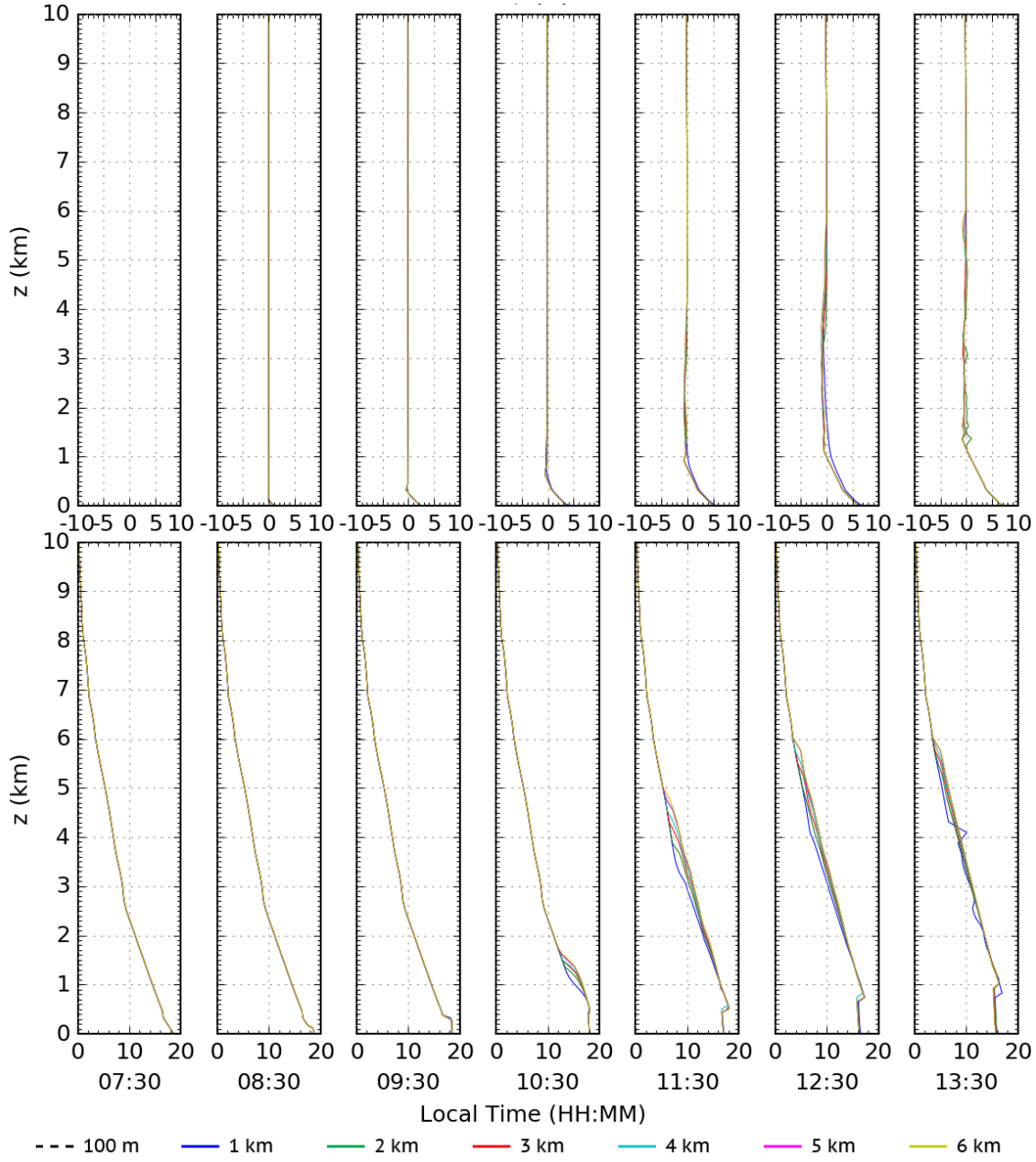

Figure 6.18: *Evolution of the domain-mean sub-grid updraught potential temperature perturbation (top, in K) and water vapour (bottom, in g kg^{-1}) in 'grey-zone' simulations of the LBA case with SPMF enabled.*

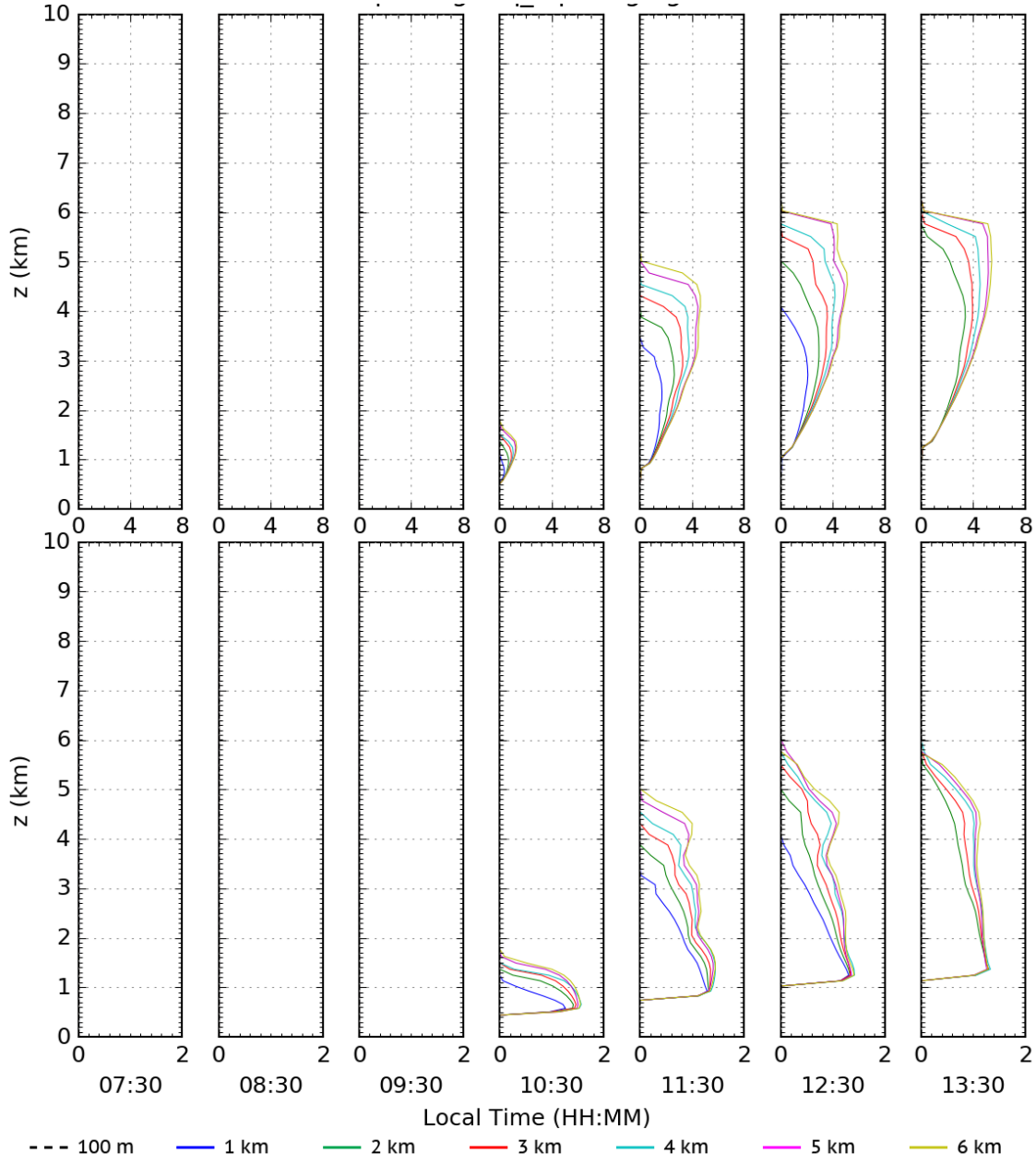

Figure 6.19: *Evolution of the domain-mean sub-grid updraught liquid water mixing ratio (top, in g kg^{-1}) and vertical velocity (bottom, in m s^{-1}) in 'grey-zone' simulations of the LBA case with SPMF enabled.*

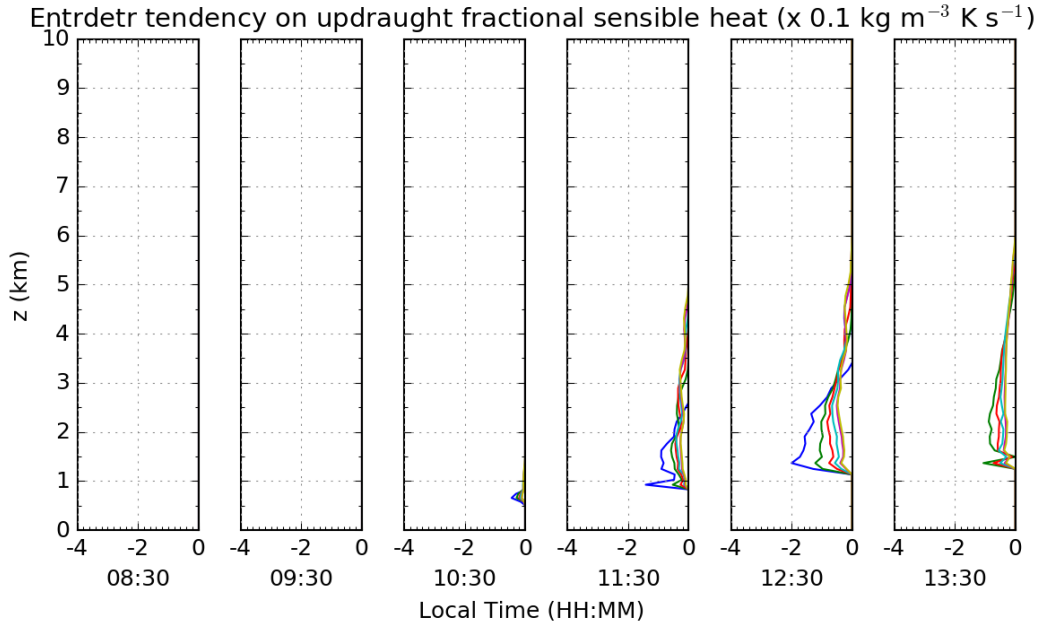

Figure 6.20: *Evolution of the domain-mean entrainment source term on the sub-grid convective sensible heat in all six 'grey-zone' simulations of the LBA case with convection scheme enabled. Colour of each line represents the grid-length of each simulation as follows: blue = 1 km, green = 2 km, red = 3 km, aqua = 4 km, purple = 5 km, yellow = 6 km. Results of simulation at $\Delta x = 1$ km not shown at 13:30 LST as the model has crashed by that time.*

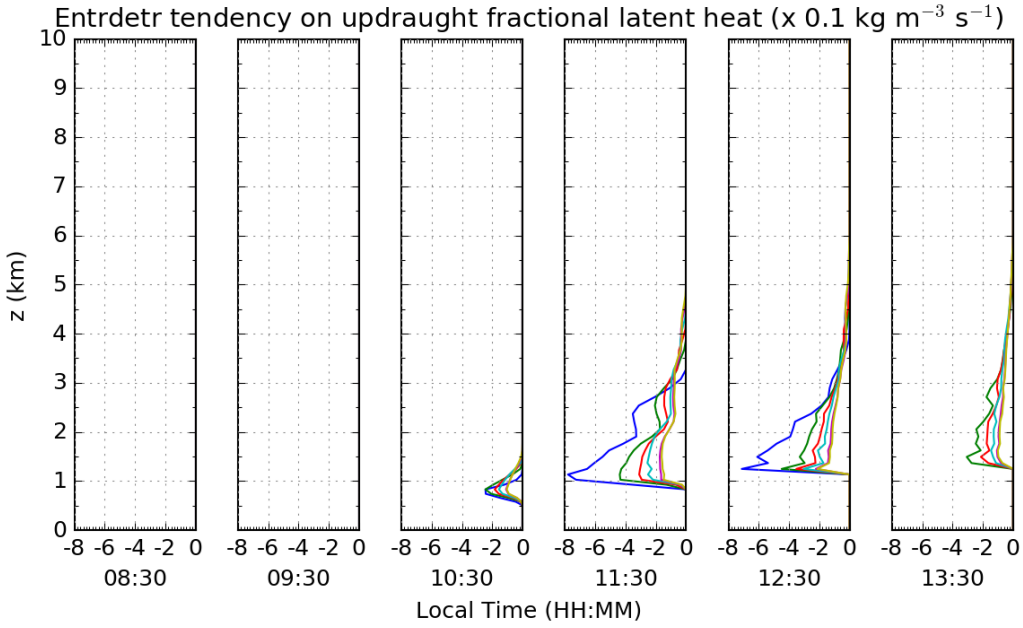

Figure 6.21: *Evolution of the domain-mean entrainment source term on the sub-grid updraught fractional latent heat in all six 'grey-zone' simulations of the LBA case with convection scheme enabled. Colour of each line represents the grid-length of each simulation as follows: blue = 1 km, green = 2 km, red = 3 km, aqua = 4 km, purple = 5 km, yellow = 6 km. Results of simulation at $\Delta x = 1$ km not shown at 13:30 LST as the model has crashed by that time.*

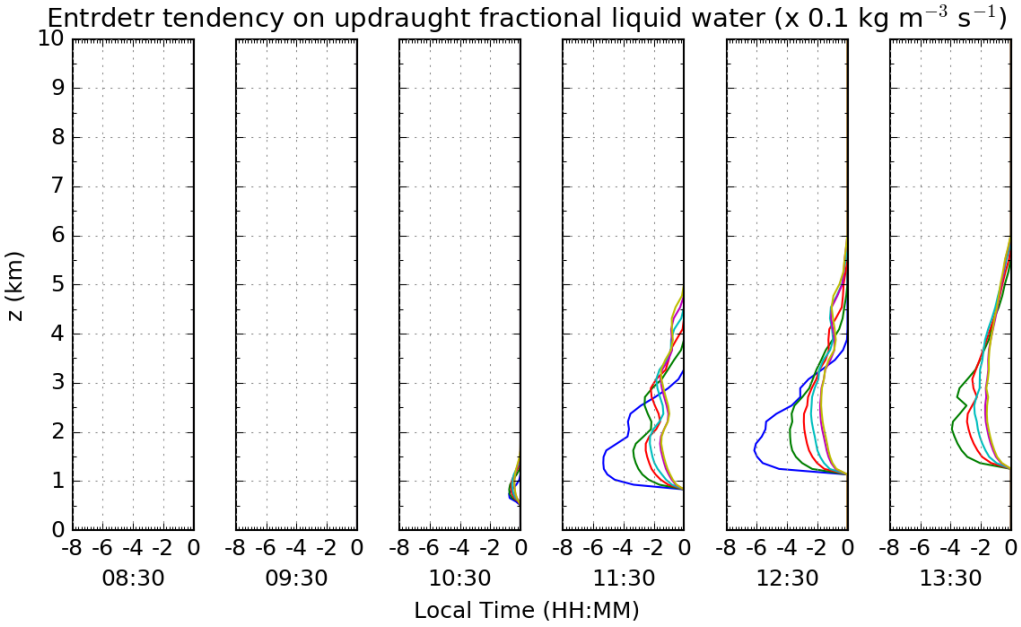

Figure 6.22: *Evolution of the domain-mean entrainment source term on the sub-grid convective updraught fractional liquid water in all six 'grey-zone' simulations of the LBA case with convection scheme enabled. Colour of each line represents the grid-length of each simulation as follows: blue = 1 km, green = 2 km, red = 3 km, aqua = 4 km, purple = 5 km, yellow = 6 km. Results of simulation at $\Delta x = 1$ km not shown at 13:30 LST as the model has crashed by that time.*

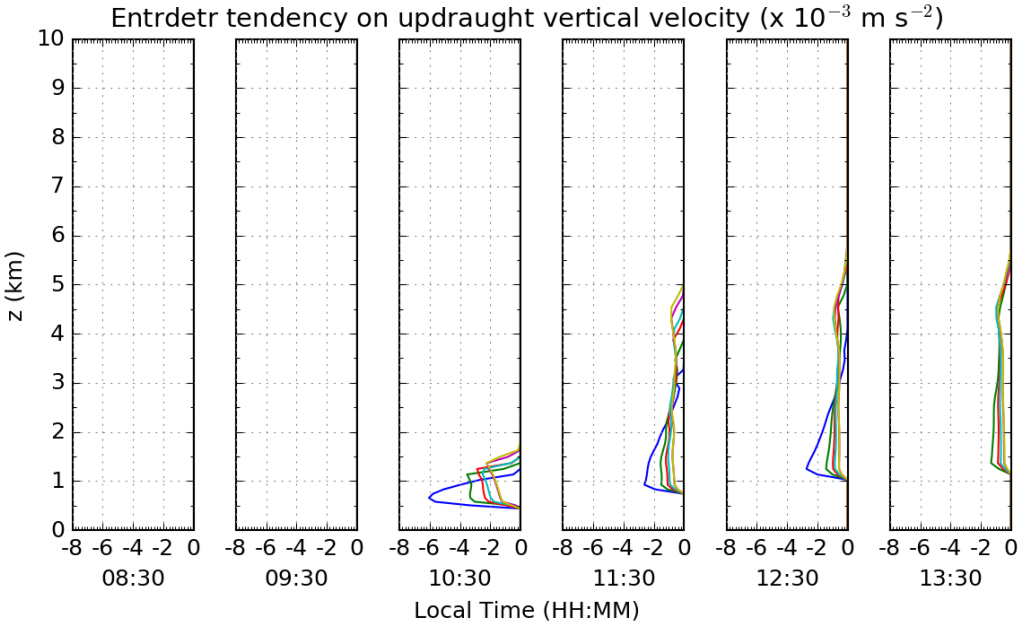

Figure 6.23: *Evolution of the domain-mean entrainment source term on the sub-grid convective updraught velocity in all six 'grey-zone' simulations of the LBA case with convection scheme enabled. Colour of each line represents the grid-length of each simulation as follows: blue = 1 km, green = 2 km, red = 3 km, aqua = 4 km, purple = 5 km, yellow = 6 km. Results of simulation at $\Delta x = 1$ km not shown at 13:30 LST as the model has crashed by that time.*

6.4.2 Horizontal variability

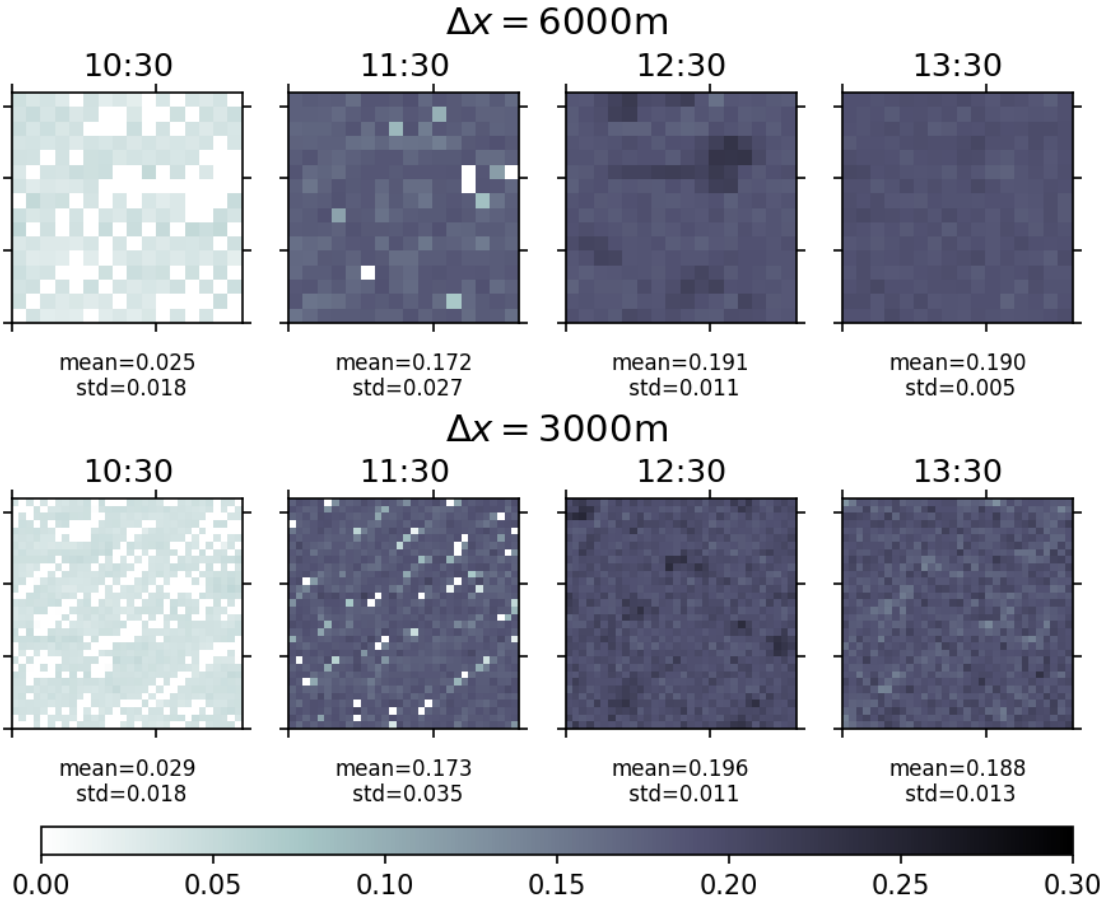

Figure 6.24: *Horizontal distribution of σ_u at cloud base at different times throughout the simulation of the LBA case at Δx =6 km and Δx =3 km with SPMF enabled. The 'mean' and 'std' below each plot refer to the horizontal mean and standard deviation at the corresponding time respectively.*

Figure 6.24 shows the evolution of horizontal distribution of σ_u at cloud base throughout the simulation of the LBA case with the convection scheme enabled at $\Delta x = 6$ km and $\Delta x = 3$ km respectively. In both simulations, the standard deviation of σ_u increases over time up to 11:30 LST as the trigger function becomes increasingly stochastic as a response to increasing surface heat flux and thus w^*, before reducing dramatically as sub-grid convection is initiated across the entire domain. More importantly, the standard deviation in the 3-km simulation is approximately twice of that in the 6-km simulation. These behaviours are also evidence in the evolution of horizontal variability of w_u at cloud base as shown in Figure 6.25. This suggests that the trigger function produces a scale-aware horizontal variability with similar domain-mean, implying that SPMF does not suppress explicit convection in simulations at a sufficiently high resolution.

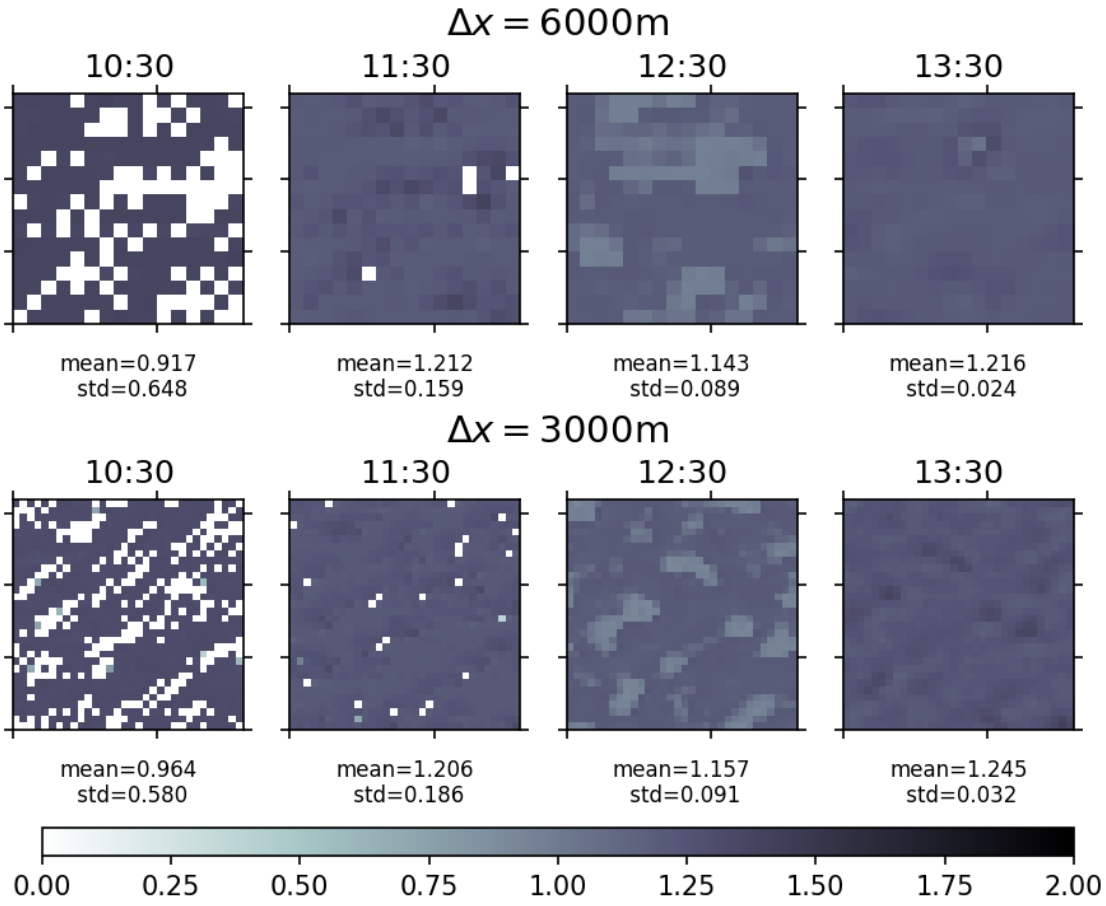

Figure 6.25: *As Figure 6.24, but for* w_{u}.

6.5 Compensating subsidence

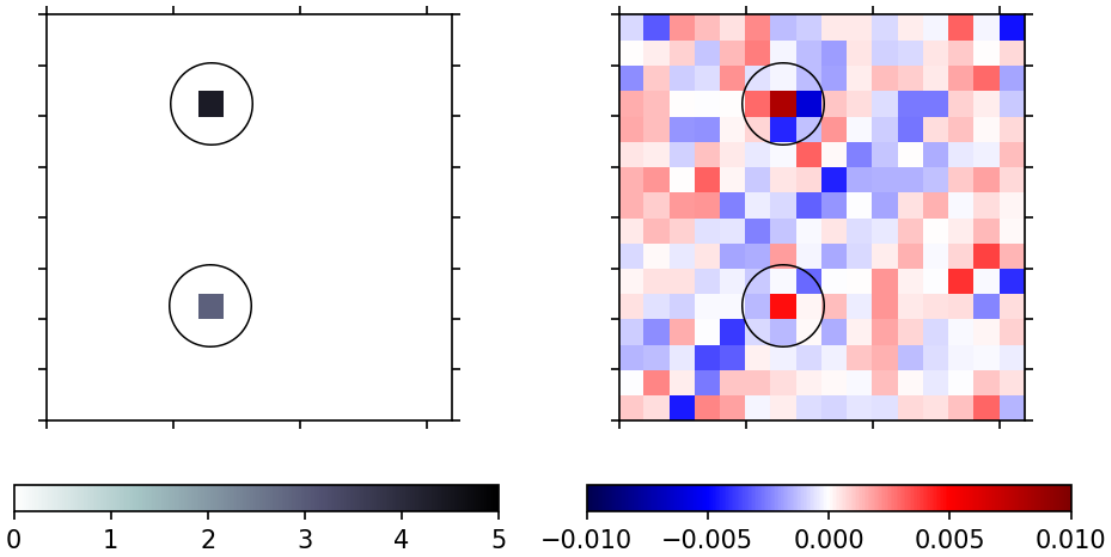

Figure 6.26: *Horizontal distributions of w_{u} (left) and w (right) in m s^{-1} at $z = 539.44$ m at $t = 9211.87$ s of a simulation of the LBA case at $\Delta x = 1$ km over a domain of 16 x 16 with SPMF enabled.*

Figure 6.26 shows the horizontal variability of both w_u and w at the initiation of the earliest sub-grid updraughts in a special 1-km simulation where the strengths of sub-grid updraughts was substantially magnified. Stronger downward motion is present at grid points adjacent to one with a sub-grid updraught, suggesting that the dynamical core does trigger non-local compensating subsidence. The resolved w at a grid point with a sub-grid updraught with $\sigma_c = 0.2$ and $w_{\mathrm{u}} = 5$ m s^{-1} is only 0.01 m s^{-1}, meaning that the vertical velocity of the sub-grid cloud-free environment is approximately -1.24 m s^{-1}. This implies the existence of local compensating subsidence, although the magnitude is excessive as subsiding shells with strength of -1.2 m s^{-1} are found only up to 400 m away from convective updraughts in the LBA case (Savre, 2021). The excess is possibly the result of the inconsistent treatment of net mass transport by convection between SPMF and the dynamical core.

6.6 Chapter summary

The performance of the SPMF scheme was evaluated. The analysis suggests that the implementation of the scheme improves the performance of simulations of a diurnal cycle test case at 'grey-zone' resolutions against having no parameterisation. It significantly reduces the differences in the

initiation time of convection and maintains a similar evolution of the vertical profiles of heat and moisture between simulations at different 'grey-zone' resolutions. It also produces scale-aware horizontal variability across a largely homogeneous domain. The scheme reduces the disagreement between the 'grey-zone' simulations and the reference simulation. Nonetheless, it has been revealed that a relatively minor degree of scale-dependence remains which is related increasing entrainment rate with resolution. The next chapter will focus on revealing the origin of the scale-dependence and whether it is possible to reduce the systematic error by altering some of the free parameters.

Chapter 7

Sensitivity of SPMF to uncertainties

7.1 Introduction

In Chapter 6, it was shown that while SPMF successfully reduces the scale-dependence of simulations of the diurnal cycle of convection at 'grey-zone' resolutions, some scale dependence remains, especially of the rate of vertical growth of sub-grid convection as a result of scale-dependent entrainment. In addition, some discrepancies exist between the 'grey-zone' simulations with the convection scheme enabled and the reference scheme, such as the initiation time of convective updraughts and the cloud fraction approaching the cloud-top. With several tuneable aspects in the scheme, it is important to assess whether how these affect its performance in simulating the diurnal cycle of convection, in particular the initiation and growth of convection which conventional schemes do not handle well. This chapter focuses on the sensitivity of SPMF to two parameters: entrainment rates on plume growth in Section 7.2 and the width of the w_{u} distribution at BL top on plume initiation time in Section 7.3. Finally, Section 7.4 examines if the performance of SPMF is time-step independent, which is a requirement for a convection scheme to be suitable for general use.

7.2 Sensitivity to the entrainment parameterisation

The SPMF scheme scales the entrainment rate on the radius of the bulk plume. While this approach may be suitable for modelling the evolution of one single plume, it is not a good approximation to

how the local population of plumes interact with the environment. In reality, the entrainment rate is proportional to the vertical surface area between all convective updraughts and the environment. With the same total cross-sectional (x-y plane) area, the total vertical surface area of plume increases with the degree of fragmentation (i.e. the number of updraughts) among the population. Thus, a population of small plumes is more efficient at interacting with the environment, i.e. they are more likely to remain shallow and to condition the environment via entrainment and detrainment. In contrast, a single large plume is more likely to retain its integrity through the ascent and reach greater heights.

Assuming that all plumes are of equal size in the horizontal, the area occupied by a single plume A_{u_i} is given by

$$A_{u_i} = \frac{A_u}{N_u} \tag{7.2.1}$$

where A_u is the total area occupied by convective updraughts and N_u is the number of convective updraughts in the population. It follows that the radius of a single updraught R_i, assuming that they are circular on the horizontal, is given by

$$R_i = \sqrt{\frac{A_u}{N_u \pi}} \tag{7.2.2}$$

Thus, the vertical surface area of a cylindrical updraught is

$$A_{l_i} = 2\pi R_i h_u = 2\pi h_u \sqrt{\frac{A_u}{N_u \pi}} \tag{7.2.3}$$

where h_u is the mean vertical extent of the convective updraughts. The total vertical surface area of the entire updraught population A_l is given by

$$A_l = N_u 2\pi R_i = 2N_u \pi \sqrt{\frac{A_u}{N_u \pi}} = 2\sqrt{N_u \pi A_u} \tag{7.2.4}$$

Therefore, the relative error due to the single updraught assumption varies with $\sqrt{N_u}$ given the same A_u, and is directly proportional to the grid length Δx as $N_u \sim \Delta x^2$. Given the same σ_{u}, this choice of parameterisation produces stronger entrainment rate at higher resolution and thus induces scale dependence across the 'grey-zone' resolution. This is verified by a re-simulation of the LBA case at $\Delta x = 6$ km with the convection scheme enabled but with six times the entrainment rate so that it matches that in the $\Delta x = 1$ km. Figure 7.1 shows that the rate of growth of convective

updraughts is reduced such that the evolution of cloud fraction is in better agreement with that in the LBA simulation at $\Delta x = 1$ km.

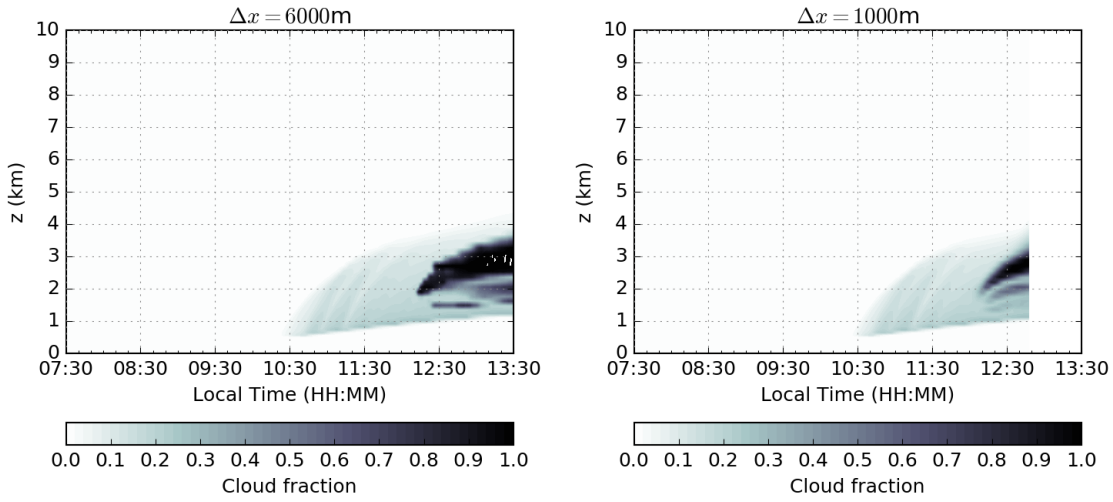

Figure 7.1: *Comparison of the evolution of cloud fraction between the LBA simulation at $\Delta x = 6$ km with six times the original entrainment rate and that at $\Delta x = 1$ km with the original entrainment rate (c.f. Figure 6.10.*

7.3 Sensitivity of the initiation time and sub-grid variability to the parameterisation of BL top variability

In the convection scheme, the stochastic trigger assumes that the distribution of vertical velocity at the top of the boundary layer is Gaussian, with the grid-mean value as the mean and βw^* as the standard deviation where β is a tunable parameter. In the evaluation in Chapter 6, β is assumed to be 0.2 following Lenschow and Stephens (1980).

7.3.1 Initiation time

Since β determines the width of the distribution of w at BL top, it plays a pivotal role in controlling the onset time of sub-grid convection. The wider the distribution, the more likely a sufficiently strong thermal occurs and thus the earlier the first cloud initiates. This is verified by performing an extra simulation of the LBA case at $\Delta x = 6$ km with the convective parameterisation scheme enabled but with $\beta = 1.0$. As shown in figure 7.2, cloud initiates approximately 40 minutes earlier in the simulation with the higher value of β compared to the default value of 0.2. This suggests that the performance of the scheme is sensitive to the choice of β and implies that it is possible to reduce the systematic error in the initiation time by tuning β.

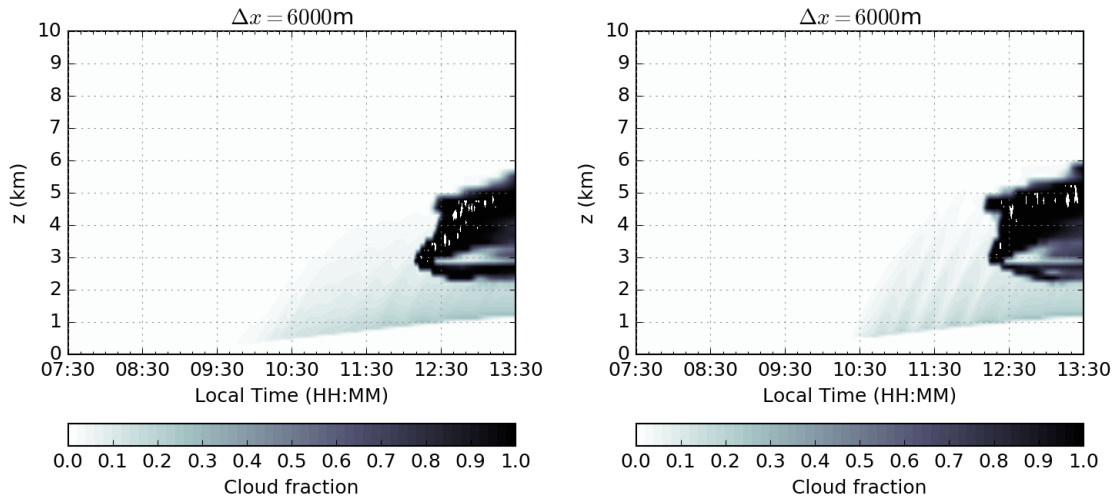

Figure 7.2: *Comparison of the evolution of cloud fraction between two simulations of the LBA case performed at $\Delta x = 6$ km with convection scheme enabled, one (left) with $\beta = 1.0$ and the other (right) with $\beta = 0.2$.*

7.3.2 Horizontal variability

In addition to the timing of convective initiation, the choice of β also affects the variability over a horizontally homogeneous domain as it directly determines the standard deviation of the vertical velocity distribution. As shown in Figure 7.3, the standard deviation of w_{u} at cloud base is higher in the simulation with $\beta = 1.0$ than that in the simulation with $\beta = 0.2$ at $\Delta x = 6$ km. It is worth noting that the standard deviation in the simulation with $\beta = 1.0$ is not five times that in the simulation with $\beta = 0.2$ due to different timings of convective initiation, complicated by the oscillation of CIN and other processes. By comparing Figure 7.4 to 6.24, the variability of σ_{u} is lower in the simulation with a higher β at identical model times. This could be due to an earlier onset of sub-grid plumes such that sub-grid updraughts are within most grid boxes earlier (thus suppressing variability).

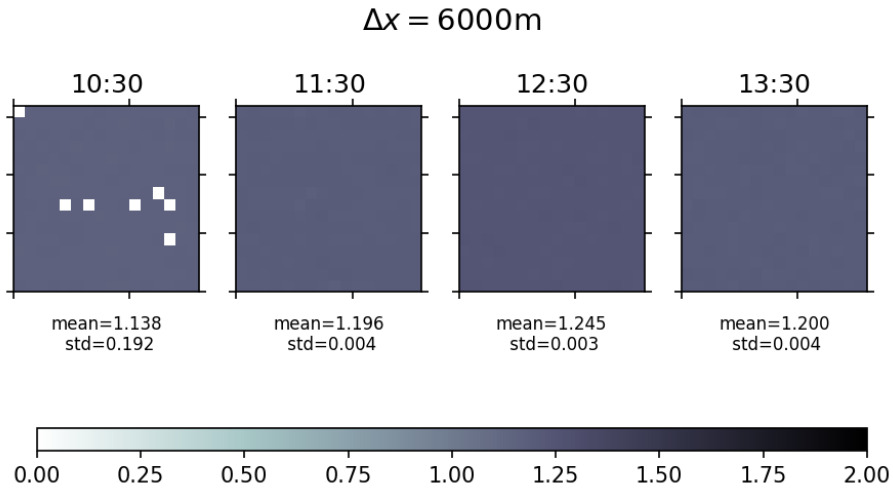

Figure 7.3: *The evolution of horizontal variability of w_{u} at cloud base in the simulations of the LBA case performed at $\Delta x = 6$ km with convection scheme enabled and with $\beta = 1.0$.*

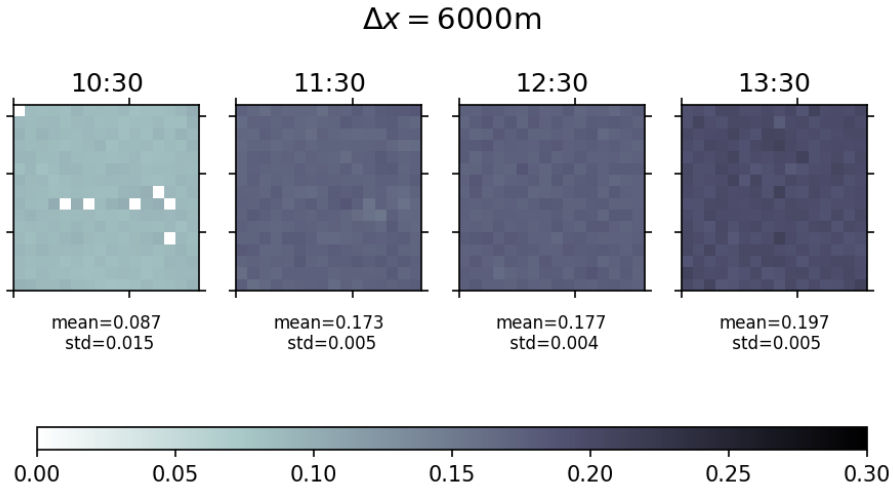

Figure 7.4: *The evolution of horizontal variability of σ_{u} at cloud base in the simulations of the LBA case performed at $\Delta x = 6$ km with convection scheme enabled and with $\beta = 1.0$.*

7.4 Sensitivity to model time-step

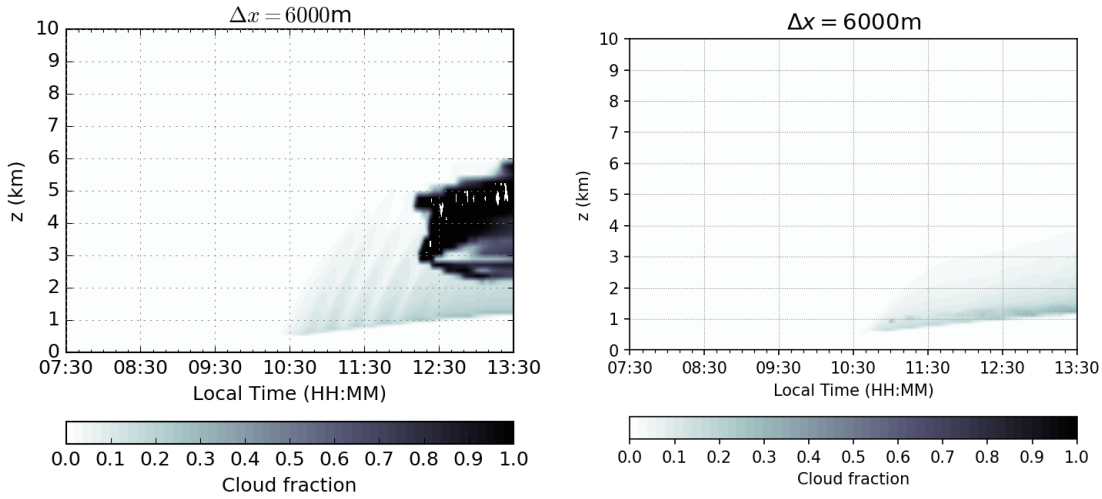

Figure 7.5: *Comparison of the evolution of cloud fraction between two simulations of the LBA case performed at $\Delta x = 6$ km SPMF enabled, one (left) with $\Delta t_{\min} = 0.5$ s and the other (right) with $\Delta t_{\min} = 0.25$ s.*

The sensitivity of SPMF to time-step was evaluated by varying $\Delta t_{\min}$, the MONC parameter introduced for the modified Smagarinsky mixing scheme to control the maximum allowed viscosity coefficient $\nu_{\max}$ at 'grey-zone' resolutions. Figure 7.5 reveals a slower vertical development of sub-grid plumes by SPMF in the simulation with a lower $\Delta t_{\min}$. This is an unexpected and highly concerning behaviour as time-step dependence is a serious limitation of a convective scheme. As neither the trigger function nor the plume model is time-step dependent in principle, it could be related to some unidentified interactions between the modified Smagarinsky scheme and the trigger function and/or other components in MONC, or simply a software defect. The root cause of this time-step dependence is not determined in this project.

Chapter 8

Conclusion and Future Work

8.1 Introduction

A new mass flux convection scheme with prognostic and stochastic treatment of sub-grid convection (SPMF) is proposed to improve the scale-awareness of simulations of diurnal cycle of convection over land across the 'grey-zone'. The convection scheme employs a stochastic boundary layer closure, relating the initiation and fractional coverage of sub-grid convection to the size and initiation of boundary layer thermals which are sufficiently strong to penetrate through any convective inhibition existing above the boundary layer. In addition, the scheme explicitly solves the budget equations to prognose the evolution of sub-grid convection. This includes advecting the convective plumes vertically with the vertical velocity of the convective updraught using an advection scheme so that convective plumes do not reach full height immediately as in traditional parameterisation relying on a quasi-equilibrium assumption. The performance of convection scheme was evaluated by comparing simulation results of the LBA case modelled at different resolutions across the 'grey-zone'. This chapter summarises the findings, answers the research questions set out in Chapter 6 and proposes directions for future research.

8.2 Answers to the research questions

1. Is it possible to construct a convective parameterisation scheme that works in the 'grey-zone'?

The presented results show that by introducing stochasticity to a boundary-layer based closure and prognosing the evolution of sub-grid plumes, it is possible to construct a scheme which significantly improves the simulation of convection at 'grey-zone' resolutions.

2. Is an accurate parameterisation of boundary layer turbulence important for a successful simulation of diurnal cycle of convection in the 'grey-zone'?

   This study suggests that while SPMF improves the diurnal cycle of convection at 'grey-zone' resolutions, it is sensitive to the choice of the width of the assumed distribution of w_{u} from which random numbers are drawn to stochastically determine the onset of sub-grid convection. It alters the initiation time of convection as well as controls the horizontal variability across a homogeneous domain. Therefore, this suggests that an accurate parameterisation of the boundary layer plays an pivotal role in simulating the diurnal cycle of convection.

8.3 Limitations of SPMF and future work

8.3.1 The lack of horizontal advection of convective plumes

In SPMF, the horizontal advective tendencies on convective prognostics were ignored as a simplification. However, this would lead to increasing decoupling of sub-grid convection from the large-scale as grid-lengths decrease towards the length scale of a convective plume; the modified environment due to convection would be advected away from the associated convective plume, while the convective plume modifies a new environment which is advected into the grid in the next time-step. This artificial "shear" prevents the warming and moistening effect from remaining vertically stacked. While evaluating this effect is beyond the scope of this study, it is sensible to assume that horizontal advection of plumes may lead to a delayed transformation from sub-grid convection to explicit convection. Thus, it may be important for future research to derive a good approach modelling the horizontal movement of plumes as discrete structures in SPMF. Possible starting points include the cellular automata approach proposed by Bengtsson et al. (2013), the conditional filtering multi-fluid framework by Thuburn et al. (2018) and extended EDMF by Tan et al. (2018).

8.3.2 The lack of a true microphysics scheme and downdraught parameterisation

The two-moment condensation scheme incorporated in SPMF is too simple. The lack of ice might lead to underestimation of cloud top heights and overestimation of cloud coverage at cloud top. The absence of rain and convective downdraughts prevents SPMF from producing cold pools, which could stabilise the local atmosphere and trigger additional non-local convection. To minimise inconsistency between the convection forcing and the large-scale forcing, future researchers should attempt to use the same microphysics as the model default microphysics scheme for grid-scale convection. For instance, CASIM should be interfaced with the convection scheme if MONC is used as the model for evaluation.

8.3.3 Inconsistencies between the dynamical core and sub-grid convection

Allowing the unmodified dynamical core to solve for grid-mean pressure and vertical velocity alongside with forcings from SPMF lead to inconsistencies which could have explained the problems seen in SPMF-enabled simulations. Future researches on SPMF should ensure that the net mass transport due to convection is treated consistently with the dynamical core by ensuring the induction of tendencies on the resolved-scale pressure field. They should also modify the dynamical core of the host model such that it only solves for w_e to avoid double counting in $\overline{w}$.

8.3.4 The crash of the LBA simulation at $\Delta x = 1$ km

As mentioned in the Chapter 6, the SPMF-enabled simulation of the LBA case at $\Delta x = 1$ km failed after approximately 5.5 hours in model time. The cause of this failure was not found and should be investigated in future studies, in particular how instabilities associated with inconsistent treatment of vertical mass flux from the negligence of pressure tendencies for $\sigma_u \approx 1$, affect simulations at the higher-resolution end of the 'grey-zone'.

8.3.5 Simplified trigger function

The stochastic trigger function of SPMF does not currently introduce sub-grid plumes with perturbed scalar quantities at cloud base. Future researchers could explore the possibility of calculating cloud-base T_u and q_u based on the buoyancy necessary to achieve the cloud-base vertical velocity determined by the stochastic process.

8.3.6 Limited test case

The performance of SPMF was only evaluated in one test case of the diurnal cycle. The LBA case is a typical diurnal cycle featuring non-equilibrium convection but the amount of CIN present in the initial sounding is weak. Stronger convective inhibition of order 100 J kg^{-1} are not uncommon, especially across central United States as an elevated mixed layer exists over the boundary layer. It would be interesting to evaluate the performance of this scheme on test cases involving stronger CIN and more significant delay in the onset of convection (i.e. afternoon thunderstorms).

8.3.7 Non-comprehensive sensitivity test

Sensitivity of SPMF to some parameters is yet to be evaluated, for example the size of a BL thermal. A more in-depth sensitivity test and analysis should be performed to understand the behaviour of SPMF, in particular the apparent time-step sensitivity associated with interactions with boundary layer schemes since a time-step dependent scheme is of little practical value.

8.3.8 Limited test model

The convection scheme has only been implemented and tested in MONC, which is an anelastic and non-hydrostatic model. The performance of this scheme in other numerical models, including the real cases and NWP models, should be attempted to assess the influence on real weather forecasts.

8.3.9 Other possible enhancements

A multi-plume approach, for instance Gentine et al. (2013a,b) and Plant and Craig (2008), introduces size variation among plumes in the same grid box and thus cloud top heights due to differential entrainment and detrainment rates. This would further enhance the horizontal variability of convective response and is worth investigating. Weller and McIntyre (2019) proposes to represent sub-grid plumes and the environment as a multi-fluid problem; transfer terms of mass and buoyancy across plumes and environment are introduced to ensure tight coupling between the two fluids and a scale-aware representation of compensating subsidence. Merging this approach with SPMF is a good motivation for future studies.

Appendix A: The initial sounding profile of the LBA case

TABLE A.1. INITIAL SOUNDING

Height (km)	Pressure (hPa)	Temperature (°C)	RH (%)	U (m s^{-1})	V (m s^{-1})
0.130	991.3	23.70	98.00	0.00	−0.40
0.464	954.2	23.30	86.00	0.81	−3.51
0.573	942.0	22.57	88.56	1.17	−3.88
1.100	886.9	19.90	87.44	3.44	−4.77
1.653	831.5	16.91	86.67	3.53	−5.28
2.216	778.9	14.09	83.67	3.88	−5.85
2.760	729.8	11.13	79.56	4.09	−5.60
3.297	684.0	8.29	84.78	3.97	−2.67
3.824	641.7	5.38	84.78	1.22	−1.47
4.327	603.2	2.29	89.33	0.16	0.57
4.787	570.1	−0.66	94.33	−1.22	0.89
5.242	538.6	−3.02	92.00	−1.72	−0.08
5.686	509.1	−5.28	85.22	−2.77	1.11
6.131	480.4	−7.42	77.33	−2.65	2.15
6.578	454.0	−10.34	80.11	−0.64	3.12
6.996	429.6	−12.69	66.11	−0.07	3.22
7.431	405.7	−15.70	72.11	−1.90	3.34
7.881	382.5	−19.21	72.67	−2.70	1.91
8.300	361.1	−21.81	52.22	−2.99	1.15
8.718	340.9	−24.73	54.67	−3.66	1.01
9.149	321.2	−27.76	51.00	−5.05	−0.57
9.611	301.2	−30.93	43.78	−6.64	−0.67
10.084	281.8	−34.62	40.56	−4.74	0.31
10.573	263.1	−38.58	43.11	−5.30	2.97
11.008	246.1	−42.30	54.78	−6.07	2.32
11.460	230.1	−46.07	46.11	−4.26	2.66
11.966	213.2	−50.03	42.33	−7.52	4.79
12.472	197.0	−54.67	43.22	−8.88	3.40
12.971	182.3	−59.16	45.33	−9.00	3.14
13.478	167.9	−63.60	39.78	−7.77	3.93
13.971	154.9	−67.68	33.78	−5.37	7.57
14.443	143.0	−70.77	28.78	−3.88	2.58
14.956	131.1	−74.41	24.67	−1.15	2.50
15.458	119.7	−77.51	20.67	−2.36	6.44
16.019	108.9	−80.64	17.67	−9.20	6.84
16.491	100.1	−80.69	17.11	−8.01	0.19
16.961	92.1	−80.00	16.22	−5.68	−2.20
17.442	84.6	−81.38	14.22	−8.83	−3.60
17.934	77.5	−81.17	13.00	−14.51	0.56
18.397	71.4	−78.32	13.00	−15.55	6.68
18.851	65.9	−74.77	12.22	−15.36	9.41
19.331	60.7	−74.52	9.56	−17.67	7.03
19.809	55.9	−72.62	7.78	−17.82	5.32
20.321	51.3	−70.87	5.89	−18.94	1.14
20.813	47.2	−69.19	4.33	−15.92	−0.65
21.329	43.3	−66.90	3.00	−15.32	5.27
30.000	10.3	−66.90	3.00	−15.32	5.27

RH = relative humidity; U/V = zonal/meridional velocity component. Note that height represents height above sea level, with the first level (130 m) provided. Model results are shown using height above the surface as vertical coordinate.

Figure .1: *The initial sounding profile of the LBA case. RH refers to the relative humidity, U and V are the x and y-component of wind. Height represents the height above sea level. Figure directly adopted from Grabowski et al. (2006).*

Appendix B: MONC LBA reference simulation configuration file.

Source code may be downloaded from `https://code.metoffice.gov.uk/trac/monc/browser/main/branches/dev/chuenchungchui/r5611_lba_gzcp_flux`.

References

Abulikemu, A., Y. Wang, R. Gao, Y. Wang, and X. Xu, 2019: A numerical study of convection initiation associated with a gust front in bohai bay region, north china. *Journal of Geophysical Research: Atmospheres*, **124**, 13843–13860.

Anderson, J. L., V. Balaji, A. J. Broccoli, W. F. Cooke, T. L. Delworth, K. W. Dixon, L. J. Donner, K. A. Dunne, S. M. Freidenreich, S. T. Garner, et al., 2004: The new gfdl global atmosphere and land model am2–lm2. *Journal of Climate*, **17**, 4641–4673.

Arakawa, A., J.-H. Jung, and C.-M. Wu, 2011: Toward unification of the multiscale modeling of the atmosphere. *Atmospheric Chemistry and Physics*, **11**, 3731–3742, doi:10.5194/acp-11-3731-2011.

URL http://www.atmos-chem-phys.net/11/3731/2011/

Arakawa, A. and W. H. Schubert, 1974: Interaction of a cumulus cloud ensemble with the large-scale environment, part i. *Journal of the Atmospheric Sciences*, **31**, 674–701, doi:10.1175/1520-0469(1974)031¡0674:IOACCE¿2.0.CO;2.

URL http://dx.doi.org/10.1175/1520-0469(1974)031<0674:IOACCE>2.0.CO;2

Barry, R. G. and R. J. Chorley, 2009: *Atmosphere, weather and climate*. Routledge.

Bates, J., 1972: Tropical disturbances and the general circulation. *Quarterly Journal of the Royal Meteorological Society*, **98**, 1–16.

bbc.com, 2019: Tropical cyclones.

URL https://www.bbc.com/bitesize/guides/z9whg82/revision/4

Bechtold, P., E. Bazile, F. Guichard, P. Mascart, and E. Richard, 2001: A mass-flux convection scheme for regional and global models. *Quarterly Journal of the Royal Meteorological Society*, **127**, 869–886.

Bechtold, P., J. Chaboureau, A. Beljaars, A. Betts, M. Köhler, M. Miller, and J.-L. Redelsperger, 2004a: The simulation of the diurnal cycle of convective precipitation over land in global models. *Quart. J. Roy. Meteor Soc.*, **130**, 1449–1467.

Bechtold, P., J.-P. Chaboureau, A. Beljaars, A. Betts, M. Köhler, M. Miller, and J.-L. Redelsperger, 2004b: The simulation of the diurnal cycle of convective precipitation over land in a global model. *Quarterly Journal of the Royal Meteorological Society*, **130**, 3119–3137.

Bechtold, P., N. Semane, P. Lopez, J.-P. Chaboureau, A. Beljaars, and N. Bormann, 2013: Representing equilibrium and nonequilibrium convection in large-scale models. *Journal of the Atmospheric Sciences*, **71**, 734–753, doi:10.1175/JAS-D-13-0163.1.
URL http://dx.doi.org/10.1175/JAS-D-13-0163.1

Bengtsson, L., M. Steinheimer, P. Bechtold, and J.-F. Geleyn, 2013: A stochastic parametrization for deep convection using cellular automata. *Quarterly Journal of the Royal Meteorological Society*, **139**, 1533–1543.

Bennett, L. J., K. A. Browning, A. M. Blyth, D. J. Parker, and P. A. Clark, 2006: A review of the initiation of precipitating convection in the united kingdom. *Quarterly Journal of the Royal Meteorological Society: A journal of the atmospheric sciences, applied meteorology and physical oceanography*, **132**, 1001–1020.

Betts, A. K. and C. Jakob, 2002: Study of diurnal cycle of convective precipitation over amazonia using a single column model. *Journal of Geophysical Research: Atmospheres*, **107**, ACL 25–1–ACL 25–13, doi:10.1029/2002JD002264, 4732.
URL http://dx.doi.org/10.1029/2002JD002264

Blyth, A. M. and J. Latham, 1993: Development of ice and precipitation in new mexican summertime cumulus clouds. *Quarterly Journal of the Royal Meteorological Society*, **119**, 91–120.

Bougeault, P., 1985: A simple parameterization of the large-scale effects of cumulus convection. *Monthly Weather Review*, **113**, 2108–2121, doi:10.1175/1520-0493(1985)113¡2108:ASPOTL¿2.0.CO;2.
URL http://dx.doi.org/10.1175/1520-0493(1985)113<2108:ASPOTL>2.0.CO;2

Bretherton, C. S. and S. Park, 2008: A new bulk shallow-cumulus model and implications for penetrative entrainment feedback on updraft buoyancy. *Journal of the Atmospheric Sciences*, **65**, 2174–2193.

Bretherton, C. S. and P. K. Smolarkiewicz, 1989: Gravity waves, compensating subsidence and detrainment around cumulus clouds. *Journal of the atmospheric sciences*, **46**, 740–759.

Bright, D. R. and S. L. Mullen, 2002: Short-range ensemble forecasts of precipitation during the southwest monsoon. *Weather and Forecasting*, **17**, 1080–1100.

Brown, A. R., S. Derbyshire, and P. J. Mason, 1994: Large-eddy simulation of stable atmospheric boundary layers with a revised stochastic subgrid model. *Quarterly Journal of the Royal Meteorological Society*, **120**, 1485–1512.

Brown, N., M. Weiland, A. Hill, and B. Shipway, 2018: In situ data analytics for highly scalable cloud modelling on cray machines. *Concurrency and Computation: Practice and Experience*, **30**, e4331.

Brown, N., M. Weiland, A. Hill, B. Shipway, C. Maynard, T. Allen, and M. Rezny, 2020: A highly scalable met office nerc cloud model. *arXiv preprint arXiv:2009.12849*.

Brown, R. G. and C. Zhang, 1997: Variability of midtropospheric moisture and its effect on cloud-top height distribution during toga coare. *Journal of the atmospheric sciences*, **54**, 2760–2774.

Bryan, G. H. and R. Rotunno, 2005: Statistical convergence in simulated moist absolutely unstable layers. *Preprints, 11th Conf. on Mesoscale Processes, Albuquerque, NM, Amer. Meteor. Soc. M*, volume 1.

Byers, H. R. and R. R. Braham Jr, 1948: Thunderstorm structure and circulation. *Journal of Meteorology*, **5**, 71–86.

Camargo, S. J. and A. H. Sobel, 2005: Western north pacific tropical cyclone intensity and enso. *Journal of Climate*, **18**, 2996–3006.

Cetrone, J. and R. A. Houze Jr, 2006: Characteristics of tropical convection over the ocean near kwajalein. *Monthly weather review*, **134**, 834–853.

Chaboureau, J.-P., F. Guichard, J.-L. Redelsperger, and J.-P. Lafore, 2004: The role of stability and moisture in the diurnal cycle of convection over land. *Quarterly Journal of the Royal Meteorological Society: A journal of the atmospheric sciences, applied meteorology and physical oceanography*, **130**, 3105–3117.

Charney, J. G. and A. Eliassen, 1964: On the growth of the hurricane depression. *Journal of the Atmospheric Sciences*, **21**, 68–75.

Cheinet, S., 2003: A multiple mass-flux parameterization for the surface-generated convection. part i: Dry plumes. *Journal of the atmospheric sciences*, **60**, 2313–2327.

— 2004: A multiple mass flux parameterization for the surface-generated convection. part ii: Cloudy cores. *Journal of the atmospheric sciences*, **61**, 1093–1113.

Chen, C. and W. R. Cotton, 1987: The physics of the marine stratocumulus-capped mixed layer. *Journal of the atmospheric sciences*, **44**, 2951–2977.

Chen, D., 1991: Tests d'un nouveau schèma de convection pronostique adaptable à un modèle à maille variable. Technical report, Note de Centre, Météo France, CNRM, Groupe de Météorologie à Méso-Echelle, Météo-France, 42 av Coriolis, 31057 Toulouse Cedex, France.

Chen, T.-C., M.-C. Yen, J.-D. Tsay, C.-C. Liao, and E. S. Takle, 2014: Impact of afternoon thunderstorms on the land–sea breeze in the taipei basin during summer: An experiment. *Journal of Applied Meteorology and Climatology*, **53**, 1714–1738.

Clarke, R., 1970: Observational studies in the atmospheric boundary layer. *Quarterly Journal of the Royal Meteorological Society*, **96**, 91–114.

Cohen, B. G. and G. C. Craig, 2006: Fluctuations in an equilibrium convective ensemble. part ii: Numerical experiments. *Journal of the atmospheric sciences*, **63**, 2005–2015.

Craig, G. C. and B. G. Cohen, 2006: Fluctuations in an equilibrium convective ensemble. part i: Theoretical formulation. *Journal of the atmospheric sciences*, **63**, 1996–2004.

D'Andrea, F., P. Gentine, A. K. Betts, and B. R. Lintner, 2014: Triggering deep convection with a probabilistic plume model. *Journal of the Atmospheric Sciences*, **71**, 3881–3901, doi:10.1175/JAS-D-13-0340.1.

URL `http://dx.doi.org/10.1175/JAS-D-13-0340.1`

Davies, T., M. J. Cullen, A. J. Malcolm, M. Mawson, A. Staniforth, A. White, and N. Wood, 2005: A new dynamical core for the met office's global and regional modelling of the atmosphere. *Quarterly Journal of the Royal Meteorological Society*, **131**, 1759–1782.

Deardorff, J. W., 1970: Convective velocity and temperature scales for the unstable planetary boundary layer and for rayleigh convection. *Journal of the atmospheric sciences*, **27**, 1211–1213.

Doms, G., J. Förstner, E. Heise, J. Herzog, M. Raschendorfer, T. Reinhardt, B. Ritter, R. Schrodin, J. Schulz, and G. Vogel, 2007: A description of the non-hydrostatic regional model lm: Part ii: Physical parameterizations.

Doms, G. and U. Schättler, 2002: A description of the nonhydrostatic regional model lm: Part i: Dynamics and numerics. *Consortium forsmall-scale modelling, Deutscher Wetterdienst, Offenbach, Germany*.

Done, J., C. A. Davis, and M. Weisman, 2004: The next generation of nwp: Explicit forecasts of convection using the weather research and forecasting (wrf) model. *Atmospheric Science Letters*, **5**, 110–117.

Donner, L. J., 1993: A cumulus parameterization including mass fluxes, vertical momentum dynamics, and mesoscale effects. *Journal of the atmospheric sciences*, **50**, 889–906.

Donner, L. J., C. J. Seman, R. S. Hemler, and S. Fan, 2001: A cumulus parameterization includ-

ing mass fluxes, convective vertical velocities, and mesoscale effects: Thermodynamic and hydrological aspects in a general circulation model. *Journal of climate*, **14**, 3444–3463.

Emanuel, K. A., 1999: The power of a hurricane: An example of reckless driving on the information superhighway. *WEATHER-LONDON-*, **54**, 107–108.

Emanuel, K. A. et al., 1994: *Atmospheric convection*. Oxford University Press on Demand.

Esterheld, J. M. and D. J. Giuliano, 2008: Discriminating between tornadic and non-tornadic supercells: A new hodograph technique. *E-Journal of Severe Storms Meteorology*, **3**.

Fenn, C., R. Bettess, B. Golding, F. Farquharson, and T. Wood, 2005: The boscastle flood of 16 august 2004: Characteristics, causes and consequences.

Flerchinger, G., C. Hanson, and J. Wight, 1996: Modeling evapotranspiration and surface energy budgets across a watershed. *Water Resources Research*, **32**, 2539–2548.

Fletcher, J. K. and C. S. Bretherton, 2010: Evaluating boundary layer–based mass flux closures using cloud-resolving model simulations of deep convection. *Journal of the Atmospheric Sciences*, **67**, 2212–2225, doi:10.1175/2010JAS3328.1.

URL http://dx.doi.org/10.1175/2010JAS3328.1

Fricker, T., 2019: Evaluating tornado casualty rates in the united states.

Fritsch, J. M. and C. F. Chappell, 1980: Numerical prediction of convectively driven mesoscale pressure systems. part i: Convective parameterization. *Journal of the Atmospheric Sciences*, **37**, 1722–1733, doi:10.1175/1520-0469(1980)037¡1722:NPOCDM¿2.0.CO;2.

URL http://dx.doi.org/10.1175/1520-0469(1980)037<1722:NPOCDM>2.0.CO;2

Garratt, J. R., 1994: The atmospheric boundary layer. *Earth-Science Reviews*, **37**, 89–134.

Gentine, P., A. K. Betts, B. R. Lintner, K. L. Findell, C. C. Van Heerwaarden, and F. D'andrea, 2013a: A probabilistic bulk model of coupled mixed layer and convection. part ii: Shallow convection case. *Journal of the Atmospheric Sciences*, **70**, 1557–1576.

Gentine, P., A. K. Betts, B. R. Lintner, K. L. Findell, C. C. van Heerwaarden, A. Tzella, and F. D'Andrea, 2013b: A probabilistic bulk model of coupled mixed layer and convection. part i: Clear-sky case. *Journal of the Atmospheric Sciences*, **70**, 1543–1556.

Gerard, L. and J.-F. Geleyn, 2005: Evolution of a subgrid deep convection parametrization in a limited-area model with increasing resolution. *Quarterly Journal of the Royal Meteorological Society*, **131**, 2293–2312, doi:10.1256/qj.04.72.

URL http://dx.doi.org/10.1256/qj.04.72

Gilmore, M. S. and L. J. Wicker, 1998: The influence of midtropospheric dryness on supercell

morphology and evolution. *Monthly weather review*, **126**, 943–958.

Golaz, J.-C., V. E. Larson, and W. R. Cotton, 2002: A pdf-based model for boundary layer clouds. part i: Method and model description. *Journal of the atmospheric sciences*, **59**, 3540–3551.

Golding, B., P. Clark, and B. May, 2005: The boscastle flood: Meteorological analysis of the conditions leading to flooding on 16 august 2004. *Weather*, **60**, 230–235.

Grabowski, W. W., P. Bechtold, A. Cheng, R. Forbes, C. Halliwell, M. Khairoutdinov, S. Lang, T. Nasuno, J. Petch, W.-K. Tao, R. Wong, X. Wu, and K.-M. Xu, 2006: Daytime convective development over land: A model intercomparison based on lba observations. *Quarterly Journal of the Royal Meteorological Society*, **132**, 317–344, doi:10.1256/qj.04.147.
URL http://dx.doi.org/10.1256/qj.04.147

Grant, A., 1997: An observational study of the evening transition boundary-layer. *Quarterly Journal of the Royal Meteorological Society*, **123**, 657–677.

Grant, A. L. M. and A. R. Brown, 1999: A similarity hypothesis for shallow-cumulus transports. *Quarterly Journal of the Royal Meteorological Society*, **125**, 1913–1936, doi:10.1002/qj.49712555802.
URL http://dx.doi.org/10.1002/qj.49712555802

Gray, M., J. Petch, S. Derbyshire, A. Brown, A. Lock, H. Swann, and P. Brown, 2001: Version 2.3 of the met office large eddy model: Part ii. *Scientific documentation. Met Office (APR) Turbulence and Diffusion Rep*, **276**.

Gray, W. M., 1972: *Cumulus Convection and Larger-scale Circulations Part III: Broadscale and Mesoscale Considerations*. Colorado State University.

Gregory, D. and P. R. Rowntree, 1990: A mass flux convection scheme with representation of cloud ensemble characteristics and stability-dependent closure. *Monthly Weather Review*, **118**, 1483–1506, doi:10.1175/1520-0493(1990)118¡1483:AMFCSW¿2.0.CO;2.
URL http://dx.doi.org/10.1175/1520-0493(1990)118<1483:AMFCSW>2.0.CO;2

Grell, G. A. and D. Dévényi, 2002: A generalized approach to parameterizing convection combining ensemble and data assimilation techniques. *Geophysical Research Letters*, **29**, 38–1.

Grell, G. A., S. R. Freitas, et al., 2014: A scale and aerosol aware stochastic convective parameterization for weather and air quality modeling. *Atmos. Chem. Phys*, **14**, 5233–5250.

Gu, J.-F., R. S. Plant, C. E. Holloway, T. R. Jones, A. Stirling, P. A. Clark, S. J. Woolnough, and T. L. Webb, 2020: Evaluation of the bulk mass flux formulation using large-eddy simulations. *Journal of the Atmospheric Sciences*, **77**, 2115–2137.

Hendon, H. H. and K. Woodberry, 1993: The diurnal cycle of tropical convection. *Journal of Geophysical Research: Atmospheres*, **98**, 16623–16637.

Henneberg, O., B. Meyer, and J. O. Haerter, 2020: Particle-based tracking of cold pool gust fronts. *Journal of Advances in Modeling Earth Systems*, **12**, e2019MS001910.

Horinouchi, T., S. Pawson, K. Shibata, U. Langematz, E. Manzini, M. A. Giorgetta, F. Sassi, R. Wilson, K. Hamilton, J. De Grandpre, et al., 2003: Tropical cumulus convection and upward-propagating waves in middle-atmospheric gcms. *Journal of the Atmospheric Sciences*, **60**, 2765–2782.

Houze, R. A., 2014: *Cloud dynamics*. Academic press.

Irannejad, P., A. Henderson-Sellers, and S. Sharmeen, 2003: Importance of land-surface parameterization for latent heat simulation in global atmospheric models. *Geophysical Research Letters*, **30**.

Kaimal, J., J. Wyngaard, D. Haugen, O. Coté, Y. Izumi, S. Caughey, and C. Readings, 1976: Turbulence structure in the convective boundary layer. *Journal of Atmospheric Sciences*, **33**, 2152–2169.

Kain, J. S. and J. M. Fritsch, 1990: A one-dimensional entraining/detraining plume model and its application in convective parameterization. *Journal of the Atmospheric Sciences*, **47**, 2784–2802, doi:10.1175/1520-0469(1990)047¡2784:AODEPM¿2.0.CO;2.
URL `http://dx.doi.org/10.1175/1520-0469(1990)047<2784:AODEPM>2.0.CO;2`

Khouider, B., A. J. Majda, and M. A. Katsoulakis, 2003: Coarse-grained stochastic models for tropical convection and climate. *Proceedings of the National Academy of Sciences*, **100**, 11941–11946.

Kim, S.-Y. and S.-Y. Hong, 2018: The use of partial cloudiness in a bulk cloud microphysics scheme: Concept and 2d results. *Journal of the Atmospheric Sciences*, **75**, 2711–2719.

Kingsmill, D. E., 1995: Convection initiation associated with a sea-breeze front, a gust front, and their collision. *Monthly weather review*, **123**, 2913–2933.

Kuang, Z. and C. S. Bretherton, 2006: A mass-flux scheme view of a high-resolution simulation of a transition from shallow to deep cumulus convection. *Journal of the Atmospheric Sciences*, **63**, 1895–1909.

Kuell, V., A. Gassmann, and A. Bott, 2007: Towards a new hybrid cumulus parametrization scheme for use in non-hydrostatic weather prediction models. *Quarterly Journal of the Royal Meteorological Society: A journal of the atmospheric sciences, applied meteorology and physical*

oceanography, **133**, 479–490.

Kuo, H.-L., 1965: On formation and intensification of tropical cyclones through latent heat release by cumulus convection. *Journal of the Atmospheric Sciences*, **22**, 40–63.

— 1974: Further studies of the parameterization of the influence of cumulus convection on large-scale flow. *Journal of the Atmospheric Sciences*, **31**, 1232–1240.

Kuwano-Yoshida, A., T. Enomoto, and W. Ohfuchi, 2010: An improved pdf cloud scheme for climate simulations. *Quarterly Journal of the Royal Meteorological Society*, **136**, 1583–1597.

Lagmay, A. M. F., R. P. Agaton, M. A. C. Bahala, J. B. L. T. Briones, K. M. C. Cabacaba, C. V. C. Caro, L. L. Dasallas, L. A. L. Gonzalo, C. N. Ladiero, J. P. Lapidez, et al., 2015: Devastating storm surges of typhoon haiyan. *International journal of disaster risk reduction*, **11**, 1–12.

Lean, H. W., P. A. Clark, M. Dixon, N. M. Roberts, A. Fitch, R. Forbes, and C. Halliwell, 2008: Characteristics of high-resolution versions of the met office unified model for forecasting convection over the united kingdom. *Monthly Weather Review*, **136**, 3408–3424, doi:10.1175/2008MWR2332.1.

URL `http://dx.doi.org/10.1175/2008MWR2332.1`

Lee, M.-I., S. D. Schubert, M. J. Suarez, I. M. Held, N.-C. Lau, J. J. Ploshay, A. Kumar, H.-K. Kim, and J.-K. E. Schemm, 2007: An analysis of the warm-season diurnal cycle over the continental united states and northern mexico in general circulation models. *Journal of Hydrometeorology*, **8**, 344–366.

Lenschow, D. and P. Stephens, 1980: The role of thermals in the convective boundary layer. *Boundary-Layer Meteorology*, **19**, 509–532.

— 1982: Mean vertical velocity and turbulence intensity inside and outside thermals. *Atmospheric Environment (1967)*, **16**, 761–764.

Leonard, B., M. MacVean, and A. Lock, 1993: Positivity-preserving numerical schemes for multidimensional advection.

Li, Y., 2004: Studies on calculating convective energy with different moist adiabatic processes. *22nd Conference on Severe Local Storms*.

Liebmann, B., H. H. Hendon, and J. D. Glick, 1994: The relationship between tropical cyclones of the western pacific and indian oceans and the madden-julian oscillation. *Journal of the Meteorological Society of Japan. Ser. II*, **72**, 401–412.

Lin, J. W.-B. and J. D. Neelin, 2003: Toward stochastic deep convective parameterization in general circulation models. *Geophysical Research Letters*, **30**, n/a–n/a, doi:10.1029/2002GL016203, 1162.

URL http://dx.doi.org/10.1029/2002GL016203

Madden, R. A. and P. R. Julian, 1972: Description of global-scale circulation cells in the tropics with a 40–50 day period. *Journal of the atmospheric sciences*, **29**, 1109–1123.

Mahoney III, W. P., 1988: Gust front characteristics and the kinematics associated with interacting thunderstorm outflows. *Monthly weather review*, **116**, 1474–1492.

Majda, A. J. and B. Khouider, 2002: Stochastic and mesoscopic models for tropical convection. *Proceedings of the National Academy of Sciences*, **99**, 1123–1128.

Malardel, S. and P. Bechtold, 2019: The coupling of deep convection with the resolved flow via the divergence of mass flux in the ifs. *Quarterly Journal of the Royal Meteorological Society*, **145**, 1832–1845.

Maloney, E. D. and D. L. Hartmann, 2001: The madden–julian oscillation, barotropic dynamics, and north pacific tropical cyclone formation. part i: Observations. *Journal of the atmospheric sciences*, **58**, 2545–2558.

Mapes, B. and R. A. Houze, 1992: An integrated view of the 1987 australian monsoon and its mesoscale convective systems. i: Horizontal structure. *Quarterly Journal of the Royal Meteorological Society*, **118**, 927–963.

Mapes, B. E., 2000: Convective inhibition, subgrid-scale triggering energy, and stratiform instability in a toy tropical wave model. *Journal of the Atmospheric Sciences*, **57**, 1515–1535, doi:10.1175/1520-0469(2000)057¡1515:CISSTE¿2.0.CO;2.

URL http://dx.doi.org/10.1175/1520-0469(2000)057<1515:CISSTE>2.0.CO;2

Market, P., K. Grempler, P. Sumrall, and C. Henson, 2019: Analysis of severe elevated thunderstorms over frontal surfaces using dcin and dcape. *Atmosphere*, **10**, 449.

Markowski, P. and Y. Richardson, 2011: *Mesoscale meteorology in midlatitudes*, volume 2. John Wiley & Sons.

Mellado, J. P., B. Stevens, H. Schmidt, and N. Peters, 2010: Probability density functions in the cloud-top mixing layer. *New Journal of Physics*, **12**, 085010.

metoffice.gov.uk, 2015: Boscastle floods.

URL https://www.metoffice.gov.uk/learning/learn-about-the-weather/weather-phenomena/case-studies/boscastle

Miyamoto, Y., Y. Kajikawa, R. Yoshida, T. Yamaura, H. Yashiro, and H. Tomita, 2013: Deep moist atmospheric convection in a subkilometer global simulation. *Geophysical Research Letters*, **40**,

4922–4926.

Monin, A. and A. Obukhov, 1954: Basic laws of turbulent mixing in the surface layer of the atmosphere. *Contrib. Geophys. Inst. Acad. Sci. USSR*, **151**, e187.

Moorthi, S. and M. J. Suarez, 1992: Relaxed arakawa-schubert. a parameterization of moist convection for general circulation models. *Monthly Weather Review*, **120**, 978–1002.

Mori, N., M. Kato, S. Kim, H. Mase, Y. Shibutani, T. Takemi, K. Tsuboki, and T. Yasuda, 2014: Local amplification of storm surge by super typhoon haiyan in leyte gulf. *Geophysical research letters*, **41**, 5106–5113.

Nakamura, K., R. Kershaw, and N. Gait, 1996: Prediction of near-surface gusts generated by deep convection. *Meteorological Applications*, **3**, 157–167.

Neggers, R., A. Siebesma, G. Lenderink, and A. Holtslag, 2004: An evaluation of mass flux closures for diurnal cycles of shallow cumulus. *Monthly weather review*, **132**, 2525–2538.

Ogura, Y., 1972: Clouds and convection. parameterization of subgrid-scale processes, garp publ. ser., no. 8, 20-39. akio arakawa and nvayne howard schubert 701-—-, and na phillips, 1962: Scale analysis of deep and shallow convection in the atmosphere. *J. Atmos. Sci*, **19**, 173–179.

Ooyama, K., 1964: A dynamical model for the study of tropical cyclone development. *Geofisica Internacional (Mexico)*, **4**, 187–198.

Pai, D., J. Bhate, O. Sreejith, and H. Hatwar, 2011: Impact of mjo on the intraseasonal variation of summer monsoon rainfall over india. *Climate Dynamics*, **36**, 41–55.

Palmer, T. N., 2001: A nonlinear dynamical perspective on model error: A proposal for non-local stochastic-dynamic parametrization in weather and climate prediction models. *Quarterly Journal of the Royal Meteorological Society*, **127**, 279–304.

Pan, D.-M. and D. D. A. Randall, 1998: A cumulus parameterization with a prognostic closure. *Quarterly Journal of the Royal Meteorological Society*, **124**, 949–981, doi:10.1002/qj.49712454714.
URL `http://dx.doi.org/10.1002/qj.49712454714`

Petch, J., 2006: Sensitivity studies of developing convection in a cloud-resolving model. *Quarterly Journal of the Royal Meteorological Society*, **132**, 345–358.

Plant, R. S. and G. C. Craig, 2008: A stochastic parameterization for deep convection based on equilibrium statistics. *Journal of the Atmospheric Sciences*, **65**, 87–105, doi:10.1175/2007JAS2263.1.
URL `http://dx.doi.org/10.1175/2007JAS2263.1`

Plant, R. S. and J.-i. Yano, 2015: *Parameterization Of Atmospheric Convection (In 2 Volumes)*, volume 1. World Scientific.

Qian, J.-H., A. W. Robertson, and V. Moron, 2010: Interactions among enso, the monsoon, and diurnal cycle in rainfall variability over java, indonesia. *Journal of the Atmospheric Sciences*, **67**, 3509–3524.

Raymond, D. J., 1995: Regulation of moist convection over the west pacific warm pool. *Journal of the Atmospheric Sciences*, **52**, 3945–3959, doi:10.1175/1520-0469(1995)052¡3945:ROMCOT¿2.0.CO;2.

URL http://dx.doi.org/10.1175/1520-0469(1995)052<3945:ROMCOT>2.0.CO;2

Ricciardulli, L. and R. R. Garcia, 2000: The excitation of equatorial waves by deep convection in the ncar community climate model (ccm3). *Journal of the atmospheric sciences*, **57**, 3461–3487.

Romero, R., C. Doswell III, and R. Riosalido, 2001: Observations and fine-grid simulations of a convective outbreak in northeastern spain: Importance of diurnal forcing and convective cold pools. *Monthly weather review*, **129**, 2157–2182.

Savre, J., 2021: Formation and maintenance of subsiding shells around non-precipitating and precipitating cumulus clouds. *Quarterly Journal of the Royal Meteorological Society*, **147**, 728–745, doi:https://doi.org/10.1002/qj.3942.

URL https://rmets.onlinelibrary.wiley.com/doi/abs/10.1002/qj.3942

Schaefer, J. and R. Edwards, 1999: The spc tornado/severe thunderstorm database. *Preprints, 11th Conf. on Applied Climatology, Dallas, TX, Amer. Meteor. Soc*, volume 6.

Seiki, A. and Y. N. Takayabu, 2007: Westerly wind bursts and their relationship with intraseasonal variations and enso. part i: Statistics. *Monthly Weather Review*, **135**, 3325–3345.

Senay, G. B., M. Budde, J. P. Verdin, and A. M. Melesse, 2007: A coupled remote sensing and simplified surface energy balance approach to estimate actual evapotranspiration from irrigated fields. *Sensors*, **7**, 979–1000.

Siebesma, A. P., C. S. Bretherton, A. Brown, A. Chlond, J. Cuxart, P. G. Duynkerke, H. Jiang, M. Khairoutdinov, D. Lewellen, C.-H. Moeng, et al., 2003: A large eddy simulation intercomparison study of shallow cumulus convection. *Journal of the Atmospheric Sciences*, **60**, 1201–1219.

Simpson, J., 1971: On cumulus entrainment and one-dimensional models. *Journal of the Atmospheric sciences*, **28**, 449–455.

Simpson, J. and V. Wiggert, 1969: Models of precipitating cumulus towers. *Mon. Wea. Rev*, **97**, 471–489.

Slingo, J. M., K. R. Sperber, J.-J. Morcrette, and G. L. Potter, 1992: Analysis of the temporal behavior of convection in the tropics of the european centre for medium-range weather forecasts model. *Journal of Geophysical Research: Atmospheres*, **97**, 18119–18135, doi:10.1029/92JD01408. URL http://dx.doi.org/10.1029/92JD01408

Smagorinsky, J., 1963: General circulation experiments with the primitive equations: I. the basic experiment. *Monthly weather review*, **91**, 99–164.

Smith, R. K., 2013: *The physics and parameterization of moist atmospheric convection*, volume 505. Springer Science & Business Media.

Sobel, A. H. and E. D. Maloney, 2000: Effect of enso and the mjo on western north pacific tropical cyclones. *Geophysical research letters*, **27**, 1739–1742.

Sobel, A. H., S. E. Yuter, C. S. Bretherton, and G. N. Kiladis, 2004: Large-scale meteorology and deep convection during trmm kwajex. *Monthly Weather Review*, **132**, 422–444.

Soden, B. J., 2000: The diurnal cycle of convection, clouds, and water vapor in the tropical upper troposphere. *Geophysical research letters*, **27**, 2173–2176.

Sommeria, G. and J. Deardorff, 1977: Subgrid-scale condensation in models of nonprecipitating clouds. *Journal of the Atmospheric Sciences*, **34**, 344–355.

Song, X. and G. J. Zhang, 2009: Convection parameterization, tropical pacific double itcz, and upper-ocean biases in the ncar ccsm3. part i: Climatology and atmospheric feedback. *Journal of Climate*, **22**, 4299–4315.

Stull, R. B., 1988: An introduction to boundary layer meteorology. *Atmospheric sciences*.

Tan, Z., C. M. Kaul, K. G. Pressel, Y. Cohen, T. Schneider, and J. Teixeira, 2018: An extended eddy-diffusivity mass-flux scheme for unified representation of subgrid-scale turbulence and convection. *Journal of advances in modeling earth systems*, **10**, 770–800.

Tetens, O., 1930: Uber einige meteorologische begriffe. *Zeitschrift fur Geophysik*, **6**, 297–309.

Thuburn, J., H. Weller, G. K. Vallis, R. J. Beare, and M. Whitall, 2018: A framework for convection and boundary layer parameterization derived from conditional filtering. *Journal of the Atmospheric Sciences*, **75**, 965–981.

Tiedtke, M., 1989: A comprehensive mass flux scheme for cumulus parameterization in large-scale models. *Monthly Weather Review*, **117**, 1779–1800.

Timmermans, W. J., W. P. Kustas, M. C. Anderson, and A. N. French, 2007: An intercomparison of the surface energy balance algorithm for land (sebal) and the two-source energy balance (tseb) modeling schemes. *Remote Sensing of Environment*, **108**, 369–384.

Tong, H., J. C. Chan, and W. Zhou, 2009: The role of mjo and mid-latitude fronts in the south china

sea summer monsoon onset. *Climate Dynamics*, **33**, 827–841.

Torn, R. D. and G. S. Romine, 2015: Sensitivity of central oklahoma convection forecasts to upstream potential vorticity anomalies during two strongly forced cases during mpex. *Monthly Weather Review*, **143**, 4064–4087.

Wakimoto, R. M., 1982: The life cycle of thunderstorm gust fronts as viewed with doppler radar and rawinsonde data. *Monthly weather review*, **110**, 1060–1082.

Weisman, M. L. and J. B. Klemp, 1986: Characteristics of isolated convective storms. *Mesoscale meteorology and forecasting*, Springer, 331–358.

Weisman, M. L., W. C. Skamarock, and J. B. Klemp, 1997: The resolution dependence of explicitly modeled convective systems. *Monthly Weather Review*, **125**, 527–548.

Weller, G. B., D. S. Cooley, and S. R. Sain, 2012: An investigation of the pineapple express phenomenon via bivariate extreme value theory. *Environmetrics*, **23**, 420–439.

Weller, H. and W. A. McIntyre, 2019: Numerical solution of the conditionally averaged equations for representing net mass flux due to convection. *Quarterly Journal of the Royal Meteorological Society*, **145**, 1337–1353.

Wilcox, E. M. and L. J. Donner, 2007: The frequency of extreme rain events in satellite rain-rate estimates and an atmospheric general circulation model. *Journal of Climate*, **20**, 53–69.

Williams, E. and N. Renno, 1993: An analysis of the conditional instability of the tropical atmosphere. *Monthly Weather Review*, **121**, 21–36.

Wu, X., L. Deng, X. Song, G. Vettoretti, W. R. Peltier, and G. J. Zhang, 2007: Impact of a modified convective scheme on the madden-julian oscillation and el niño–southern oscillation in a coupled climate model. *Geophysical Research Letters*, **34**.

Wyngaard, J., O. Coté, and Y. Izumi, 1971: Local free convection, similarity, and the budgets of shear stress and heat flux. *Journal of the Atmospheric Sciences*, **28**, 1171–1182.

Xie, S. and M. Zhang, 2000: Impact of the convection triggering function on single-column model simulations. *Journal of Geophysical Research: Atmospheres*, **105**, 14983–14996.

Xu, K.-M., A. Arakawa, and S. K. Krueger, 1992: The macroscopic behavior of cumulus ensembles simulated by a cumulus ensemble model. *Journal of the atmospheric sciences*, **49**, 2402–2420.

Yanai, M., 1971: A review of recent studies of tropical meteorology relevant to the planning of gate. *Experimental Design Proposal by the Interim Scientific and Management Group (ISMG), WMO*, **2**, 1–43.

Yang, G.-Y. and J. Slingo, 2001: The diurnal cycle in the tropics. *Monthly Weather Review*, **129**, 784–801.

Yang, K., T. Koike, H. Fujii, T. Tamura, X. Xu, L. Bian, and M. Zhou, 2004: The daytime evolution of the atmospheric boundary layer and convection over the tibetan plateau: observations and simulations. *Journal of the Meteorological Society of Japan. Ser. II*, **82**, 1777–1792.

Yeh, S.-W., W. Cai, S.-K. Min, M. J. McPhaden, D. Dommenget, B. Dewitte, M. Collins, K. Ashok, S.-I. An, B.-Y. Yim, et al., 2018: Enso atmospheric teleconnections and their response to greenhouse gas forcing. *Reviews of Geophysics*, **56**, 185–206.

Zhang, G. J., 2002: Convective quasi-equilibrium in midlatitude continental environment and its effect on convective parameterization. *Journal of Geophysical Research: Atmospheres*, **107**.

Zhang, G. J. and N. A. McFarlane, 1995: Sensitivity of climate simulations to the parameterization of cumulus convection in the canadian climate centre general circulation model. *Atmosphere-ocean*, **33**, 407–446.

Zhang, G. J. and M. Mu, 2005: Simulation of the madden–julian oscillation in the ncar ccm3 using a revised zhang–mcfarlane convection parameterization scheme. *Journal of Climate*, **18**, 4046–4064.

Zhang, G. J. and X. Song, 2010: Convection parameterization, tropical pacific double itcz, and upper-ocean biases in the ncar ccsm3. part ii: Coupled feedback and the role of ocean heat transport. *Journal of Climate*, **23**, 800–812.

Zhang, G. J. and H. Wang, 2006: Toward mitigating the double itcz problem in ncar ccsm3. *Geophysical research letters*, **33**.

Zhang, Y. and S. A. Klein, 2010: Mechanisms affecting the transition from shallow to deep convection over land: Inferences from observations of the diurnal cycle collected at the arm southern great plains site. *Journal of the Atmospheric Sciences*, **67**, 2943–2959.